Applied Quantum Architectures (AQUA)
Mekelweg 4,
2628 CD Delft
The Netherlands
http://www.aqua.ewi.tudelft.nl/

AQUA-2016-09

M.Sc. Thesis

Small-Animal PET Detector Module Based on Multichannel Digital Silicon Photomultipliers

Siddharth Sinha

Abstract

Positron Emission Tomography (PET) is a nuclear-medicine imaging technique used extensively in diagnosis of early stage tumors and cancers. Apart from clinical applications, PET is also employed in biomedical and pharmaceutical research. For this purpose, small-animal PET scan systems have been developed with superior performance metrics and cost efficiency. Small-animal PET scan systems provide higher spatial and temporal resolution. Conventionally, PET scan systems are developed using photomultiplier tubes (PMTs) which have certain intrisnsic limit on spatial and temporal resolution. The prospect of designing PET scan systems with solid-state based photomultipliers is quite rewarding in terms of detector miniaturization and higher spatial and temporal resolution.

The thesis project presented hereafter discusses the design implementation of a small-animal PET scan detector module based on multichannel digital silicon photomultipliers (MD-SiPMs). It outlines the design details of the MD-SiPMs i.e., its pixel and array architecture, readout mechanism, on-chip time-to-digital converters (TDCs). The firmware development over field-programmable gate arrays (FPGAs) is presented next, followed by radiation characterization using a ^{22}Na radioactive source. Finally, a proof of concept for timing estimation using multiple timestamps is provided.

Small-Animal PET Detector Module Based on Multichannel Digital Silicon Photomultipliers

Thesis

submitted in partial fulfillment of the
requirements for the degree of

Master of Science

in

Embedded Systems

by

Siddharth Sinha
born in Kanpur, India

This work was performed in:

Applied Quantum Architectures (AQUA) Lab
Department of Quantum Engineering
Faculty of Electrical Engineering, Mathematics and Computer Science
Delft University of Technology

Delft University of Technology

Delft University of Technology
Department of
Quantum Engineering

The undersigned hereby certify that they have read and recommend to the Faculty of Electrical Engineering, Mathematics and Computer Science for acceptance a thesis entitled **"Small-Animal PET Detector Module Based on Multichannel Digital Silicon Photomultipliers"** by **Siddharth Sinha** in partial fulfillment of the requirements for the degree of **Master of Science**.

Dated: 30^{th} September, 2016

Chairman:

Prof. Dr. Edoardo Charbon

Advisor:

Ir. Esteban Venialgo Araujo

Committee Members:

Asst. Prof. Dr. Dennis R. Schaart

Asst. Prof. Dr. Fabio Sebastiano

Abstract

Positron Emission Tomography (PET) is a nuclear-medicine imaging technique used extensively in diagnosis of early stage tumors and cancers. Apart from clinical applications, PET is also employed in biomedical and pharmaceutical research. For this purpose, small-animal PET scan systems have been developed with superior performance metrics and cost efficiency. Small-animal PET scan systems provide higher spatial and temporal resolution. Conventionally, PET scan systems are developed using photomultiplier tubes (PMTs) which have certain intrisnsic limit on spatial and temporal resolution. The prospect of designing PET scan systems with solid-state based photomultipliers is quite rewarding in terms of detector miniaturization and higher spatial and temporal resolution.

The thesis project presented hereafter discusses the design implementation of a small-animal PET scan detector module based on multichannel digital silicon photomultipliers (MD-SiPMs). It outlines the design details of the MD-SiPMs i.e., its pixel and array architecture, readout mechanism, on-chip time-to-digital converters (TDCs). The firmware development over field-programmable gate arrays (FPGAs) is presented next, followed by radiation characterization using a ^{22}Na radioactive source. Finally, a proof of concept for timing estimation using multiple timestamps is provided.

Acknowledgments

First of all I would like to express my sincere gratitude to my supervisor Ir. Esteban Venialgo Araujo and my Professor Dr. Edoardo Charbon. With their constant guidance and support, I am able to complete the M.S. thesis project. I would like to thank my supervisor for offering me the opportunity to work with him on Positron Emission Tomography and helping me all along the way. I learned a lot from his meticulous time and project management skills, approach towards problem and developing a right strategy to resolve it.

I would also like to thank Augusto Carimatto to help me at every moment during my thesis work. From understanding the chip operation, firmware porting and designing a new operation mode in the firmware, he was always there to help and guide me on how to proceed. Despite being extremely busy with his Ph.D., he always helped me whenever I was stuck with a problem and needed his advice. He spent hours at stretch with me to make it work and hence I attribute a level of my thesis to him.

I would also like to thank all of my colleagues: Dr. Chockalingam Veerappan, Ting Gong, Harald Homulle, Ivan Michel Antolovic, Dr. Myung-Jae Lee, Chao Zhang, Rosario Incandela, Arin Can Ulku, Preethi Padhmanabhan, Bishnu Patra, Bahador Valizadeh Pasha, Lin Song and Jeroen Van Dijk for making this 1 year very pleasant and memorable.

I would like to thank my friends Shubhankar, Paul, Aniruddha, Alejandro, Maria, Angela, Elisabeth(Lissi), Apurva and Dimitris for being there on almost every weekend and ready to go out for drinks, movies, music festivals and what not. Out of all the people mentioned above, I think the one who needs a special mention is Maria Luisa for her freakishly insane love for cats. So much, that she would attend my thesis defense only if I put a picture of a cat in my presentation.

Siddharth Sinha
Delft, The Netherlands
30^{th} September, 2016

Contents

Abstract **v**

Acknowledgments **vii**

1 Introduction to Small-Animal Positron Emission Tomography **1**
1.1 Motivation . . . 1
1.1.1 Small-Animal Positron Emission Tomography requirements . . . 2
1.1.2 Thesis Goals . . . 2
1.2 Thesis Outline . . . 3
1.3 Physics of Positron Emission Tomography . . . 3
1.3.1 Positron-Electron Annihilation . . . 4
1.4 Preclinical PET Scan Systems . . . 6
1.5 State-of-the-art of Preclinical systems . . . 7
1.6 PET detector module for small-animal . . . 8
1.6.1 Sensitivity . . . 8
1.6.2 Dead Time . . . 9
1.6.3 Energy Resolution . . . 9
1.6.4 Spatial Resolution . . . 10
1.6.5 Timing Resolution . . . 10
1.6.6 Non-Idealities . . . 10

2 Multichannel Digital SiPMs **13**
2.1 Architecture . . . 13
2.2 SPAD-cell Array . . . 14
2.2.1 Single-Photon Avalanche Diodes . . . 14
2.2.2 SPAD-cell Design . . . 20
2.2.3 MD SiPM Pixel Array . . . 21
2.3 Time-to-Digital Converters . . . 23
2.3.1 TDC Architecture . . . 24
2.4 Read-out Architecture . . . 25
2.4.1 Mode 0 . . . 26
2.4.2 Mode 2 . . . 26

3 Firmware Development **27**
3.1 Mode 0 porting to Spartan-6 . . . 27
3.2 Mode 2 Designing . . . 32
3.3 SPAD-cell Array and Energy Count Verification . . . 35
3.4 TDC and Dummy Verification . . . 37
3.5 Temperature Sensing and Controlling for single chip operation . . . 39
3.6 Expansion to Multiple SiPMs Read-out . . . 40

4 Radiation Characterization **45**
4.1 Energy Measurements . . . 45
4.1.1 Experimentation setup and Methodology. . . . 46
4.1.2 Results . . . 46
4.2 Dead Time . . . 47
4.3 Timing Resolution . . . 53
4.3.1 Experimentation setup and Methodology for SPTR . . . 53
4.3.2 SPTR Results . . . 55
4.3.3 Impact of DCR on TDCs . . . 55
4.4 Light Crosstalk . . . 56

5 Timing Estimation with Multiple Timestamps **59**
5.1 Theory . . . 59
5.1.1 Statistical behaviour of scintillation photons. . . . 60
5.1.2 Cramér-Rao Lower Bound for Time Estimation of Multiple Photons 62
5.2 GATE Simulations . . . 63
5.3 Maximum Likelihood Estimators (MLE) . . . 63
5.4 Best Linear Unbiased Estimations (BLUE) . . . 64
5.5 MLE and BLUE Simulation Results . . . 65

6 Conclusion **69**
6.1 Summary and Contributions . . . 69
6.2 Further Improvements . . . 70
6.3 Future of SPAD based PET sensors . . . 70

Bibliography **72**

List of Figures

1.1 Positron-electron annihilation process resulting in emission of two gamma photons 180° apart and each possessing $511keV$ of energy . . . 5
1.2 Positron Emission Tomography setup with a pair of detectors used to detect the two emitted gamma photons. 6
1.3 (A) True Coincidence. (B) Scattered Coincidence. (C) Random Coincidence. (D) Multiple Coincidence. 11

2.1 9×18 MD-SiPM array chip [1] 13
2.2 A P-N junction diode 15
2.3 P-N junction diode with depletion region. 16
2.4 Passive Quench and Recharge Circuitry. 17
2.5 Transient behaviour of passive quenching and recharge operation [27]. (a) Short-circuit current versus time. (b) Transient behaviour of voltage across quenching resistor. 19
2.6 Active quenching and recharge circuit 19
2.7 Transient behaviour of diode with active quenching and recharge mechanism [27]. (a) Short-circuit current versus time. (b) Voltage across quenching resistor. (c) Quench and recharge pulse generated by the current sense circuitry. 21
2.8 Pixel schematic. 22
2.9 Schematic of the MD-SiPM pixel array. 23
2.10 (a)Block diagram of a 432 column-parallel TDC including a dummy TDC. (b) TDC architecture [1]. 25

3.1 Timing diagram for configuration phase. 28
3.2 (a). SPAD-cell map for first 4 columns activated. (b). SPAD-cell map for next 4.5 columns activated. 30
3.3 Timing diagram for mode-0 read out. 31
3.4 TDC data structure in read out process. 32
3.5 Timing diagram for mode-2 read out. 34
3.6 Energy counter readout algorithm. 35
3.7 (a) Masking profile programmed in the chip. (b) SPAD-cell array plot. 36
3.8 Mode-2 energy count plots 37
3.9 DISEXTBIN vs VCOEN signal relation. (a) Electrical trigger set at $250ns$. (b) Electrical trigger set at $450ns$. 38
3.10 (a) Dummy TDC at $500ns$ and electrical trigger at $50ns$. (b) Dummy TDC at $750ns$ and electrical trigger at $250ns$. (c) Dummy TDC at $750ns$ and electrical trigger at $450ns$. 42
3.11 Water cooled heatsink for 1 MD-SiPM chip. 43
3.12 4×2 motherboard model housing 8 MD-SiPM array chips. (3D rendering using Altium PCB designer). (a) Top layer with connectors for 8 MD-SiPM chip. (b) Bottom layer with connectors for Spartan-6 FPGA board. 43

3.13 (a) 3D model of the water cooling assembly mounted over the motherboard. (b) Actual image of water cooling assembly over motherboard with 2 MD-SiPM chips, 6 dummies (water is circulated through the inlet and outlet ports). 44

4.1 (a) 0.8mm pitch scintillator. (b) 1.6mm pitch scintillator. (c) Actual scintillators glued over the MD-SiPM array chip. 47
4.2 Two scintillators installed on test boards with fan based cooling. 48
4.3 (a), (b), (c) and (d) are 4 instances of gamma scintillations detected by 1.6mm scintillator pitch. 49
4.4 (a), (b), (c) and (d) are 4 instances of gamma scintillations detected by 0.8mm scintillator pitch. 50
4.5 (a) Row-wise centroid histogram for 0.8mm pixel scintillator. (b) Column-wise centroid histogram for 0.8mm pixel scintillator. 51
4.6 (a) Row-wise centroid histogram for 1.6mm pixel scintillator. (b) Column-wise centroid histogram for 1.6mm pixel scintillator. 51
4.7 Normalized 2D histogram for 0.8mm pixel scintillator. 52
4.8 Number of gamma scintillations per block. 53
4.9 (a) The source and detector placement. (b) GATE simulation showing gamma photons emitting out of the source. 54
4.10 Energy spectrum of LYSO scintillator. 54
4.11 SPTR measurement setup. 55
4.12 SPTR measurement with a 405nm, blue laser. (a) Complete TDC histogram for TDC No. 260. (b) TDC histogram zoomed on the first 10 laser peaks. 56
4.13 (a) CDF of free TDCs for 50ns smart reset period. (b) CDF of free TDCs for 100ns smart reset period. (c) CDF of free TDCs for 200ns smart reset period. (d) CDF of free TDCs for 300ns smart reset period. 57
4.14 1.6mm pitch scintillator with light crosstalk resulting in the scintillation width to be approximately 2.0mm. 58
4.15 0.8mm pitch scintillator with light crosstalk resulting in the scintillation width to be approximately 1.32mm. 58

5.1 (a) Normalized PDF of the emitted photon upon a scintillation. (b) Normalized PDF zoomed at time $t = 0.1\mu s(T_\circ)$. 60
5.2 Block diagram of scintillation photon timestamp estimation methodology [2]. 61
5.3 GATE simulation results of emission PDF for photo electrons generated upon gamma photon absorption within a scintillator. 65
5.4 CRT @ FWHM versus photoelectron order calcuated using BLUE algorithm. 66
5.5 CRT @ FWHM versus photoelectron order calcuated using MLE algorithm. 67

6.1 4×1 motherboard for PET scan detector module. (a) Top layer with connectors for 4 MD-SiPM chips. (b) Bottom layer with connectors for Spartan-6 FPGA board. 70

List of Tables

1.1 Small-Animal PET scan system performance requirement. [3]. 2
1.2 Radiotracers used in Medical imaging applications [4] 4
1.3 Commercially available Preclinical PET scan systems and their reported performance metrics [3, 5]. 7

3.1 Spartan-6 XC6SLX150 specifications. 27
3.2 Configuration data for chip. 29
3.3 Signal description for mode-2 energy counter readout. 34
3.4 Temperature of a single MD-SiPM operation with and without water cooled heatsink. 40

4.1 Scintillator properties for LYSO and BGO scintillators [7, 8]. 45
4.2 Radioactive properties of ^{22}Na. 46

Introduction to Small-Animal Positron Emission Tomography 1

PET (Positron Emission Tomography) is a nuclear-medicine imaging technique used extensively in diagnosis and research applications [9]. PET finds its application in diagnosis and treatment of various diseases, encompassing many types of cancer/tumors, neurological impairments, heart diseases, and other abnormalities in the body.

In PET imaging, the patient is injected with radioactive compounds, often known as radiopharmaceuticals or radiotracers, which emit positrons as a result of a nuclear decay process. Emitted photons, upon annihilation, release gamma photons which are detected using special detectors. A detailed functional image is generated, which can provide useful molecular information. The radiotracers used can vary depending upon the type of PET scan exam the patient is undergoing and they can be introduced either as an intravenous injection, swallowed as a medicine or inhaled as a gas. For instance, in lung ventilation/perfusion scan for pulmonary embolism Ga-68 or ^{68}Ga Aerosol (Galligas) is inhaled for PET scan [10].

PET scans are very useful for providing detailed insight about several important body functions such as blood flow, oxygen uptake and glucose metabolism. These characteristics make PET a suitable medical imaging technique, which can be used to map certain brain functions and eventually help in early diagnosis of Alzheimer's and Parkinson's diseases [11]. PET scan images can reveal changes in the brain from very early stages of the disease process. In fact, researchers have been able to identify disease signatures even before the symptoms have started to develop [12].

1.1 Motivation

The use of PET for preclinical research to study small-animal models of human disease is growing significantly. In order to fully understand the disease processes, animal models have turned out to be a rather valuable tool. Apart from PET, many other conventional imaging techniques have been adapted for visualizing small animals. Imaging techniques provide an opportunity to understand biochemical processes in a non-invasive manner. Constant research and development over the years in designing PET scanners, used for small-animal PET imaging, have yielded significant benefits in sensitivity, spatial resolution, and eventually higher image quality [12].

PET is a preferred choice for clinical oncology and since with a suitable radiotracer many biological compounds can be traced, this makes PET an apt choice for biomedical research and in development of innovative pathways for diagnosis and novel treatment strategies.

1.1.1 Small-Animal Positron Emission Tomography requirements

Clinical PET scan systems have been in use since the 1970s. Initially, PET scan systems were introduced as a new research domain for studying various biological processes in human diseases [13]. With constant research and development in the PET scan design, numerous commercial PET scan systems were made available and a need for standardization in PET system specifications arose. Consequently, agencies like the International Atomic Energy Agency (IAEA), National Electrical Manufacturers Association (NEMA) and European Association of Nuclear Medicine (EANM) have laid out benchmark tests for clinical PET scan system's quality assurance.

With constant improvements in PET detector design and scintillator performance, PET scan systems have been developed for small-animal tomography. These PET scan systems are usually employed in biomedical and pharmaceutical research domain for understanding disease processes and for finding new pathways in radiotracer development [12]. In order to standardize preclinical PET scan systems and to prepare benchmarks for the same, NEMA NU 4-2008 standard was published [3]. In order to fully characterize the small-animal PET scan detector module using MD-SiPMs, some crucial performance goals are set forth. Table. 1.1 lists the performance requirements for preclinical PET scan system under consideration.

Performance Metric	**Value**
Scintillator Type	LYSO
Ring Diameter	$150mm$
Axial FOV	$75mm$
Crystal Pixel Dimensions	$0.8 \times 0.8 \times 10mm^3$ $1.6 \times 1.6 \times 10mm^3$
Energy Window	$350 - 650keV$
Timing Window	less than $500ps$
Resolution/Crystal size	1
Randoms Correction	Calculated
Peak NECR[1]	$\sim 350Kcps$

Table 1.1: Small-Animal PET scan system performance requirement. [3].

1.1.2 Thesis Goals

The thesis mainly discusses six aspects of small-animal PET scan detector module based on MD-SiPMs.

1. To port the frame-based readout process (mode-0) from a Xilinx Virtex-5 evaluation kit (ML-507) to a new and advanced Xilinx Spartan-6 XCM-206Z-LX150 FPGA board provided by a Japanese company HumanData. The new FPGA board is quite compact (having dimensions of a credit card)[6].

[1]NECR is Noise Equivalent Count Rate. The total number of prompt coincidences recorded by the system is a summation of true, scattered and random coincidences. NEC is a parameter given by $\frac{T^2}{P}$, where T represents True coincidence count rate and P is the prompt coincidence rate observed.

2. To develop a new event-driven based readout mechanism (mode-2) for a fast readout process and thereby reducing the system dead time.

3. To develop the complete firmware for multiple chip readout along with temperature sensor readout.

4. To perform a complete electrical characterization and single photon timing resolution(SPTR) measurement for the time-to-digital converters(TDCs).

5. To perform radiation characterization with LYSO scintillator glued over the MD-SiPM array chip.

6. To explore the possibility of multiple timemark estimation for gamma event. This ensures a better image quality post reconstruction.

1.2 Thesis Outline

The thesis is aimed at discussing the system level design of a PET scan module. Chapter-1 starts with providing a brief introduction and overview of PET scan module and its system level requirements. It is followed by presenting the physics of PET, positron-electron annihilation, a concise discussion about preclinical basics of PET. State-of-the-art PET modules are discussed along with their limitations and scope of improvements in its design and architecture. Lastly, performance metrics like system sensitivity, dead time, energy and timing resolution, and associated non-idealities are explained.

Chapter-2 provides an in-depth knowledge of MD-SiPMs, its top level architecture, SPAD-cell array structure, SPAD-cell design and lastly, the photo-sensitive core of the pixel: single-photon avalanche diodes(SPADs). It is followed by a description of the TDC under use and its architecture. Next, the readout architecture is presented. The chip can be configured in two modes, namely, mode-0 and mode-2. Mode-0 is frame-based readout mechanism while mode-2 is an event- driven readout process.

Chapter-3 discusses the details of the firmware that is designed to perform the read-out both for a single and multiple chip configuration. Pixel and TDC data verification, temperature controlling and firmware expansion for multiple chip readout. In chapter-4, results for radiation characterization are presented. Chapter-5 explores the possibility of using multiple timestamps for gamma event for better image reconstruction. The thesis is concluded by Chapter-6 discussing the PET detector performance and its future roadmap.

1.3 Physics of Positron Emission Tomography

PET is a branch of medical imaging technique where the unique characteristics of some radioactive elements are exploited for imaging purposes. In PET scan systems, a patient is usually injected with a $\beta+$ decay radioactive compound (radiotracer). These radionuclides are produced artificially and are subsequently attached to compounds of biological interest [9, 4]. Many naturally occurring isotopes of elements, like carbon,

nitrogen, oxygen etc, exhibit $\beta+$ decay. These isotopes can be processed to design a variety of radiopharmaceuticals. Some typical radiotracers are presented in Table 1.2.

Isotopes	Tracer Compound	Typical application
^{11}C	Methionine	Oncology
^{13}N	Ammonia	Myocardial perfusion
^{15}O	Water	Brain activation studies
^{18}F	Flourodeoxy glucose	oncology, neurology, cardiology

Table 1.2: Radiotracers used in Medical imaging applications [4]

1.3.1 Positron-Electron Annihilation

In PET scan systems, a patient is given radiotracer labeled compound with a short half-life. The radionuclides present in the compound are undergoing $\beta+$ decay and emitting out positrons inside the subject. These positrons are in an electron rich surrounding medium. The positrons are emitted with a high kinetic energy and it rapidly loses all of its energy due to inelastic collisions inside the tissue [9]. Once the positron has lost most of its energy in inelastic interactions with the surrounding medium, it combines with an electron to form an *exotic atom* called positronium(Ps). Positronium is an unstable system which lasts no longer than 10^{-10} seconds [9, 14]. It is formed by an electron and positron which eventually results in an *annihilation*.

Annihilation is a process where a subatomic particle collides with its antiparticle and results in release of tremendous amount energy. As both electron and positron are almost in the state of rest while annihilation, the total energy dissipated can be attributed to the mass of the particles and is computed using Einstein's mass energy equivalence. In annihilation, the masses of both particles are converted into energy and can be calculated by the Eqn. 1.1

$$E_{released} = m.c^2 = [m_e + m_p].c^2 \tag{1.1}$$

Where m_e and m_p are the masses of an electron and positron respectively and c is the speed of light (3×10^8m/s). Positron, being an antiparticle of electron, has same mass as electron and opposite charge. Substituting their masses in the Eqn. 1.1, the amount of energy released during an annihilation event is calculated out to be $1.022MeV$.

The total energy released during annihilation process is in the form of high-energy radiations with very high frequency close to 10^{19}Hz. As both positron and electron are nearly in state of rest, the net momentum is close to zero and annihilation cannot result in high-energy photon emission as this will cause the net momentum to be non-zero in the direction of that photon [9]. Conservation of both energy and momentum dictates that two photons are emitted simultaneously in opposite directions each carrying half of the total energy released from the process. Thus, each photon acquires $511keV$, as total energy released during the annihilation process is $1.022MeV$, and since both are emitted out at 180° direction the net momentum is also conserved and is close to zero. The annihilation process is illustrated in the Fig. 1.1.

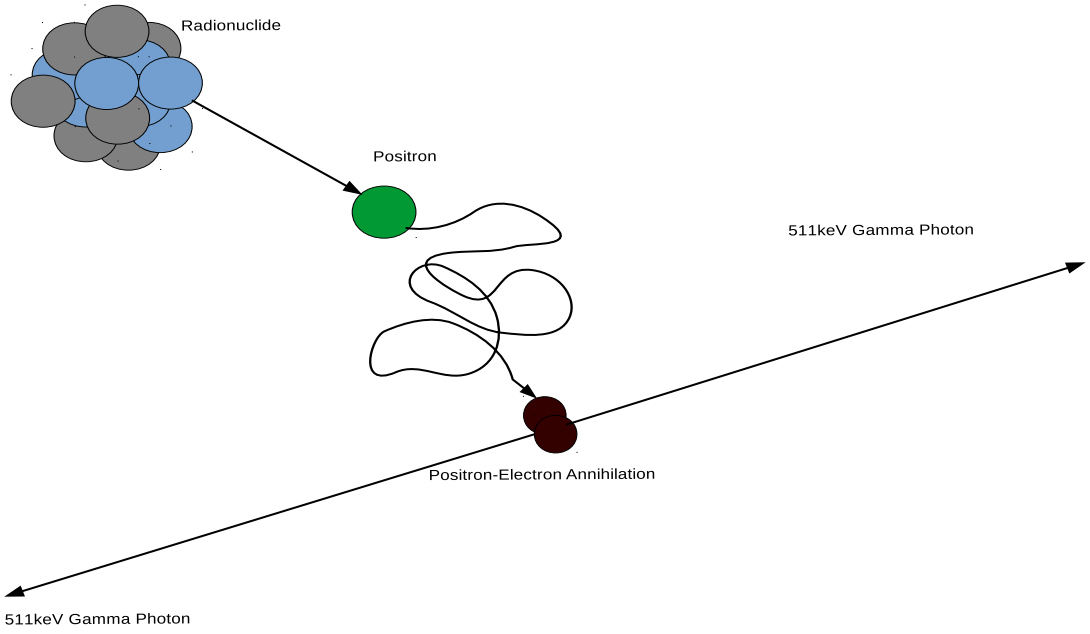

Figure 1.1: Positron-electron annihilation process resulting in emission of two gamma photons $180°$ apart and each possessing $511keV$ of energy

The high-energy photons($511keV$) generated as a result of annihilation process have a high probability of escaping through the subject's body for external detection. Thus, PET scan systems actually detect the gamma radiation and not the positrons themselves.

The PET scan system can be illustrated by Fig. 1.2. In the typical PET scan system, there is a ring of detectors and the subject, already injected with radiotracer, is placed at the detector ring's center. Gamma radiations that is emitted out of the subject's body is detected and a computed tomography scan is generated. As the two gamma photons emitted during an annihilation process obeys a specific geometric relation and similar energy profile, detecting both of them externally leads to localization of the annihilation site inside the subject's body. PET scan detectors, when triggered by a gamma photon, produces an electrical pulse. These electrical pulses are read and coupled by the coincidence electronics. If the leading edge of two pulses occurred within a small window of time, they are considered to be two gamma photons from same annihilation event i.e., coincident [4]. Once the gamma photon pair from a $\beta+$ decay event are detected, the line joining the two PET detectors will pass through the point where annihilation event actually occurred and hence, spatial information about point of occurrence can be estimated. This process of gathering positional information is called as *Electronic Collimation*. Electronic collimation is only possible because each positron emission and its subsequent annihilation produces two gamma photons traveling in opposite direction and with similar energy profile. Electronic collimation also

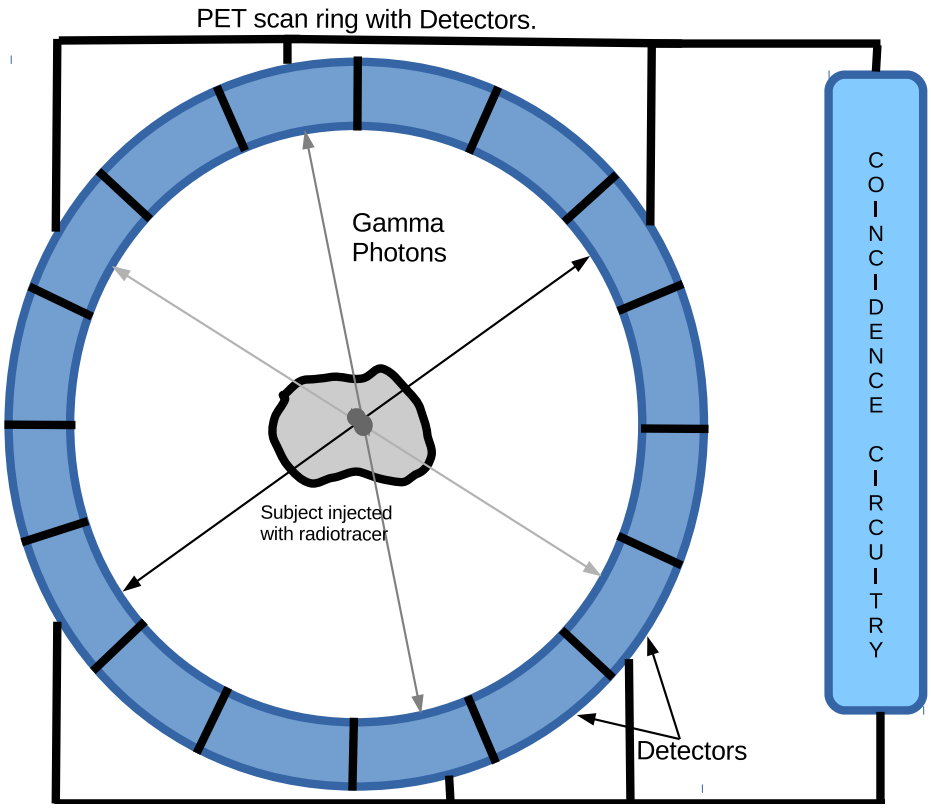

Figure 1.2: Positron Emission Tomography setup with a pair of detectors used to detect the two emitted gamma photons.

eliminates the need for a physical collimator which reduces the overall PET sensitivity by hindering events from being detected.

1.4 Preclinical PET Scan Systems

Clinical PET scan systems have been in medical use for treatment and diagnosis of human diseases such as cancer, melanoma, cardiovascular disorders etc. However, due to the cost and limited availability of clinical PET scan systems for research endeavours, preclinical PET scan systems have been designed and developed to further the scope of biomedical and pharmaceutical research. Preclinical PET systems are smaller in size and are designed for small animals like mice, rats etc. Preclinical PET scan systems with superior temporal and spatial resolution have enabled researchers to perform *in vivo* studies on complex biochemical processes that can help us in innovating new radiotracers or therapeutic agents to clinic.

Table. 1.3 lists some of the commercially available preclinical PET scan systems along with their important performance metrics. Due to smaller ring diameter for preclinical PET systems, the number of scattered coincidence events and attenuation is

[2]Full Width at Half Maximum (FWHM) at axial center

Manufacturer	Ring Diameter(mm)	Spatial Resolution[2] (mm)	Energy Window (keV)
Siemens Inveon	161	1.63	350-625
Philips Mosaic HP	197	2.32	385-665
Raytest ClearPET	135-225	1.94	250-650
Gamma Medica LabPET8	162	1.65	250-650
Bioscan/Mediso NanoPET	160	1.2	250-750
Carestream Albira	105	∼1.3	-

Table 1.3: Commercially available Preclinical PET scan systems and their reported performance metrics [3, 5].

lesser than clinical PET scanners. Typically, the reported scatter fractions for human PET systems is roughly 33% which is significantly higher than scatter fractions reported for preclinical PET systems with mouse(8%) and rat(17%) phantoms [5]. Also, the system sensitivity in preclinical PET scanners have been reported to be significantly higher than the conventional human PET scanners. Since the ring diameter of a preclinical PET is very small compared to human clinical PET, the designers elongated the preclinical PET gantry. With a long axial field of view (FOV), the number of detector channels available are still approximately same as human PET scanners. For instance, Siemens Inveon has 25600 detectors while Siemens clinical PET scanner, *Biograph PET/CT*, has 32,448 detectors [15]. Preclinical PET scanners have been reported to have 10% absolute sensitivity at axial center of FOV which is roughly 10 times higher than a clinical PET scan for humans [5]. Also, due to higher sensitivity, lower doses of radiotracers are quite sufficient to obtain detailed information without compromising the image quality [16].

The superior performance metrics as discussed above have enabled preclinical PET scanners to be used for a variety of research applications related to study of disease processes like cardiovascular anomalies, oncology, neurology etc. The preclinical PET scanners are now being integrated with state-of-the-art MRI scan systems to provide multi-modal studies enabling researchers to acquire soft tissue images along with detailed quantitative functional imaging data within one study.

1.5 State-of-the-art of Preclinical systems

At the heart of PET scan systems, a PET detector module is responsible for detecting, with reasonable precision, the gamma photons. Conventionally, scintillation detectors have been employed in the task of gamma photon detection. In scintillation detectors, a crystal scintillator is coupled with a photosensor to form the module. The first PET scan detectors were developed using Thallium doped Sodium Iodide (NaI-Tl) scintillator coupled with photomultiplier tubes (PMTs). Since then, there has been an ongoing research in design and development of new and improved scintillation detectors. PMTs are light sensitive devices with peak sensitivity in UV to near IR range of the electro-

magnetic spectrum. PMTs used in PET detection applications are designed to work with very high multiplication gain which is achieved by operating the PMTs at a very high biasing voltage. Also, PMTs are extremely sensitive to magnetic fields. If operated near a strong magnetic field source, a loss of gain can be observed as strong magnetic fields can bend the electron paths inside the PMTs and guide them away from dynodes.

Several research literature, [17, 18], suggest the use of multi-anode PMTs (MA-PMTs) and position sensitive PMTs (PS-PMTs). MA-PMTs comprises of an array of distinct PMTs coupled with a pixelated scintillator with each PMT providing an independent read out channel and PS-PMTs are capable of providing a segmented readout for X and Y directions. With technological advancements in semiconductor process technology, avalanche photo diodes (APDs) can be employed as primary photon detectors instead of PMTs. APDs are also insensitive to magnetic fields thereby enabling PET scan systems to be integrated with MRI systems to augment the functional imaging data obtained. Also, a smaller detector size enables designers to integrate more detectors for higher sensitivity and reduced deadspace [19].

With recent developments in SPADs, SiPM farms have been developed that can be used in designing PET scan detectors. There are two types of SiPMs: analog SiPMs and digital SiPMs. Analog SiPMs are based on the principle of deducing the number of incident photon from the total sum of avalanche current generated in the SiPM farm [20]. In analog SiPM, upon a photon interaction with the sensor, avalanche current is generated in the SPAD-cell. The avalanche current for all the SPAD-cells (the ones which are triggered) are added up into a single output. The resultant output current is proportional to the number of SPAD-cell fired. In digital SiPMs, on the other hand, the current pulse generated due to an avalanche is converted into a voltage pulse and stored as a bit information which can be further processed to count the total number of incident photons. As SPADs can be manufactured with standard CMOS process, their integration with other digital electronics is easier. The rise time of current pulse in SPADs upon illumination with a photon is in sub-nanosecond range. Also, compared to PMTs, SPADs operate at much lower bias voltage eliminating the need of high voltage power supplies [21]. In [1], a novel 9×18 MD-SiPM is designed for PET scan detectors. The design architecture details are discussed in chapter 2.

1.6 PET detector module for small-animal

There are certain performance metrics that needs to be taken care of while designing a PET scan systems. Performance metrics such as sensitivity, spatial and energy resolution, and timing resolutions are very critical to PET performance. These figure of merit are often interdependent. Following subsections discuss about these parameters and how they affect the quality of reconstructed image.

1.6.1 Sensitivity

The efficacy of a PET scan system depends greatly on the number of coincidence events it detects which is consequently used for image formation. One of the major challenges

of designing a PET system is to maximize the *system sensitivity*. *System sensitivity* is defined as the number of coincidence events detected per second in a specific phantom containing an unit of radioactive concentration ($cps/Bq/ml$) [9]. As the amount of radioactive tracer that can be administered to a subject is fixed, system sensitivity is highly dependent on detector and geometric efficiency of the PET scan system, dead time, etc.

The detector efficiency, ξ, is a product of photon detection probability of the sensor and the fraction, Φ, of incoming photons falling in the energy window of interest. The energy window ranges from 350keV to 650keV [9, 22]. The detector efficiency alone cannot be used reliably for registering a valid gamma event. In positron annihilation, two gamma photons are emitted by the annihilation process. Thus, to register a valid gamma event, both the gamma photons need to be detected by detectors on opposite side within the energy specified in energy window. Therefore, the resulting efficiency is termed as *coincidence detection efficiency* and is the square of detection efficiency.

The other factor playing an important role in determining the overall system sensitivity is the *geometric efficiency* of the detector itself. Geometric efficiency depends on how seamless detectors are integrated into the PET scan system i.e., packing fraction, and the absolute solid angle coverage of the detectors [9].

1.6.2 Dead Time

PET scan systems are generally operated in event-driven read out mode where the detectors are activated to capture a gamma event and upon a valid gamma event registration, a read out is performed. During the readout process, the detectors are deactivated and hence cannot be used for gamma detection till the readout is complete. Thus, the time taken to read out the complete detector is termed as system *Dead Time*. Dead time plays a vital role in overall system performance as a higher dead time will lead to less gamma events being detected.

1.6.3 Energy Resolution

The gamma photon emitted out of an annihilation event possess a constant energy of 511keV. Thus, the detectors designed for PET scan system must be optimized to have very high efficiency for registering gamma photons falling in the mentioned energy range. Typically, the energy range employed in conventional PET scan system lies within $350keV$ to $650keV$. The reason for having an energy window extending both ways from $511keV$ is the fact that a scintillation's response towards gamma photons is not ideal and possess some limited resolution. The FWHM for energy response is around 15% and to account for this non ideality, a range of energy is chosen for gamma detection. The energy window is selected in such a way that gamma photons emitted out of an annihilation event are detected while the photons that have scattered inside the body and have lost part of their energy are filtered out. To convert high-energy gamma photons into visible light photons, scintillators are utilized. Scintillators are transparent materials that generate visible light photons upon absorbing an incident high-energy gamma photons. Choice of scintillators is one of the factors that define the energy window for a particular PET scan system as they are differentiated by stopping

power, rise and decay time i.e., how fast the incident high-energy photon leads to emission of visible light photons, and the wavelength of generated visible light photons.

1.6.4 Spatial Resolution

Spatial resolution is another crucial figure of merit for small PET scan systems. Empirically, it is defined as the ability of a scanner to clearly detect two points in an image distinctively. A higher spatial resolution is desirable for high quality image reconstruction in PET scan systems. But, spatial resolution cannot be increased arbitrarily and it depends on detector size which is one of the most important aspects in addition to some intrinsic limitations like positron range, non collinearity, etc.

In a PET scan system, a valid gamma event is registered when two gamma photons from a single annihilation event are detected. Due to a finite detector size, the annihilation event can exist anywhere in the volume of response (VOR). An array of very small detectors or a large detector with position sensing capability can help in increasing the spatial resolution of the PET scan systems [9, 4]. Designing a very small detector with acceptable detection efficiency is often difficult and hence detectors are coupled with pixelated scintillators to achieve a finer spatial resolution.

1.6.5 Timing Resolution

Timing resolution is defined as the ability of a PET scan detector to estimate the precise time of arrival of gamma photon. The system timing resolution depends on the photosensor's intrinsic timing resolution of detecting visible light photons and the scintillator's rise and decay times denoted by t_r and t_d respectively, etc. Thus, scintillator choice is particularly important in designing PET scan detector.

Spatial resolution only narrows down the position of annihilation event to within a VOR. VOR still does not accurately position the event. To further localize the annihilation site, a straight forward method of calculating time of arrival of the first photon produced upon a gamma photon absorption inside the scintillator is applied. This approach is often referred to as Time-of-Flight (TOF) [9]. In TOF-PET scan system, accurate positional information can be gathered by measuring the time difference in the arrival of two gamma photons on the opposite detectors. Once the timing information is available, the position of annihilation site can be estimated. If the point of occurrence is at a distance d from the center of line joining the two detectors and the difference in time of arrival of two gamma photons is ΔT, then the point of annihilation can be given by the Eqn. 1.2.

$$d = \frac{\Delta T \times c}{2} \tag{1.2}$$

1.6.6 Non-Idealities

In PET systems, coincidence detection is a crucial process. Under practical circumstances, there are undesirable events that can lead to false-positives. Ideally, only true coincidences i.e., two gamma photon from same annihilation event, are detected and contribute to image reconstruction but practically, there are scattered, random and

multiple coincidence that are simply noise and degrade the image quality. Fig. 1.3

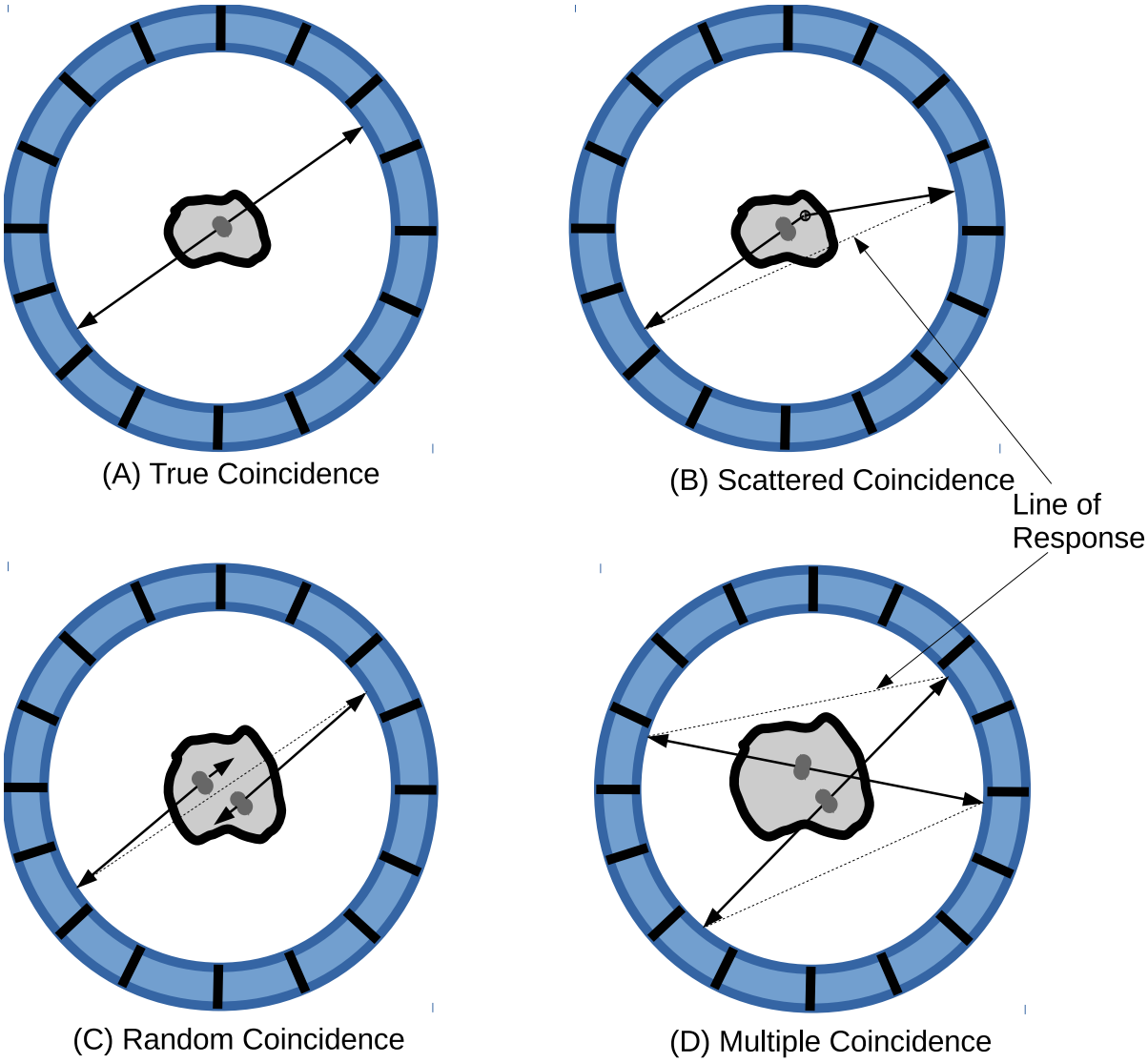

Figure 1.3: (A) True Coincidence. (B) Scattered Coincidence. (C) Random Coincidence. (D) Multiple Coincidence.

shows 4 major types of coincidences that are possible. True coincidence are of interest as they are comprised of two gamma photons generated out of the same annihilation pair and the gamma photons managed to escape the subject's body for external detection. Fig. 1.3(B), (C) and (D) are undesirable events that leads to false-positives. In scattered coincidence, one of the two gamma photons generated changes its direction due to interactions inside the body (Compton scattering). This leads to a false VOR that results in a degraded spatial resolution. Random coincidence is generated due to two gamma photons reaching the detector within time window but they belong to

different annihilation events. Multiple coincidences happen when more than 2 detectors report an event within the same time window and ambiguity arises in performing localization. Usually, multiple coincidences are disregarded and does not contribute in image formation.

2 Multichannel Digital SiPMs

A photon time-of-arrival (TOA) is central to PET applications. The term "Multichannel" points to the fact that digital SiPM is designed with more than 1 TDC. In fact, the MD-SiPM discussed in this thesis has 48 TDCs per MD-SiPM per column. The chapter is divided into four sections. First, a brief overview of the monolithic array of 9×18 MD-SiPM architecture is provided. Second, SPAD-cell array and SPAD are discussed along with non-idealities associated with SPADs. Next, the TDC architecture is discussed. Lastly, the read out architecture is explained. A basic overview of modes of chip operation is presented in the read out architecture. The associated details are discussed in chapter-3 which deals with firmware development and data verification.

2.1 Architecture

The complete chip is designed in a 9×18 two dimensional MD-SiPM array with associated digital logic. The total SPAD-cell resolution achieved is 468×144. Fig. 2.1

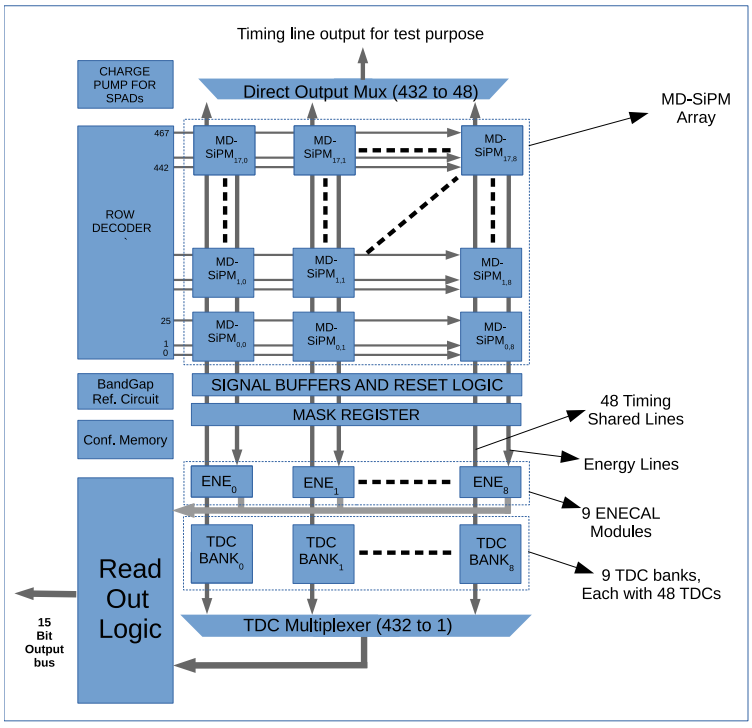

Figure 2.1: 9×18 MD-SiPM array chip [1]

shows the complete chip block diagram that contains 9×18 MD-SiPM monolithic array,

energy calculation module, 9×48 TDCs, readout multiplexers, configuration memory unit, row address decoder and bandgap reference generation circuit. 0.35μm HV-CMOS technology is utilized for 9×18 MD-SiPM array chip fabrication. The chip dimensions are $7.6mm \times 17.1mm$ with each MD-SiPM acquiring $800 \times 780\mu m^2$.

A novel reset technique is employed in the design called the *Smart Reset* which sits inside the signal buffer and reset logic module. As 48 timing lines are shared column-wise in the MD-SiPM array, there can be a situation where most of the TDCs are occupied by the SPAD firings due to DCR. Thus, the effective time for actual photon detection reduces. To solve this issue, smart reset technique is employed where the reset is performed only on the SPAD-cells and TDCs that were triggered due to DCR.

The row address decoder module is responsible for generating the row addresses while the readout is performed. A digitally controlled charge pump is also implemented for providing high voltages to the SPAD-cell array. A 6-bit digitally controlled oscillator (frequency ranging from 43.7MHz to 1.2GHz) is implemented for clocking the charge pump [1]. A mask register is implemented to store the masking information which is used to deactivate *Screamers*[1]. This is done to reduce the spurious TDC firings. In order to provide precise biasing voltages to the TDC, a band-gap reference circuit is implemented. The chip's configuration settings are stored in the configuration memory unit which receives its data from FPGA firmware controlling the chip. Lastly, a TDC readout multiplexer and read out logic is implemented to route the data coming from 432 TDCs and energy calculation module onto the output 15-bit bus.

2.2 SPAD-cell Array

The MD-SiPM is designed in a two dimensional 26×16 SPAD-cell matrix with column parallel TDCs. The SiPM SPAD-cell contains a SPAD and associated digital circuit. In the next section, the fundamental design and working principle of a SPAD are discussed. Next, the SPAD-cell structure is explained and lastly a brief description of complete MD-SiPM SPAD-cell array is provided.

2.2.1 Single-Photon Avalanche Diodes

Single-photon avalanche diode (SPAD), as the name suggests, is a class of photo-detector diodes designed to detect single incident photon. SPADs are solid-state P-N junction diodes designed to work well above its reverse breakdown voltage. Also referred to as Geiger-mode avalanche photodiodes(G-APDs) in some literature, fundamentally they are P-N junction diodes capable of withstanding high electric field due to high reverse bias voltage [24].

A P-N junction, shown in the Fig. 2.2, is a boundary between two types of semiconductor devices, namely, a P-type region and a N-type region. Both P-type and N-type regions are fabricated from silicon wafer with different doping profiles. While P-type region is designed to have holes as majority charge carriers, the N-type region has higher electron concentration. Doping process is done under controlled environment

[1] *Screamers* are SPAD-cells which have a very high DCR resulting in TDCs firing and, thus, reducing the number of available TDCs for actual photon TOA measurement.

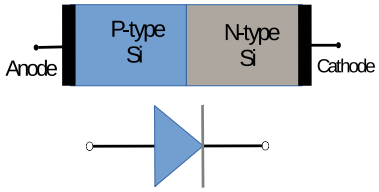

Figure 2.2: A P-N junction diode

via diffusion or ion implantation[25].

A SPAD, as mentioned earlier, is a special class of P-N junction diodes which are specifically fabricated to withstand reverse biased voltages above its breakdown voltage (V_{br}) [24]. With the diode being operated with such a high external electric field, a single charge carrier, if injected in the depletion region, can set off an avalanche process due to impact ionization. If the charge carrier triggering the avalanche is a photo-generated one then the reverse biased P-N junction can be considered as a photon detector. In a SPAD-cell, the diode is surrounded by ancillary digital circuit designed for performing below mentioned tasks.

1. Applied external voltage (V_a) is increased so that it becomes higher than the breakdown voltage (V_{br}). At this moment, the SPAD is activated for single-photon detection.

2. Once a SPAD detects a photon, the digital circuit is designed to sense rising edge of the current pulse generated due to the avalanche and converting it into a asynchronous voltage pulse.

3. Upon trigger, the SPAD is in avalanche and needs to be quenched in order to reuse it for further detection. The digital circuit brings down the applied voltage below the breakdown to cease the avalanche process in case of active quenching.

4. Finally, once the avalanche is quenched, the SPADs are re-activated by restoring the applied external voltage above its breakdown i.e., $V_a > V_{br}$.

Photon Detection Probability

Photon detection in SPADs rely on avalanche dynamics. In a p-n junction diode (Fig 2.3), an incident photon can either fall on the depletion region or the neutral regions (p or n substrate). If a photon with sufficient energy falls on the active area of the SPAD (depletion region), then it can potentially generate an electron-hole pair which, in turn, may trigger an avalanche [26]. Since single-photon detection is a stochastic phenomenon, the SPAD's sensitivity towards single-photon detection is measured by means of probability [27].

Thus, photon detection probability (PDP) may be defined as the probability of a photon initiating an avalanche upon falling on SPAD.

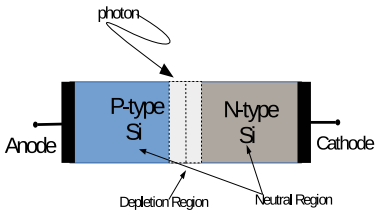

Figure 2.3: P-N junction diode with depletion region.

Dark Count Rate (DCR)

A charge carrier causing an avalanche process can either be a thermally generated, photo-generated or could be due to tunneling effect because of high electric field at the p-n junction [27]. The electrical pulse produced by the SPAD, upon firing, is identical irrespective of what initiated the avalanche process. Thus, if a SPAD is kept in absolute darkness and is triggered by a thermally generated charge carrier an output will be recorded even though there is not a single photon. This resulting average number of counts per second is termed as dark count rate, abbreviated as DCR.

The DCR is rather an important figure of merit so far as efficacy of SPAD is concerned. The inverse of DCR represents mean time difference between two successive SPAD firings. During the time between the two SPAD firings, it is biased above its breakdown voltage and is armed for photon detection. A lower DCR means higher mean time difference between two undesired SPAD firings and hence a higher time for which it is activated for photon detection. Therefore, for a SPAD to work efficiently as a single-photon detector it must have a lower DCR. In addition, spurious firing can have a significant impact depending on the application.

Afterpulsing

A photon, if injected into the depletion region, can trigger a self-sustaining avalanche process. During an avalanche event, some charge carriers which are generated by impact ionization may get trapped in defect sites within the depletion region [24]. The hold off period for these trapped carriers is in the nanosecond range. These trapped charge carriers, if liberated while the SPAD is still in the quenching process, can cause a second avalanche pulse. [27]. This correlated second pulse is known as Afterpulsing.

Afterpulsing determines the time for which the SPADs need to be in quenched state before being used again for photon detection. The time for which the SPAD is in shutdown mode is known as *Dead Time*. Also due to correlated nature of afterpulsing, it is particularly catastrophic for certain SPAD applications such as true random number generation and quantum key distribution.

Quench and Recharge circuitry

The avalanche breakdown process is self-sustaining in nature i.e., it continues so long as the applied reverse bias voltage (V_a) is above the breakdown voltage (V_{br}). A continuous flow of avalanche current can be potentially damaging. Also, the SPAD cannot be

used again for photon detection while it is avalanche breakdown mode and, hence, the avalanche needs to be extinguished. Quenching and recharge circuitry is used to first quell the avalanche by reducing the V_a to a level lower than V_{br} and then raising V_a back to a value above V_{br} so that the SPAD is again ready to be triggered by another photon. The hold off time between the onset of avalanche, its subsequent quenching, and recharging is the dead time and denoted by T_d. In order to efficiently use SPADs as single-photon detectors, the dead time must be as small as possible but it cannot be reduced indefinitely. Dead time is governed by several factors like time taken to quench and recharge SPADs and afterpulsing. Decreasing dead time can increase afterpulsing probability and hence induces correlated noise.

Passive Quenching and Recharge Technique

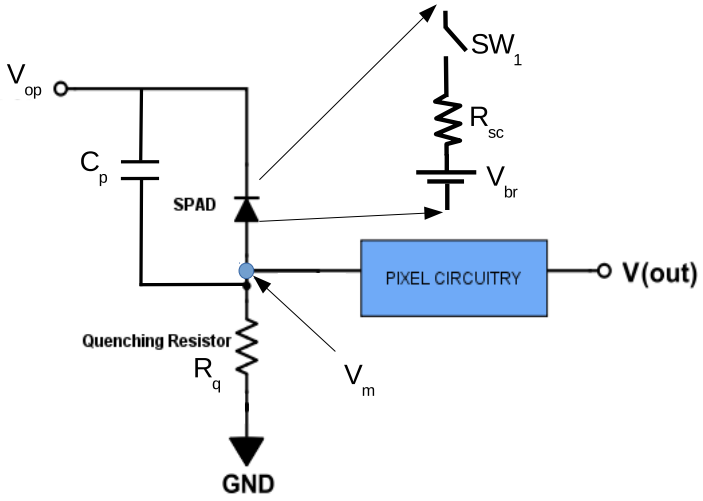

Figure 2.4: Passive Quench and Recharge Circuitry.

The simplest way of quenching a SPAD is to have a large resistor, typically ranging from 100KΩ to 1MΩ, in series with the diode [27]. Fig 2.4 shows the simplest technique for quenching and recharging SPADs. It is a passive solution where a quenching resistor and parasitic capacitance C_p (total capacitance seen across the diode including junction capacitance) forms a RC circuit. The space-charge resistance, denoted by R_{sc}, exhibited by the SPAD in avalanche breakdown mode is far less than the quenching resistance. In the idle condition, there is no avalanche current and diode is biased above its breakdown and the capacitor C_p is charged to a voltage V_{op} which is also the voltage across the diode.

On the start of the avalanche (closing of switch SW_1), the current build up is almost instantaneous and rises to a value given by Eqn 2.1. At this point, the capacitor C_p starts to discharge and, thus, the voltage at V_m increases. Once V_m reaches $V_{op}-V_{br}$, the diode is no longer biased above V_{br} so the avalanche cannot continue and extinguishes. The discharging time (also the quenching time) T_q of the capacitor C_p is determined

by Eqns 2.2(a),(b) and (c).

$$\begin{aligned} I_a &= \frac{V_{op} - V_m - V_{br}}{R_{sc}} \quad (since\ initially\ V_m = 0V) \quad (a) \\ I_a^{max} &= \frac{V_{op} - V_{br}}{R_{sc}} = \frac{V_e}{R_{sc}} \quad (b) \end{aligned} \tag{2.1}$$

$$\begin{aligned} T_q &= R_{eq} \times C_p \quad where\ R_{eq}\ is, \quad (a) \\ R_{eq} &= \frac{R_{sc}.R_q}{R_{sc} + R_q} \quad if\ R_q \gg R_{sc}, \quad (b) \\ T_q &\approx R_{sc}.C_p \quad (c) \end{aligned} \tag{2.2}$$

Once the SPAD is completely quenched, the current flowing through the diode drops to a very low steady value denoted by $I_a^{steady\_state}$. The steady state current is given by the Eqn 2.3(c)

$$\begin{aligned} I_a^{steady\_state} &= \frac{V_{op} - V_{br}}{R_{sc} + R_q} \quad (a) \\ I_a^{steady\_state} &= \frac{V_e}{R_{sc} + R_q} \quad if\ R_q \gg R_{sc}, \quad (b) \\ I_a^{steady\_state} &\approx \frac{V_e}{R_q} \quad where\ V_e = V_{op} - V_{br} \quad (c) \end{aligned} \tag{2.3}$$

The Fig. 2.5 shows the transient behaviour of the diode. In Fig. 2.5(a), we observe the steep rise of short-circuit current upon avalanche initialization and the maximum short-circuit current (I_a^{max}) reaching to a value given by Eqn. 2.1(b). The exponential current decay attributed to discharging of capacitor C_p can also be observed. In Fig. 2.5(b), we observe the voltage rise across the quenching resistor R_q because of capacitor discharging and the quenching time (T_q) is given in Eqn. 2.2(c).

At time $T = t_x$, the quenching has finished and recharge phase starts. Once the avalanche is quenched(marked by opening of switch SW_1), the current flow drops to $0A$ and the diode acts like an open circuit. The capacitor C_p that is discharged to a potential of $V_{op} - V_{br}$ now begins to charge via quenching resistor R_q. The charge time is governed by the Eqn. 2.4. The recharge time can be reduced by reducing the quenching resistor R_q but this is in contrast to the requirement for faster quenching time as suggested in Eqn. 2.2(b) [27].

$$T_r = R_q \times C_p \tag{2.4}$$

Active Quenching and Recharge Technique

In order to reduce the quench and recharge time and thereby having a shorter dead time, active quenching and recharging methods are employed. In active quench mechanism, shown in Fig. 2.6, upon the avalanche initialization(marked by closing of switch SW_1), the avalanche current starts to flow and discharge the capacitor C_p. At the same time, the current pulse is sensed and a feedback is provided in form of a gated pulse ($\bar{Q}$) to

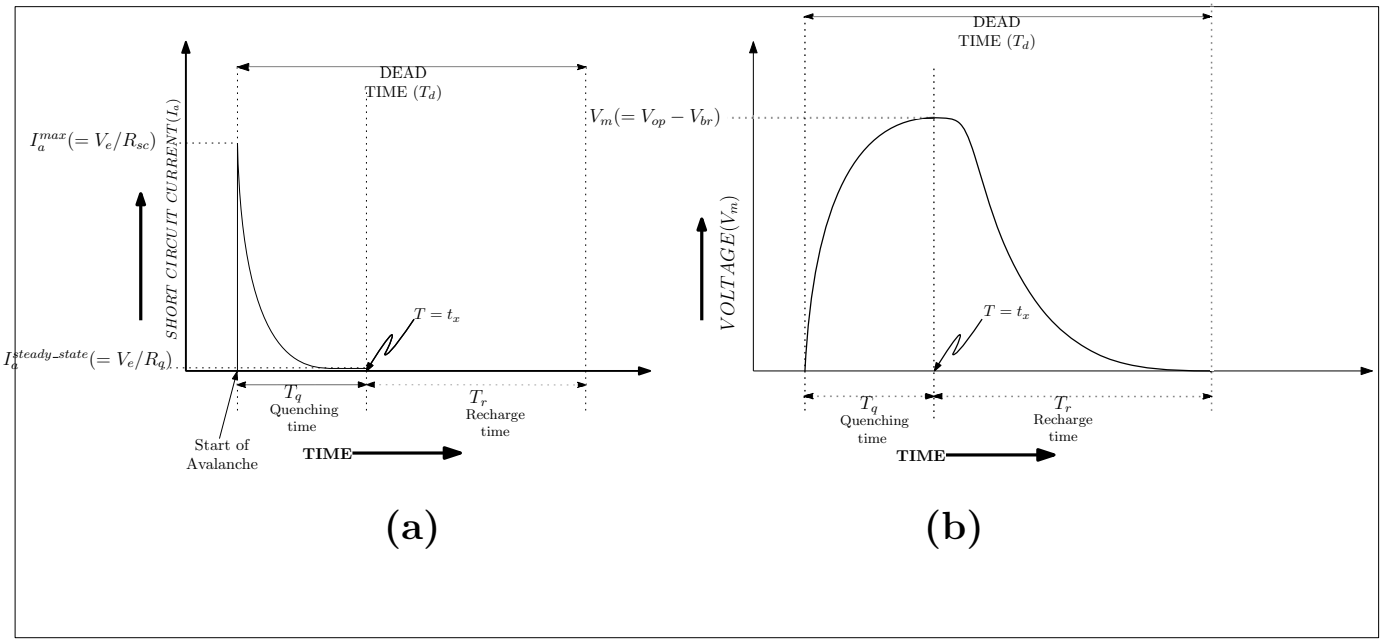

Figure 2.5: Transient behaviour of passive quenching and recharge operation [27]. (a) Short-circuit current versus time. (b) Transient behaviour of voltage across quenching resistor.

the quenching transistor $Q1$. The potential at V_m, which was originally at 0V prior to avalanche initiation, rises and settles to a value V_QUENCH. This value is adjusted in order to bring the diode bias below V_{br} necessary for extinguishing the avalanche. The quenching time T_q of the diode is total time it takes to sense the avalanche current

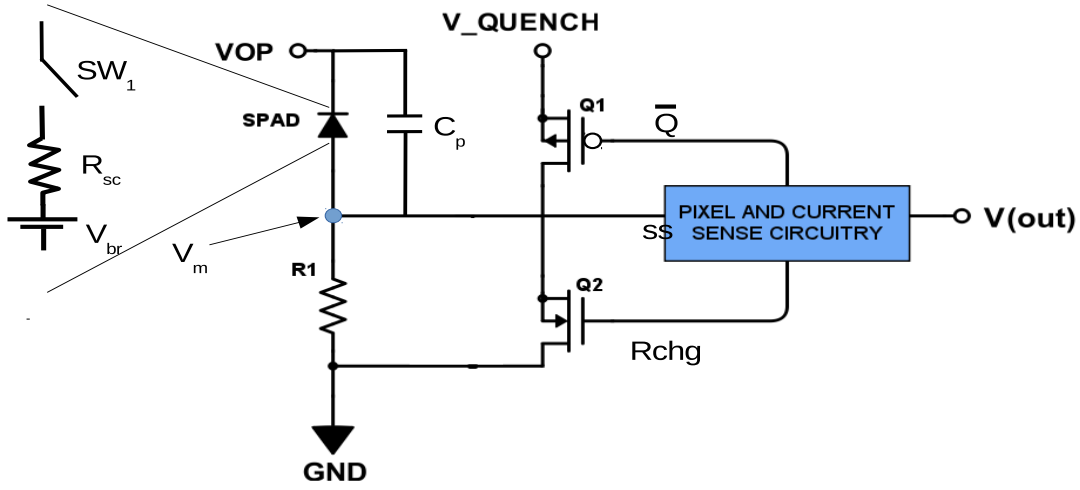

Figure 2.6: Active quenching and recharge circuit

and issue the quench pulse via $\bar{Q}$. Thus, the quenching time T_q is given by Eqn. 2.5(b).

$$\begin{aligned} T_q &= T_3 + T_1 && (a) \\ T_q &= C_p \times (R_{sc} + R_{Q1}^{on}) && (b) \end{aligned} \tag{2.5}$$

In the recharge cycle, as soon as $\bar{Q}$ is de-asserted, the capacitor C_p starts to charge itself via resistor R_1 to V_{op}. The recharge pulse can be asserted after a short delay of hold time denoted as T_4. Once the recharge pulse is asserted, the capacitor C_p charges rapidly because the on-state resistance of the transistor $Q2$ is very small and thus provides a smaller time constant. The total recharge time is given by Eqn. 2.6

$$\begin{aligned} T_r &= T_4 + T_2 && (a) \\ T_r &= C_p \times (R_1 + R_{Q2}^{on}) && (b) \end{aligned} \tag{2.6}$$

Fig. 2.7 shows the transient behaviour of the diode. From Fig. 2.7, the total dead time T_d for the SPAD is given by Eqn. 2.7. The hold time, T_4, can be varied by appropriately adjusting the SPAD-cell and current sense circuitry. User configurable hold time is an important aspect as it can be useful in certain experiments and measurements where longer dead time is required, usually to suppress afterpulsing probability [27].

$$T_d = T_q + T_r = C_p \times (R_1 + R_{sc} + R_{Q1}^{on} + R_{Q2}^{on}) \tag{2.7}$$

2.2.2 SPAD-cell Design

The cell is designed using the SPAD with additional digital logic responsible for various tasks to have a correct cell functionality along with safe device operation. Fig. 2.8 shows the single SPAD based cell circuit design. Each SPAD is complemented with digital read out logic and masking circuitry. Each cell has a 1-bit counter and mask circuit which is essentially a 1 bit storage element designed as cross-coupled inverters. The cell also has associated quench and memory latching logic. The mask logic is added in every cell to have the ability to shutdown individual cells in case if they have DCR higher than the average. The overall SPAD-cell array fill factor is 57% resulting in reduced photon misses [1]. The silicon real estate taken up by each cell is $50\mu m \times 30\mu m$.

The masking logic consists of two inputs, namely, $MASK$ and $MASKDATA$. The $MASKDATA$ is latched into the mask memory upon asserting $MASK$ signal. A digital '1' logic activates the cell while '0' deactivates it. A global reset is also provided to perform a complete cell array reset via RST which recharges the SPADs before start of each frame. The timing line and energy line are pulled up with PMOS transistors Q_8 and Q_9 controlled via PRE. $ROWCALSEL$ is kept activated all the time except during DCR measurement for generating the masking profile. This measurement is done prior to start of the frame to make sure that the *screamers* are masked. When an incident photon is detected, the generated digital pulse pulls down the timing line. The digital pulse can also be latched into the 1-bit counter by activating SET and this counter can be read out by issuing ROW signal.

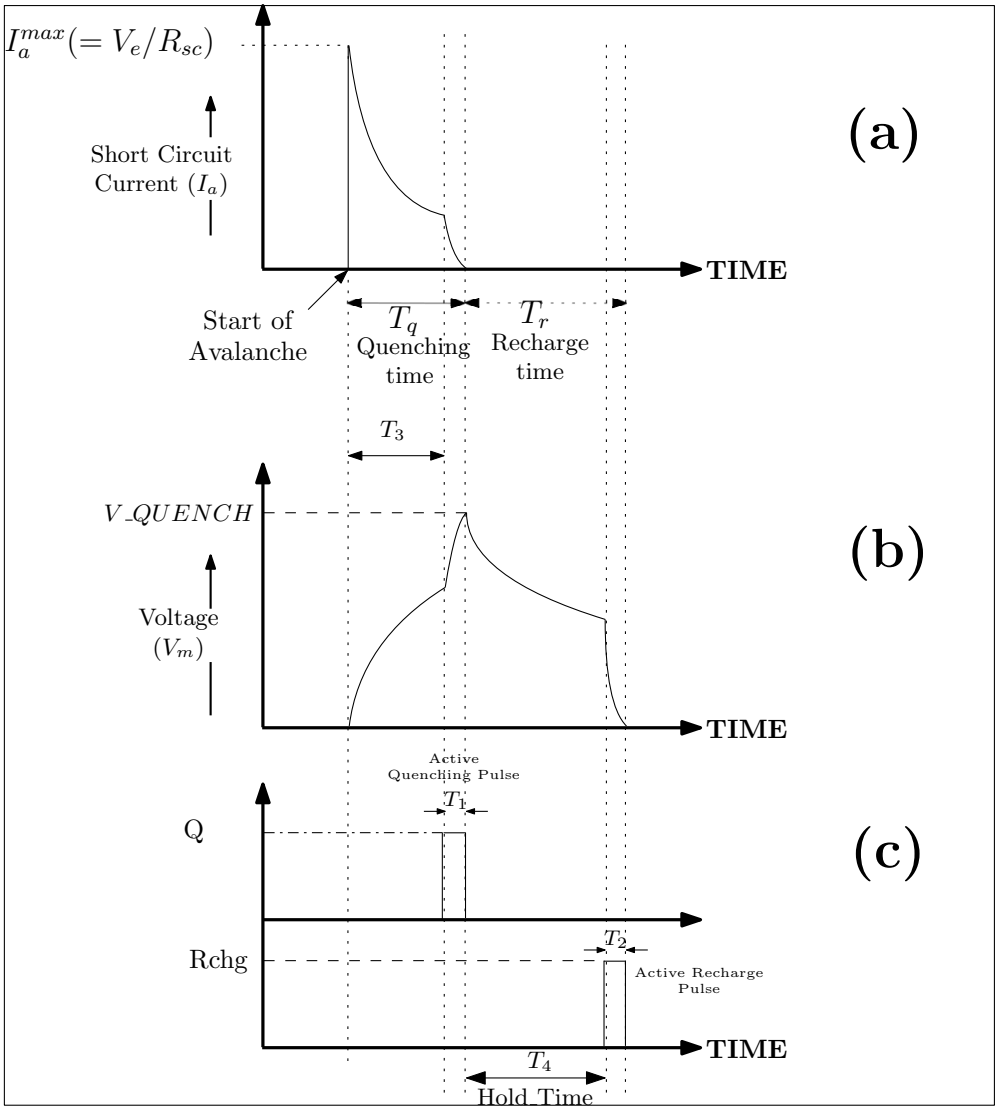

Figure 2.7: Transient behaviour of diode with active quenching and recharge mechanism [27]. (a) Short-circuit current versus time. (b) Voltage across quenching resistor. (c) Quench and recharge pulse generated by the current sense circuitry.

2.2.3 MD SiPM Pixel Array

The MD-SiPM SPAD-cell array is designed in a 26×16 2-dimensional matrix. Fig. 2.9 shows the MD-SiPM architecture with column-parallel TDCs and an energy calculator module. The array is designed with energy line being shared per SPAD-cell in each column while the timing line is shared per 3^{rd} cell every column. Thus, in total there are 16 energy lines going into the "ENECAL" module. As every column has 26 cells, there are 3 TDCs per column making a total of 48 TDCs in the bank for the complete MD-SiPM unit.

A gamma photon upon interaction with a scintillator produces visible light photons inside the scintillator and the number of produced photons is proportional to energy

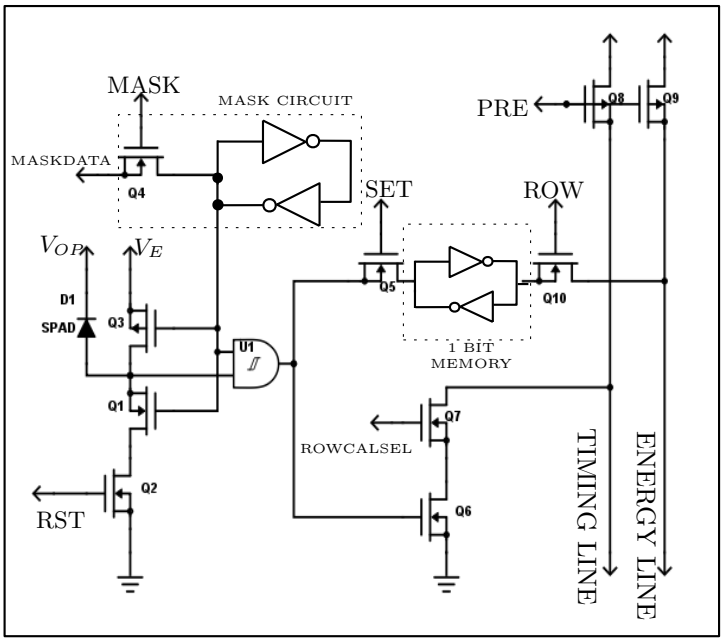

Figure 2.8: Pixel schematic.

of the gamma photon after saturation correction. Thus, an energy calculator unit is also added in every MD-SiPM module which adds up all the cell bits. The resulting digital count can be read out from the "ENECAL" giving us an estimate of gamma photon energy. The "ENECAL" module can count upto 416 SPAD firings. The module is equipped with a programmable threshold for energy count known as ENE_{TH}. The idea behind having this threshold is to avoid DCR from saturating the counts. The module is kept activated for a certain time, which can be programmed, if the energy counts is less than the threshold, the count is considered to be DCR and discarded. A reset is performed and the MD-SiPM re-initialized for next cycle.

Each MD-SiPM has 48 timing lines which are used for detecting photon resulting from a gamma event. As the MD-SiPM is kept activated, the DCR can saturate the timing lines. To avoid this from happening, the smart reset technique is adopted where the cell array undergoes a reset if the number of timing lines fired is less than a programmable threshold called as TDC_{TH}. The *smart reset* algorithm can be summed up in the following steps:

1. The frame start after a global reset is performed.
2. After a specific interval of time ($SR_{INTERVAL}$), which is externally programmable, the number of TDC timing lines fired is compared against a threshold (TDC_{TH}).
3. If the number of fired TDCs is higher than the threshold, the frame continues and an event flag is set to '1'.
4. If the number of fired TDCs is lower than the threshold, event flag is set to '0' and only the fired TDCs and SPAD-cells are reset. This reset is different from the global reset performed at the very beginning in a sense that this only resets the

SPAD-cells and TDCs that were fired due to DCR while other SPAD-cells and TDCs are still activated for photon detection.

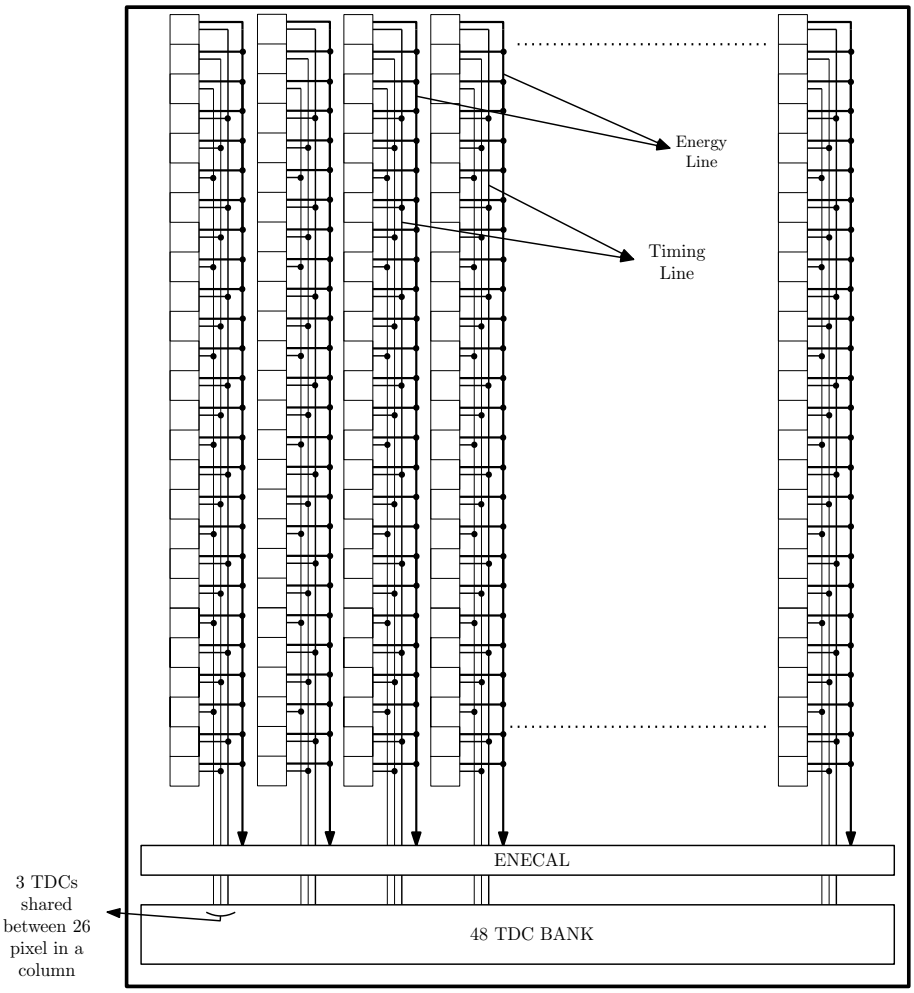

Figure 2.9: Schematic of the MD-SiPM pixel array.

2.3 Time-to-Digital Converters

In order to pinpoint, with reasonable accuracy, the location of annihilation event, we need knowledge of time of arrival of the gamma photon. For this purpose, a TDC is employed.

The primary goal of a TDC is to measure the time gap between the rising edge of two signals, namely, *Start* and *Stop*. In the simplest of implementation, a TDC can be visualized as a digital counter with an extremely high clock frequency. The *Start* pulse activates the counter and it starts counting and the *Stop* signal is used to latch the counter value. Knowing the output of the counter and multiplying it with the clock period gives us the time gap between the activation of *Start* and *Stop* pulse. Thus, the resolution of such a TDC will be the clock period of the system as the counter output is

quantized to integral multiples of clock cycles. To achieve sub-nanosecond resolution, a simple counter approach is not feasible and fine counters are designed where the time is measured using the propagation delays of transistor gates [28].

In the basic design of TDC, a chain of well designed buffer, with accurate and uniform propagation delay time τ, is utilized for time measurement. *Start* pulse travels through the buffer chain and *Stop* pulse is used to latch the buffer outputs into registers. The latched output is in the form of thermometer code and is converted into binary output. The output when multiplied with the propagation delay time τ of a single buffer gives the time gap between the rising edge of the *Start* and *Stop* pulse. Depending on the process technology, buffers with very small gate propagation delay, in pico-second range, can be designed thereby giving a pico-second range resolution in time measurement.

2.3.1 TDC Architecture

In 9×18 MD-SiPM, to achieve a higher dynamic range and higher temporal resolution a two-stage architecture is adopted. The TDC is designed with a 12 bit coarse counter with a temporal resolution of $1.58ns$ and a phase detector acting as 5-bit fine counter with a LSB of $49ps$. Together, they make up a 17-bit TDC with a temporal resolution of $49ps$ and a dynamic range of about $6.4\mu s$.

The chip integrates a column-parallel TDC with a common voltage-controlled-oscillator (VCO) for phase generation. The column-parallel TDC is achieved with a $16\mu m$ pitch and each TDC occupies $16\mu m \times 850\mu m$ area over silicon. Each cell could have had an independent TDC but that would drastically reduce the fill-factor and consequently hamper the photon detection efficiency of the array. Thus, a column-parallel TDC approach is adopted where every 3^{rd} SPAD-cell in a column share a TDC as shown in the Fig. 2.9. Another design novelty is use of a common VCO for all the TDCs instead of an independent VCO per TDC. A common VCO with phase repeaters for all TDCs eliminates LSB variations per TDC as these variations can become significantly large with imperfect frequency matching [1].

Fig. 2.10(a) shows the block diagram of the TDC bank that is implemented in the 9×18 MD-SiPM array chip. The TDC bank is designed with 432 TDCs and 1 *Dummy TDC*. All the TDCs receive the phase signals (ϕ_0, $\overline{\phi_0}$ through ϕ_3, $\overline{\phi_3}$) from the common VCO. The bandgap reference circuit is responsible for supplying the necessary biasing voltages to the TDCs and VCO.

Fig. 2.10(b) shows the TDC architecture where the $Start_i$ (i denotes the i^{th} TDC), which is the timing output line of the SPAD-cell, marks the detection of an incoming photon on one of the connected SPADs. Furthermore, it is used to generate two enable signals (ENB_1 and ENB_2). ENB_1 and ENB_2 are generated in a way that they have a phase difference of $\Delta t = LSB$ and they are responsible for activating the two identical phase detector modules. At the end of VCOEN cycle, the TDC coarse counter value and phase detector values are latched. The 2 phase detector modules are used to generate 32 distinct phases in the fine counter. Thus, the phase detector resolution turns out to be 5 bits and the coarse counter is 12 bits, making the dynamic range of the TDC to be 17 bits with LSB of $49ps$.

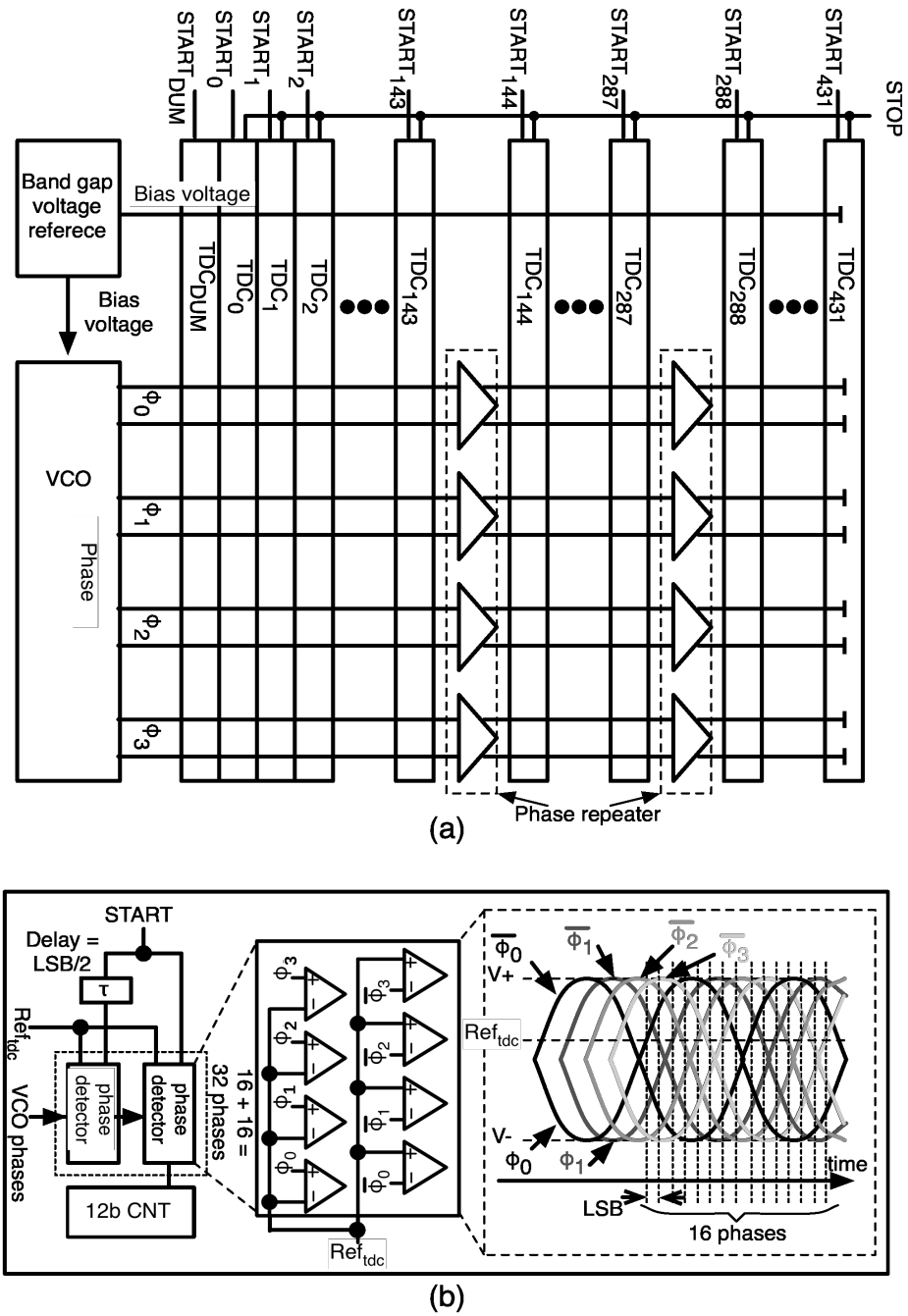

Figure 2.10: (a)Block diagram of a 432 column-parallel TDC including a dummy TDC. (b) TDC architecture [1].

2.4 Read-out Architecture

The chip supports two operation mode:

1. A complete chip readout mode: ***MODE-0***.

2. A fast readout mode: ***MODE-2***.

2.4.1 Mode 0

Mode-0 is a complete chip readout mode. In this mode all the SPAD-cells, configuration and TDC data are read out through the 15-bit output bus. The mode-0 readout operation takes roughly about $2ms$ for reading 1 frame. Each frame consists of a header followed by the chip configuration data, 433 (1 Dummy + 432 TDCs) TDC data and finally 468×144 SPAD-cell matrix. The read out is performed using a high-speed USB2.0 link. The achieved bandwidth for mode-0 with single chip operation is approximately 54Mbps.

The chip configuration takes up 6 bytes and report the operation mode, programmed threshold for *Enecal* and TDCs, software controlled bias for VCO and TDC, the *smart reset* status and its programmed interval. After the configuration, TDCs are readout. Each TDC takes up 4 bytes of data which includes 12bit coarse counter, 8bit phase information from two phase detectors for fine counting and a 1bit *Edge* signal. In total 433 TDCs are read out (432 TDCs + 1 Dummy) making up a total of 1732 bytes for TDC data. Finally, the SPAD-cell matrix is readout. There are 67392 SPAD-cells in the MD-SiPM array chip and each SPAD-cell occupying 1 bit. Thus, a total of 8424 bytes are taken up by SPAD-cell data. Thus, each frame is 10192 bytes wide.

2.4.2 Mode 2

Mode-2 is a fast readout mechanism. Unlike Mode-0, instead of individual SPAD-cell, the enecal module is read out along with all the TDCs and chip configuration. The frame size in mode-2 is significantly smaller than mode-0. Each frames starts with a header followed by *Enemonitor* register, the energy registers, chip configuration and finally all the 433 TDCs. The read out is performed with the same USB2.0 link and the bandwidth obtained is approximately 164Mbps.

The maximum frame size in mode-2 is 2068 bytes. The *enemonitor*, which takes up 2 bytes, is a 9 bit flag register for 9 columns of the MD-SiPM array chip. Each bit corresponds to each column and report a logic '1' when the number of fired TDCs is higher than the programmed threshold and a logic '0' otherwise. After the *enemonitor*, the energy registers are read out. Each MD-SiPM reports the sum of fired SPAD-cell via energy register. As it can count up to a maximum of 416, the energy register acquires 2 bytes. A total of 324 bytes of energy data is read out. After the energy data, the chip configuration and TDC data are read out. The structure of configuration and TDC data is same as mode-0.

3 Firmware Development

The 9 × 18 MD-SiPM array chip is interfaced with an FPGA for chip configuration and read out process. The chosen FPGA is a powerful Xilinx Spartan-6 series [29]. XC6SLX150 spartan-6 FPGA is utilized for configuring and readout process. Table. 3.1 lists some of the device features.

The main contribution of this chapter is to present the complete firmware that has been developed. The first step is to perform a complete porting and verification of mode-0 from Xilinx Virtex-5 evaluation board to Spartan-6 FPGA board. The second step is complete development of a new mode of operation called as mode-2. The new mode is designed as an event-driven based readout mechanism. Mode-2 gives us the ability to read out the energy registers of the complete cluster matrix. Mode-2 has a much lower dead time than mode-0 and, hence, allows us to detect more gamma events. Also, the ability to readout energy registers for each cluster enables us to explore designs with different scintillator pitch. Next, the thermal characterization is performed with a single chip. Lastly, the complete firmware is ported for multiple chip readout.

Logic Cells	147,443
Slices[1]	23,038
DSP blocks[2]	180
Total I/O banks	4
Usable GPIO pins	576
Flip-flops	184,304
Total block RAM bits (Kb)	4,824
Max. distributed RAM bits (Kb)	1,355
Clock Management Units[3]	6

Table 3.1: Spartan-6 XC6SLX150 specifications.

3.1 Mode 0 porting to Spartan-6

The chip was originally interfaced with a Xilinx Virtex-5 evaluation kit "ML507".The setup was used for basic test and characterization. For this purpose, a firmware was developed over ML507 that was responsible for configuration and performing a complete chip read out i.e., Mode-0. The read out was performed using ethernet link and the data rate was very slow because of the firmware implementation. Also, the Xilinx

[1]Each slice contains 4 LUTs and 8 flip-flops.
[2]Each DSP48A1 block has 18 × 18 multiplier, an adder and an accumulator.
[3]Each Clock Management Unit has 2 DCMs and 1 PLL.

ML507 evaluation kit was too big to be used for a compact small-animal PET scan detector. Thus for these reasons, a compact FPGA board is chosen with a cost effective FPGA i.e., Spartan6. One of the challenges faced when porting to spartan-6 series is to develop a new data acquisition link between the FPGA and PC. A high speed USB2.0 link is chosen as it provides a very high bandwidth and driver development on PC side is documented. A high speed FT2232H USB board is utilized provided by "HumanData". The USB controller is programmed to single USB to dual channel FIFO configuration providing a maximum theoretical data throughput rate of 480Mbps (practically 320Mbps).

As discussed above, mode-0 is a complete chip readout where configuration, TDCs and SPAD-cell data are read out and the read out time is in the order of $2ms$. The masking and chip configuration part is common in both the modes of operation. The configuration data and masking pattern are only sent once before the start of acquisition process and is kept constant throughout the measurement. Thus, a UART transmission link is used. The detailed configuration data sent to the chip for its proper operation is listed in the Table. 3.2 and the timing diagram for configuration phase and masking is shown in the Fig. 3.1.

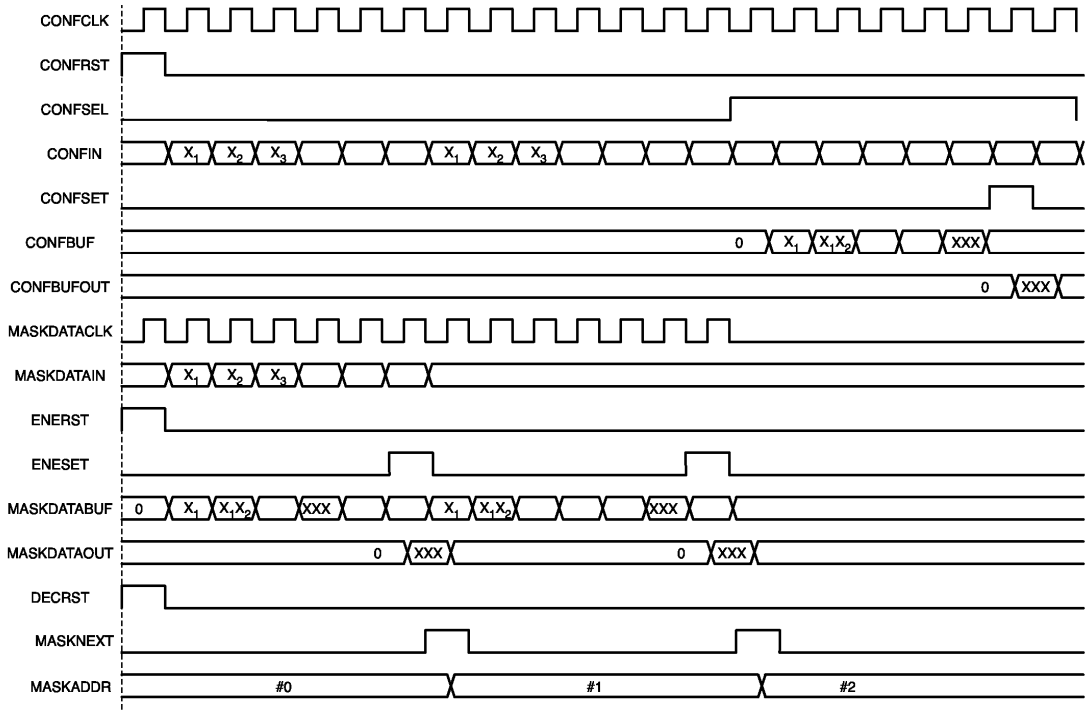

Figure 3.1: Timing diagram for configuration phase.

CONFIGURATION DATA	**No. of bits**	Remarks
WINDOW TIME	12	The SPAD-cells are kept activated for the specified time period.
MODE	2	Mode of operation 00 = mode-0 10 = mode-2
ROWCALSEL_ACT	1	0 = all rows active 1 = only one row is active
PREAMP	2	00 = Amplifier 01 = Comparator 10 = Inverter
TDCINSEL	4	0000 = leftmost cluster 1000 = rightmost cluster
ENE_{TH}	9	Energy threshold for mode-2 readout.
ENETEST	1	0 = use on-chip energy counter 1 = on-chip energy counter deactivated
SRON	1	To enable or disable the smart reset.
SRINTERVAL	10	To specify smart reset interval.
TDC_{TH}	6	To set TDC threshold for smart reset.
SWBIASTDC	4	0000 = fast 1111 = slow
SWBIASVCO	4	0000 = fast 1111 = slow
DISEXTON	1	To enable electrical trigger.
DISEXTPERIOD	8	To specify electrical trigger period.

Table 3.2: Configuration data for chip.

The complete SPAD-cell data is read out and to ensure correct masking, the SPAD-cells are plotted into an image using Matlab. Fig. 3.2(a) and (b) shows two images for SPAD-cell map. While in Fig. 3.2(a) first 4 columns are activated, while Fig. 3.2(b) shows 4 complete and 1 half columns are activated.

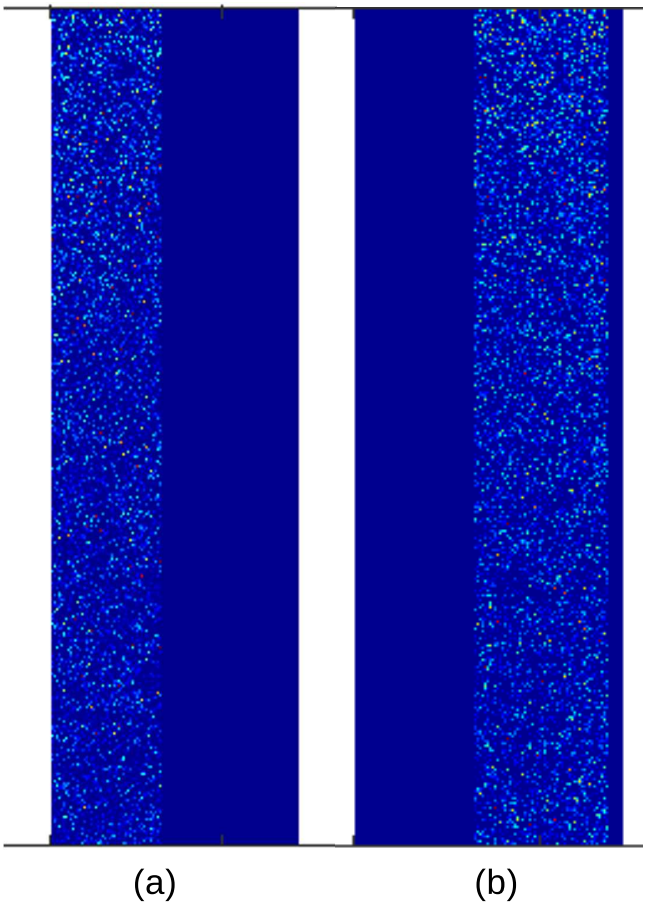

Figure 3.2: (a). SPAD-cell map for first 4 columns activated. (b). SPAD-cell map for next 4.5 columns activated.

In mode-0, the frame starts with a global reset and activation of VCOEN time that is same as "Window Time" in the configuration. During the VCOEN time, all the SPAD-cells that are not masked are activated and ready for photon detection. At the end of the VCOEN time, the read out phase starts. Thus, during the read out phase, the SPAD-cell are deactivated and cannot be used for photon detection. The read out timing diagram is given by Fig. 3.3. The ENETEST bit is set to '1' for mode-0 operation which results in the deactivation of on-chip energy counter and energy calculator module only relays the individual SPAD-cell firing when a read command is issued. The ENECLK is provided to start the readout process. At the beginning, a ROWNEXT pulse is provided along with DECCLK so that the row address is set to '0' pointing to the first row. Now, at every rising edge of ENECLK, ENESET is probed. If ENESET is #0 then energy counter is read out otherwise configuration is read out. In each energy counter readout, 2 15-bit words are read back to back. The

least significant 8 bits of each word has SPAD-cell data. Thus, in total 16 SPAD-cells are read from reading energy calculator module assigned for first column. Similarly, the ENECLK is provided to read out all the 9 energy calculator modules at the end of which 144 SPAD-cells are read out i.e., one complete SPAD-cell row. Now, ROWNEXT pulse along with DECCLK is provided again to increment the row address from #0 to #1 and the process of reading out 9 energy calculator modules is repeated resulting in reading out the SPAD-cell information for the next row. The complete process is repeated for 468 rows at the end of which ENESET is set to logic '1' for reading out the configuration.

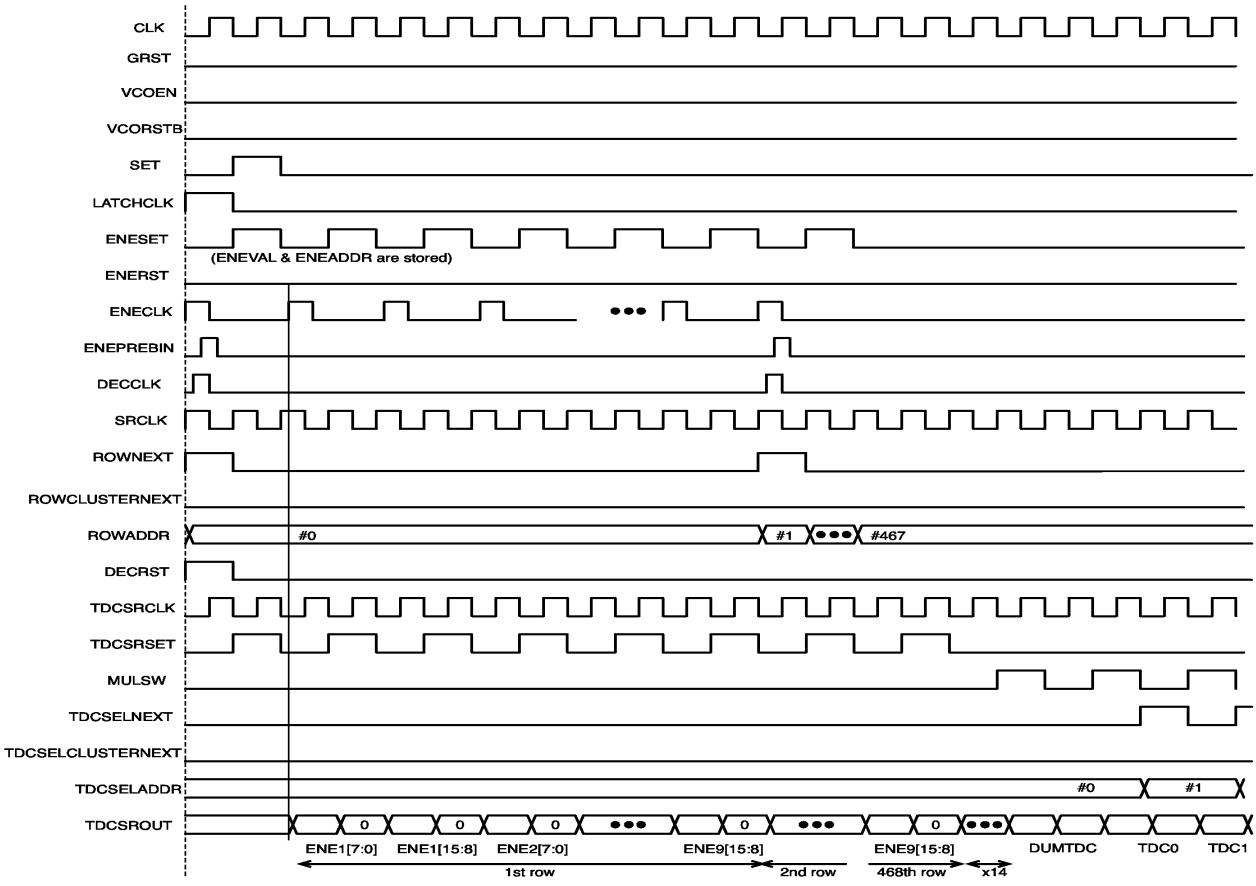

Figure 3.3: Timing diagram for mode-0 read out.

After successful SPAD-cell information read out, TDC data is read out. For TDCs, the signals of interest are MULSW, TDCSELNEXT and TDCSRCLK. The TDCSELNEXT signal is used to increment the TDC select address. The TDC read out on chip is implemented in such a way that the first TDC to be read is dummy and then TDCSELNEXT is probed to read the TDC corresponding to the address set on TDCSELADDR. The start of TDC readout cycle is initiated by asserting MULSW. The first MUSLW pulse detected by TDCSRCLK triggers the dummy TDC readout process, from the second MULSW pulse, the TDCSELNEXT signal is probed. MULSW and TDCSELNEXT are phase shifted by 180° and have twice the TDCSRCLK period. The TDCSELNEXT signal is delayed by one whole clock cycle to enable dummy TDC

readout. From there on, TDCSELNEXT is toggled to increment the TDC address. Thus, TDCSELNEXT is provided 432 times to increment TDC address from #0 to #431 while MULSW is provided 433 times (1 for dummy and next 432 pulses for each TDC). Within one MULSW cycle, two 15-bit words are read out which contains the TDC data. Fig. 3.4. shows the TDC data structure in the read out process. In the TDC data, we read a 12-bit coarse counter, 2 8-bit phase information coming from two identical phase detectors implemented in each TDC and the $EDGE$ signal.

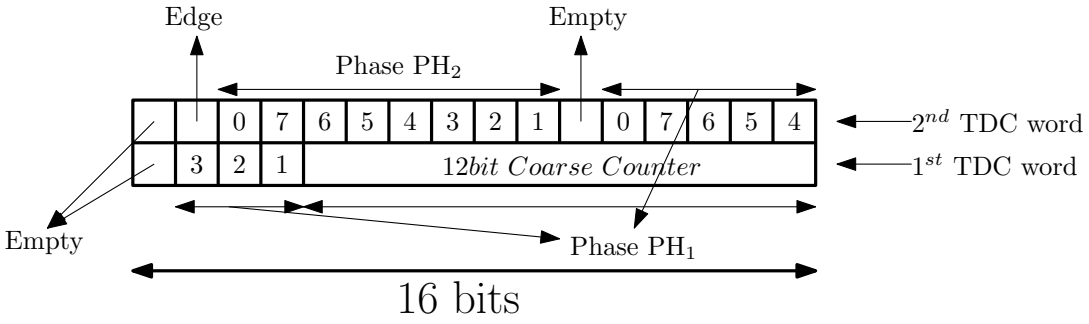

Figure 3.4: TDC data structure in read out process.

3.2 Mode 2 Designing

Mode-2 is a fast readout process and unlike mode-0, which is a frame-based readout mechanism, mode-2 is an event-driven readout technique. In mode-2, the on-chip energy counter is activated and only the energy value is read out instead of complete SPAD-cell array. The configuration and TDC readout mechanism is identical to mode-0. In the current implementation, mode-2 read out process takes approximately $100\mu s$. Thus, the SPAD-cells are deactivated only for $100\mu s$ leading to a lower system dead time compared to mode-0. In mode-2, to avoid TDC and energy count saturation due to DCR the smart reset is activated and triggered, typically, every $200ns$ however it can be programmed to any other value as well.

The following steps illustrates the mode-2 operation.

1. The frame in mode-2 starts with a global reset followed by activating VCOEN. The VCOEN can be kept activated upto a maximum of $6.4\mu s$. This maximum VCOEN time corresponds to the full count of 17-bit TDC with a LSB of $49ps$.

2. During the VCOEN active period, smart reset clears out the saturation effect from TDCs and SPAD-cell columns. Mode-2 functions only when smart reset is activated in the configuration phase.

3. The 9×18 MD-SiPM array chip has a 9 bit register called *Enemonitor*. It is a flag register with each bit corresponding to one cluster column. The bit is set to '1' if the number of TDCs fired for a particular cluster column exceeds the TDC threshold TDC_{th}.

4. The TDC_{th} is programmable and is set to a value which is higher than the number of TDCs fired by DCR. Thus, the DCR will never set the enemonitor flag and report a false event.

5. From the start of VCOEN period, Enemonitor register is probed regularly to check if there is an event. In case an event is registered and the enemonitor bit for a given cluster column is set to '1', the firmware issues SETBIN, STOPDUM and LATCHCLK to freeze the chip (both energy counters and TDCs) and simultaneously deactivating VCOEN.

6. Once the chip is frozen i.e., its energy counter values and TDC values are latched, a complete chip readout is performed. SETBIN signal is responsible for latching the SPAD-cell value to a 1-bit SPAD-cell memory and STOPDUM is responsible for latching the dummy TDC.

7. The readout is performed in the following order:

   (a) First, the enemonitor register is read.

   (b) Second, the 9-bit energy counter is read in a 2 byte USB word. Each row has 9 clusters and thus a total of 18 bytes are read for the first cluster row.

   (c) The above process is repeated for 18 rows to read out the energy counters for the complete chip. A total of 162 energy counter registers each having 2 byte long USB word. Hence, a total of 324 bytes of data for energy counters.

   (d) Following the energy readout, the configuration data is read. The configuration is read for verification purposes and can be omitted.

   (e) Lastly, the TDCs are read out. The trick here is to read the dummy TDC and then only those TDCs that fired due to a valid event. As discussed earlier, each enemonitor bit represents one cluster column. Each cluster column shares 48 TDCs. Thus, for every enemonitor bit set to '1', 48 TDCs are read.

   (f) Each TDC acquire 4bytes of data and, therefore, a maximum of 1732 bytes can be read out for 433 TDCs.

Fig. 3.5 shows the timing diagram for mode-2 readout mechanism and Table. 3.3 lists the important signals are used for energy counter readout for the complete chip. The total energy counter modules read are 162(9×18 MD-SiPM). The counters are read through 2 15-bit words via the output bus. The flowchart in Fig. 3.6 describes the energy readout process. Once the energy module readout is finished, the configuration and TDC data read out begins. The readout algorithm for configuration and TDC is same as mode-0. Thus, the maximum data that is read out in mode-2 can be only be 2068 bytes (324 bytes of energy data + 1732 bytes of TDC data + 6 bytes of configuration + headers). As the amount of data readout in mode-2 is extremely smaller than mode-0, the readout time is approximately 20 times faster. Also, since mode-2 is event driven, the read out is initiated only when there is valid gamma event thereby reducing the system dead time.

Signals	Description
ENECLK	clock input to the energy calculator module.
ROWNEXT	1-bit signal that is used to increment the row address of the SPAD-cell matrix.
ROWADDR	It is a 9-bit register inside the chip that keeps the track of the SPAD-cell row. Initialized to point the 1^{st} SPAD-cell row and increments by 1 every clock cycle (if the ROWNEXT is activated) up till 467 and then resets back to 0.
ROWCLUSTERNEXT	It is a 1-bit signal that is registered inside the chip with every ENECLK. It is used to make the ROWADDR jump to point the 1^{st} SPAD-cell row of a particular cluster row. The cluster row is decided by how many clock cycles the ROWCLUSTERNEXT is kept activated. Also, it is used to latch the energy counter values onto the output bus.
ENERST	It is a reset signal that resets the following: 1.) The energy counters back to 0 2.)ROWADDR to $9'b0$ so that is points to the 1^{st} SPAD-cell row of the 1^{st} cluster row.

Table 3.3: Signal description for mode-2 energy counter readout.

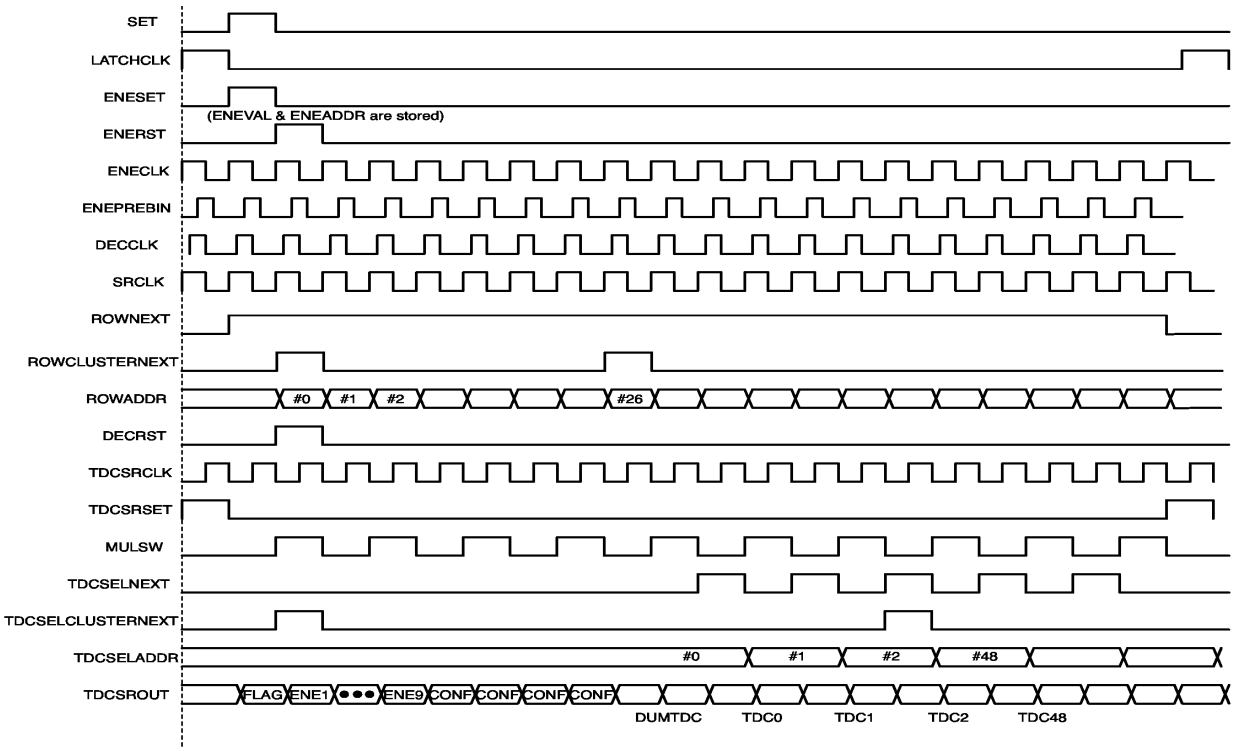

Figure 3.5: Timing diagram for mode-2 read out.

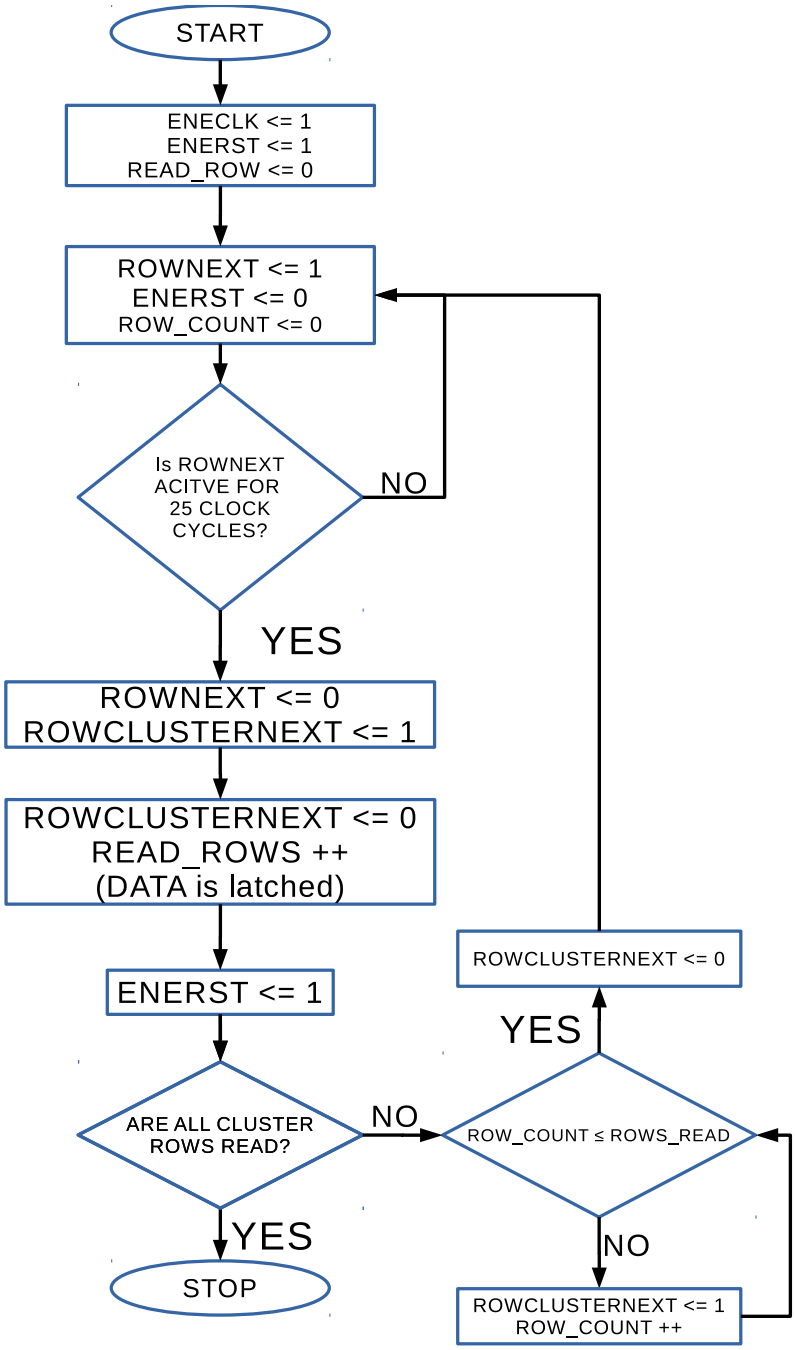

Figure 3.6: Energy counter readout algorithm.

3.3 SPAD-cell Array and Energy Count Verification

SPAD-cell array and energy count obtained in mode-0 and mode-2 respectively needs to be verified. The process of SPAD-cell array verification is straight forward, where the chip is configured with a specific masking profile and VCOEN time. Depending upon

the masking profile, SPAD activity is observed on SPAD-cells which are unmasked. By varying the VCOEN time, different DCR can be observed. With increase in VCOEN time, a higher DCR is recorded as SPADs are activated for a longer period and more SPAD-cells are fired by photons.

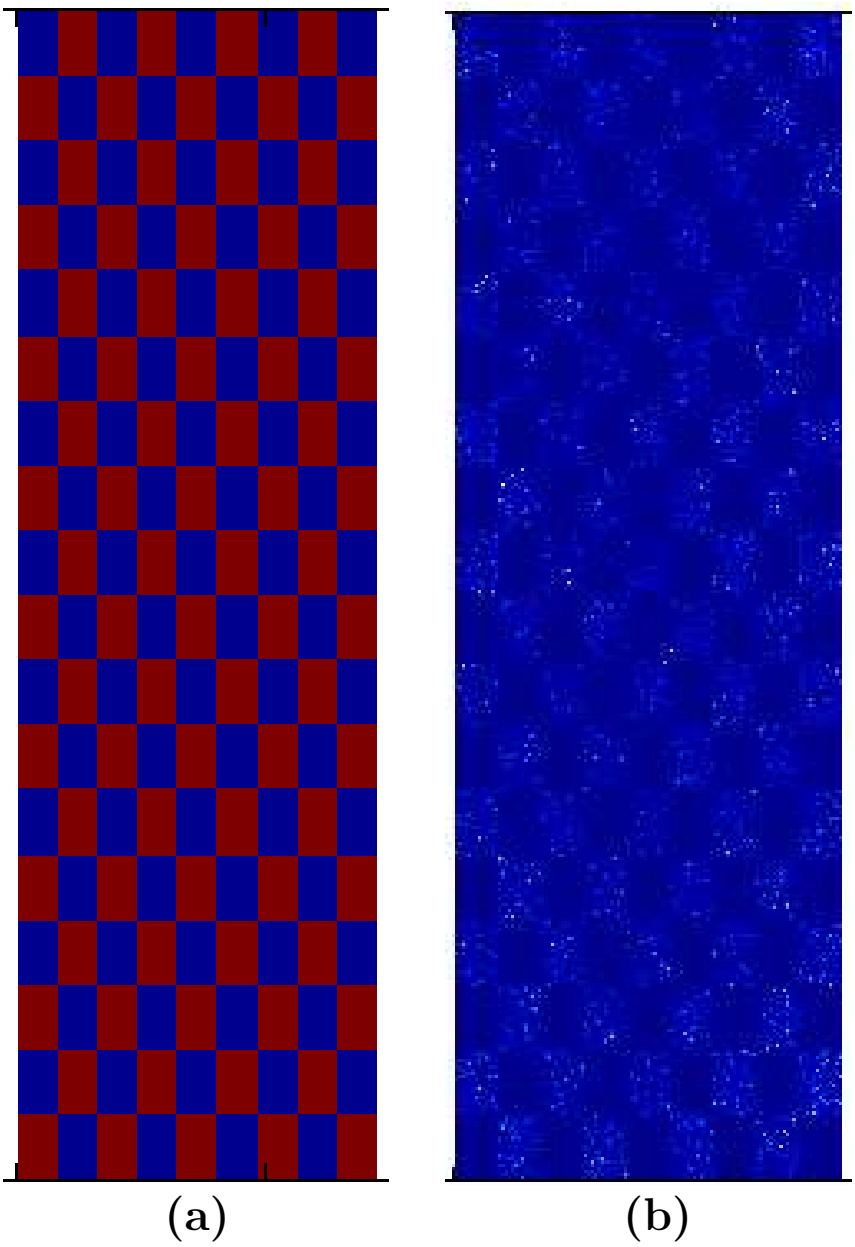

Figure 3.7: (a) Masking profile programmed in the chip. (b) SPAD-cell array plot.

Fig. 3.7(a) shows the masking profile where every alternate MD-SiPM cluster is activated per cluster row. The masking is a 468×144 matrix containing the binary information for each SPAD-cell. The masking profile is plotted with blue indicating an activated MD-SiPM cluster while red denoting a deactivated cluster.

In mode-2, the energy counter verification for MD-SiPM clusters is done by plotting the counts received from the energy calculator module. Fig. 3.8 shows the plot of energy counts obtained for 108 activated MD-SiPM clusters. The energy counts are plotted for several frames that have been acquired. The X-axis denotes the counts, while Y-axis signifies the number of frames with a particular count. The plot takes up a gaussian curve as the counts are generated by DCR and is centered around the mean DCR of the cluster.

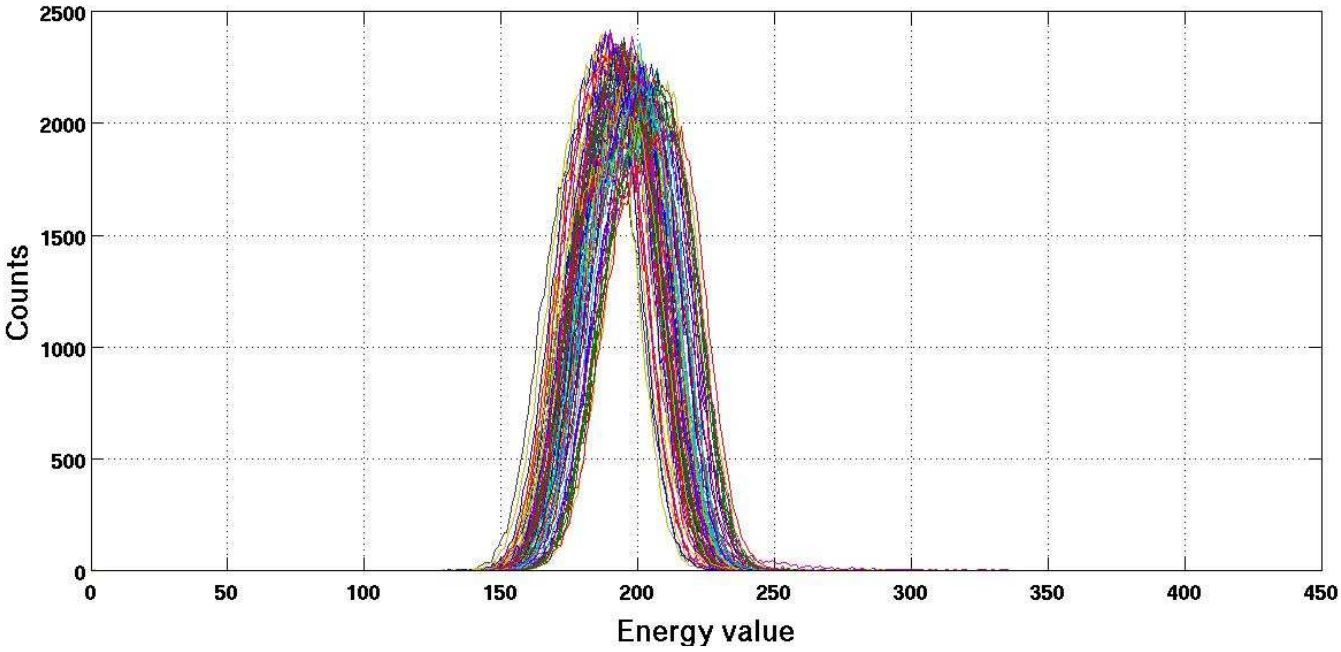

Figure 3.8: Mode-2 energy count plots

For mode-2 operation, as the VCOEN time is activated for $6.4\mu s$, smart reset is activated to avoid energy count from saturating. As the smart reset interval is changed, the curve shifts along the x-axis as counters are active for different time intervals and hence can have either higher or lower mean count depending upon the reset interval.

3.4 TDC and Dummy Verification

In either modes, the TDC and dummy data needs thorough verification and the process is same since the data is identical in either modes and also the read out methodology is same. The process of TDC verification is not as straight forward as SPAD-cell data verification. For this purpose, an electrical trigger is employed to trigger the TDCs at a specific time within the VCOEN time. The time interval is programmable and care must be taken to ensure that the electrical trigger interval is smaller than the VCOEN time otherwise, the electrical trigger will happen after the VCOEN is deactivated and hence will not be captured by the TDCs.

To operate electrical trigger correctly, the complete SPAD-cell matrix is either

masked or the VOP is switched off so that none of the SPADs are able to pull down the timing line that is connected to the TDCs in the TDC bank. The electrical trigger input is connected to the timing line of all the 432 TDCs and is controlled by a counter running inside the FPGA control unit. The electrical trigger, $DISEXTBIN$, is a falling-edge sensitive signal. If asserted to '0', the timing lines of all the TDCs are pulled down resulting in firing of all the 432 TDCs. The TDCs will start counting until the end of the frame.

There are two signals which are programmed into the FPGA that controls the $DISEXTBIN$. They are $DISEXTON$ and $DISEXTPERIOD$. DISEXTPERIOD is defined as the number of clock cycles from the start of VCOEN after which the electrical trigger must fire. The DISEXTON activates the counter inside the FPGA and starting moment of the counter is synchronized with VCOEN activation. The counter runs on the system clock frequency of $20MHz$ and when the count reaches DISEXTPERIOD, $DISEXTBIN$ (signal going to the MD-SiPM chip) is pulled down.

Fig. 3.9(a) and (b) shows the electrical trigger DISEXTBIN and VCOEN relation for two trigger time intervals of $250ns$ and $450ns$ respectively.

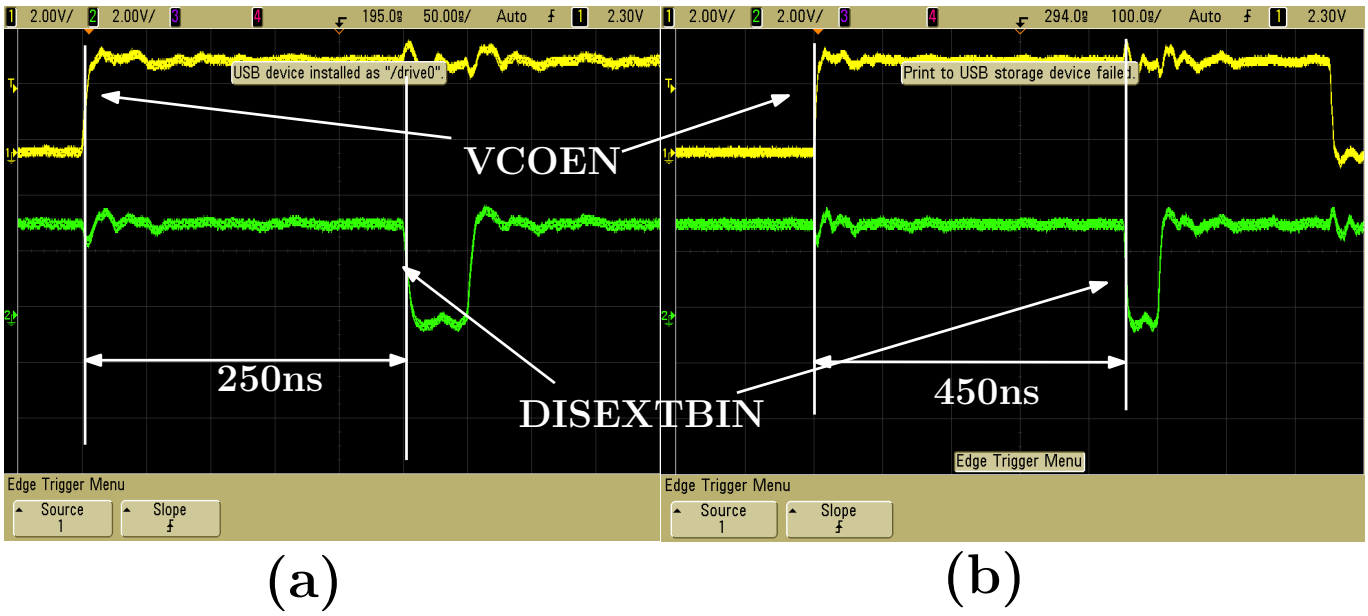

Figure 3.9: DISEXTBIN vs VCOEN signal relation. (a) Electrical trigger set at $250ns$. (b) Electrical trigger set at $450ns$.

Fig. 3.10(a), (b) and (c) shows the results for the electrical trigger verification of the TDCs.

1. Fig. 3.10(a) is executed with VCOEN time of $500ns$ and the electrical trigger is set at $50ns$ from the start of VCOEN time.

2. Fig. 3.10(b) is performed with VCOEN time of $750ns$ and the trigger is set at $250ns$.

3. Finally, Fig. 3.10(c) shows the electrical trigger test with VCOEN time of $750ns$ and trigger time is $450ns$.

The dummy TDC runs throughout the VCOEN time and, hence, reports the VCOEN time itself.

3.5 Temperature Sensing and Controlling for single chip operation

The MD-SiPM array chip generates approximately $1.5W$ and needs to be dissipated actively. Passive heat dissipation is not feasible and the chip can reach as high as $110°C$. The temperature and current consumption follows a positive feedback. As the temperature starts to rise, the DCR increases due to more SPAD-cells being triggered. As more SPAD-cells start to fire, the current consumption on the main supply voltage increases which leads to an increase in temperature. Although, the bandgap reference circuit is designed to be temperature independent but practically it is prone to minor variations due to temperature which may be amplified if the temperature goes above a certain point. Also, continued operation under such high temperature can cause irreversible thermal damage.

In order to monitor the temperature of 9×18 MD-SiPM array chip, the PCB board that holds the chip also has two low-power digital temperature sensors designed and manufactured by *Texas Instruments*. The *TMP104* is a digital temperature sensor designed in a 4 ball wafer chip-scale package (WSCP) with a resolution of $1°C$ [30]. TMP104 is designed with a SMAART wire interface which is similar to a UART interface. The sensor has only two I/O pins, namely, RX and TX. These temperature sensors can be connected in a daisy chain format with a maximum of 16 devices connected in the chain. TMP104 has a 8bit temperature register that can measure from $-10°C$ to $100°C$ with an accuracy of $\pm 0.5°C$ [30]. The two sensors which are installed on PCB to monitor the MD-SiPM chip's temperature are connected in a daisy chain fashion.

A simple heat sink cannot dissipate the entire heat generated by the chip as passive cooling options are not adequate. Thus, a water cooling system is employed. In water cooling system, the chip is housed in a metal chamber which has two ports, one for water inlet and the other for outlet. Cold water is circulated through the system and it is capable of dissipating the heat quite effectively. However, special care has to be taken to ensure the water that is fed into the system is not very cold. If the water temperature is lower than the dew point then it can cause condensation which can damage the chip.

Fig. 3.11 shows the water cooled heatsink that fits between the PCB holding the MD-SiPM array chip and the motherboard. Water is fed into the heatsink through the inlet marked A and it comes out from the outlet marked B. The heatsink is manufactured with a medium strength Aluminium alloy.

Table. 3.4 shows the temperature variations with and without the use of water cooled heatsink for a single chip operation with 3.3V VDDA supply. The water circulated through the system is at normal room temperature. The cooling can further be

	WITHOUT HEAT SINK	WITH HEATSINK	
		WITHOUT WATER FLOW	WITH WATER FLOW
VDDA	3.3V	3.3V	3.3V
IDDA	334mA	265mA	240mA
POWER	1.1W	0.87W	0.79W
T_{BOTTOM}	70°C	56°C	41°C
T_{TOP}	74°C	59°C	43°C

Table 3.4: Temperature of a single MD-SiPM operation with and without water cooled heatsink.

optimized by circulating cold water through a closed loop with a refrigeration unit in place.

3.6 Expansion to Multiple SiPMs Read-out

The firmware discussed up till now can perform mode-0 and mode-2 readout for a single MD-SiPM array chip. In a PET scan system, there is a ring of detectors and the readout process has to be done for multiple chips. The PET scan design under consideration has 8 MD-SiPM chips per detector module that is read through a single FPGA. Thus, the firmware designed has to be ported for multiple chip readout. The motherboard is designed to integrate 8 MD-SiPM array chips in a 4×2 matrix formation.

Fig. 3.12 shows the 4×2 motherboard 3D-model. Fig. 3.12(b) shows the top layer with connectors to mount 8 MD-SiPM array chips and Fig. 3.12(b) shows the bottom layer where the FPGA is connected. Most of the control signals are shared among the 8 MD-SiPMs with some exceptions. Signals that are directly responsible for masking and readout process are routed individually to each MD-SiPM. ENECLK, DECCLK, TDCSRCLK, ENEPREBIN, MASKNEXT and 15-bit output bus are routed individually to each chip. While a USB2.0 link was sufficiently fast for a single chip operation, to operate 8 chips simultaneously higher bandwidth is required and hence a USB3.0 link is proposed. USB3.0 provides a $5Gpbs$ maximum data transfer rate which is 10 times faster than a USB2.0 link. All the chips are read simultaneously via 15-bit output bus coming from each MD-SiPM chip. The received data is then interleaved and relayed to the USB FIFO. The data readout from the USB is then de-interleaved via post-processing scripts to extract SPAD-cell, configuration and TDC data for each chip. The core of readout mechanism for both modes remains same while only the data routing through USB FIFO buffer is adapted for data transfer.

Similar to a single chip operation, the multiple chip readout also requires active temperature sensing and controlling. Fig. 3.13(a) shows the 3D rendering of the water cooling assembly mounted over the 4×2 Motherboard for cooling down 8 chips when

they are operating simultaneously and Fig. 3.13(b) shows the actual experiment setup. In the experimentation setup, 2 MD-SiPM array chips are operated simultaneously while the other 6 MD-SiPM locations are mounted with dummy chips, which are not bonded. The dummy are mounted to close the temperature sensor chain and thus enables us to read the 16 temperature sensors on board the motherboard (2 temperature sensor per MD-SiPM array chip)

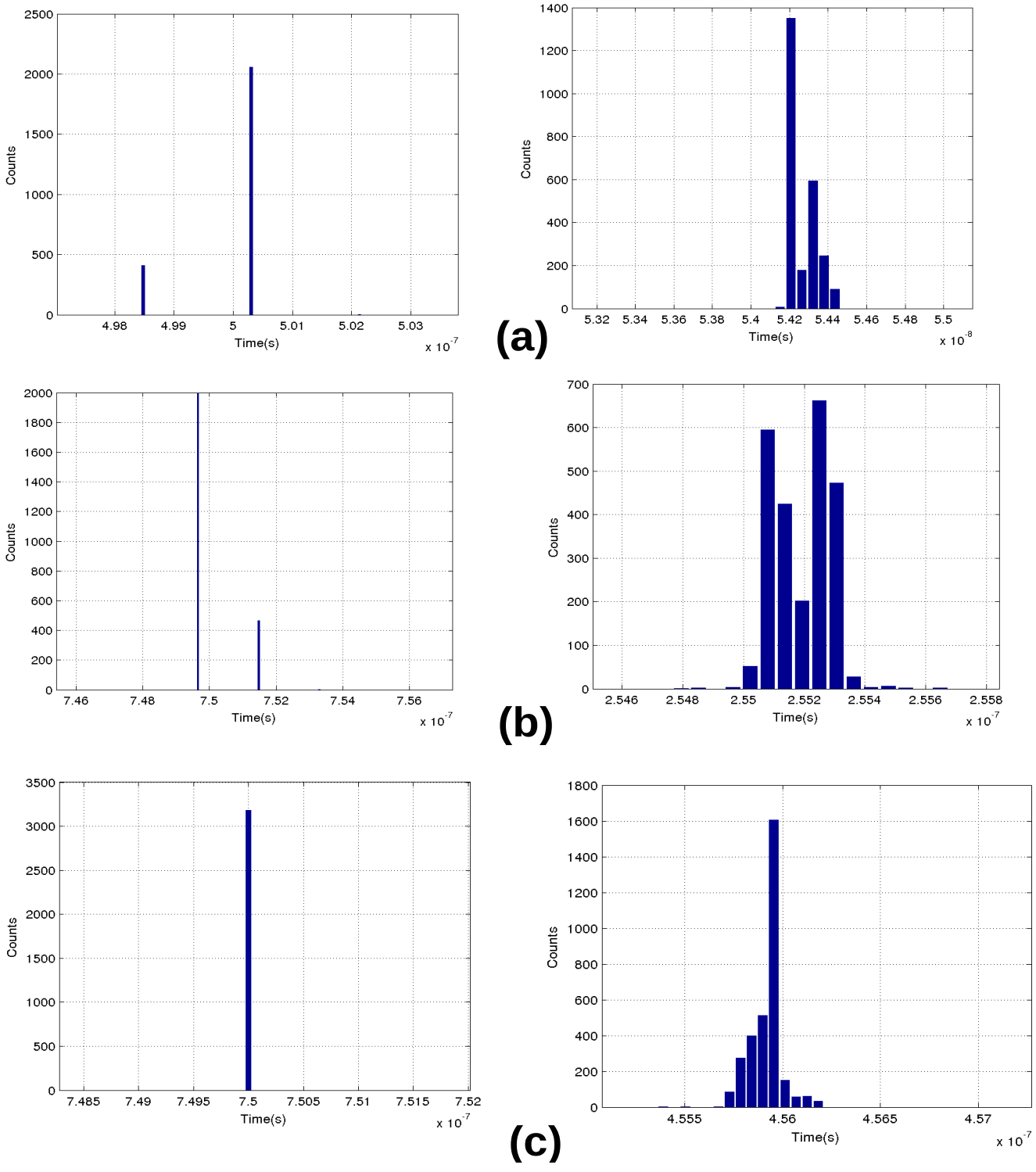

Figure 3.10: (a) Dummy TDC at $500ns$ and electrical trigger at $50ns$. (b) Dummy TDC at $750ns$ and electrical trigger at $250ns$. (c) Dummy TDC at $750ns$ and electrical trigger at $450ns$.

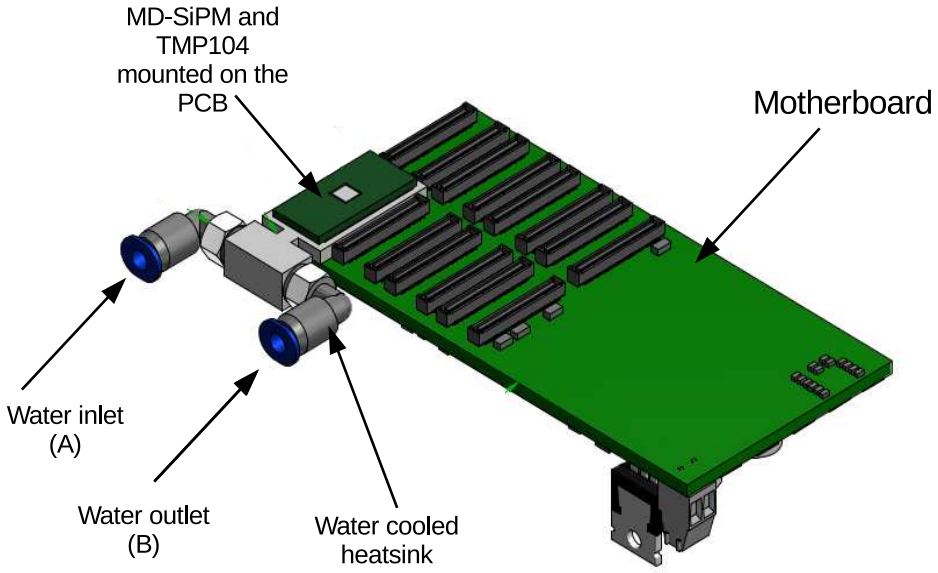

Figure 3.11: Water cooled heatsink for 1 MD-SiPM chip.

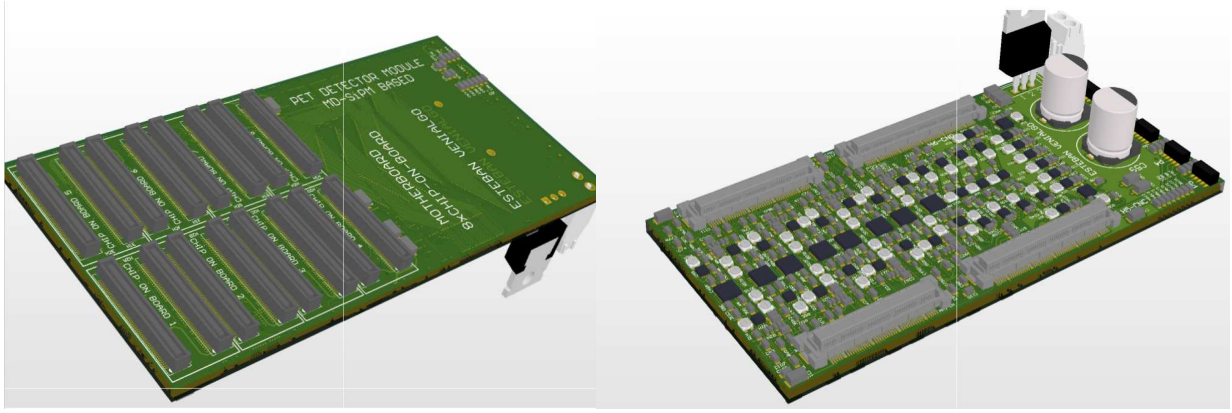

Figure 3.12: 4×2 motherboard model housing 8 MD-SiPM array chips. (3D rendering using Altium PCB designer). (a) Top layer with connectors for 8 MD-SiPM chip. (b) Bottom layer with connectors for Spartan-6 FPGA board.

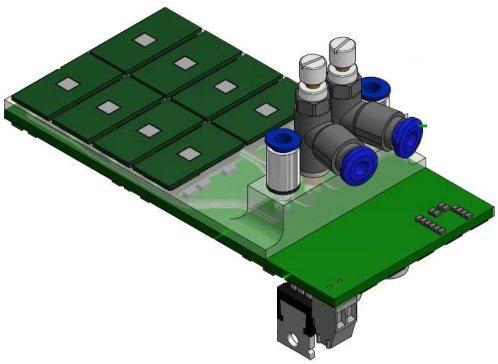

(a)

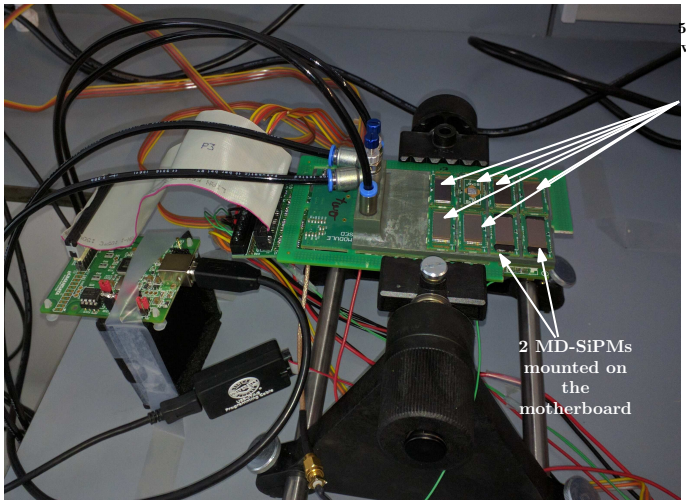

(b)

Figure 3.13: (a) 3D model of the water cooling assembly mounted over the motherboard. (b) Actual image of water cooling assembly over motherboard with 2 MD-SiPM chips, 6 dummies (water is circulated through the inlet and outlet ports).

Radiation Characterization 4

The MD-SiPM based PET detector module is coupled with a scintillator for converting the gamma photon into visible light photons. The main contribution of this chapter is to characterize two scintillator choices. One with a $1.6mm$ pixel pitch and other with $0.8mm$ pixel pitch. Scintillation characterization includes energy measurements, crystal pixel identification and light crosstalk. Additionally, SPTR measurements for TDCs and impact of DCR on TDCs are also discussed. The choice of scintillator for our design is a Cerium-doped Lutetium Yttrium Orthosilicate (LYSO) scintillator. To ensure superior performance of the PET detector, LYSO scintillator is chosen over Bismuth Germinate (BGO) scintillators. LYSO offers much higher light yield and small decay time. Table. 4.1 lists some of the important properties along with comparison with BGO scintillator.

Properties	LYSO	BGO	$LaBr_3$(Ce)	LSO(Ce)
Density (g/cm^3)	7.2	7.13	5.08	7.4
Refractive Index	1.82	2.15	1.9	1.82
Decay Constant (ns)	42($\pm$5)	300	16	40
Light Yield (%) NaI-TI	75	25	165	~75
Energy Resolution (511keV, %)	10	16	-	~12
Rise Time(ps)	89	-	280	79

Table 4.1: Scintillator properties for LYSO and BGO scintillators [7, 8].

Each MD-SiPM array chip is coupled with a pixelated LYSO scintillator. For experimentation, two LYSO crystals are used each with a different crystal pixel pitch. One scintillator with $0.8mm$ pitch and the other with $1.6mm$. As discussed in chapter-3, each MD-SiPM unit is $800\mu m \times 780\mu m$. Thus, the scintillator pixel pitch is chosen in such a way that for $0.8mm$ pitch each scintillator pixel is aligned with 1 MD-SiPM whereas a $1.6mm$ pitch scintillator is aligned with 4 MD-SiPMs (in 2×2 fashion). The performance metrics are measured for both the scintillator choices to find out the optimal scintillator pitch.

4.1 Energy Measurements

The energy measurement is dependent on two aspects of the scintillator used:

1. How many visible light photons are generated for every gamma photon absorbed, a property known as light yield.

2. How well the scintillator can distinguish between photons with energy corresponding to annihilation process($511keV$) and otherwise.

In the energy measurements performed for small-animal PET scan detector, ^{22}Na is chosen as a radioactive source. The radioactive properties of ^{22}Na is listed in Table. 4.2.

Property	**Value**
Radioactivity	Gamma-1.27MeV (100% abundance) Annihilation Photons-511keV (180% abundance) Beta-546keV (90% abundance)
Half life ($T_{1/2}$)	2.6 Years
Specific Activity	$6,243Ci/gm$ or $2.31 \times 10^{14}Bq/gm$

Table 4.2: Radioactive properties of ^{22}Na.

4.1.1 Experimentation setup and Methodology.

There are two scintillator designs that are being evaluated. One scintillator with $0.8mm$ pitch and the other with $1.6mm$ pitch. Fig. 4.1(a) and (b) shows the diagram of the 0.8mm pitch scintillator and $1.6mm$ pitch scintillator respectively. Fig. 4.1(c) shows the actual scintillators glued over the MD-SiPM array chip. For the purpose of testing the two scintillators simultaneously, two test boards are utilized and both the chips are mounted over the board and kept in the dark chamber with ^{22}Na source. 2 powerful fans per chip are installed for cooling down the chip because water cooling is not possible with test boards. Fig. 4.2 shows the experimentation setup for energy measurements. With the $0.8mm$ pitch scintillator, the total number of SPAD-cells available for event detection is 416. The total number of available SPAD-cells in $1.6mm$ pitch scintillator is 1664.

4.1.2 Results

The gamma scintillations observed by two detector with different scintillator pixel pitch is presented here. In Fig. 4.3(a) through (d), 4 gamma scintillations for $1.6mm$ pixel pitch are displayed. In each map, one on the left is a binary image of single frame data for the chip and the other has been post processed. Similarly, Fig. 4.4(a) through (d) represents 4 gamma events being captured by detector with a $0.8mm$ pixel pitch. In post processing, dilation, erosion and averaging is performed. Dilation and erosion are two fundamental image processing techniques where a 3×3 structural element is used to smoothen the image and merge the foreground boundaries with background. Averaging is performed to reduce the noise in image. The basic assumption is that noise induced in the image are registered dark counts. Hence, the pixel level fluctuations can be smoothened by averaging over multiple frames.

Scintillator pixel identification during energy measurement is a crucial task. Hence, centroid calculations are performed over the number of frames that registered gamma

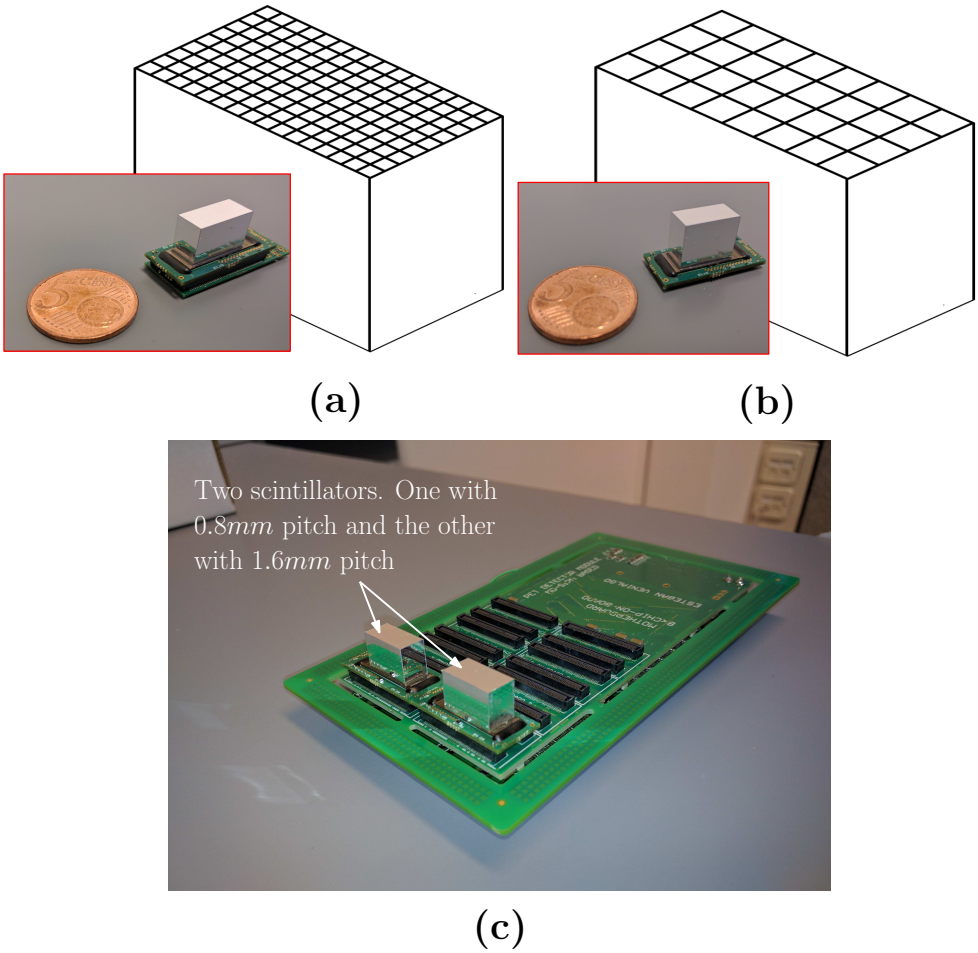

Figure 4.1: (a) $0.8mm$ pitch scintillator. (b) $1.6mm$ pitch scintillator. (c) Actual scintillators glued over the MD-SiPM array chip.

scintillations. *Centroids* are the pixels, within one crystal pixel, with highest activity during a gamma scintillation. A row-wise and column-wise centroid histogram is plotted. Fig. 4.5(a) and (b) shows the row-wise and column-wise centroid histograms respectively for scintillator with $0.8mm$ pixel pitch. The centroids are acquired with VOP $= 21.5V$ and a VCOEN time of $1\mu s$. Similarly, Fig. 4.6(a) and (b) shows the row-wise and column-wise centroid histograms respectively for the scintillator with bigger pixel pitch i.e., $1.6mm$. The VOP is set to $21.8V$ and VCOEN time is $1\mu s$. Finally in Fig. 4.7, the normalized 2D histogram is presented for scintillator with $0.8mm$ pixel pitch.

4.2 Dead Time

The dead time of the PET scan system has two components: the scintillator decay time t_d and the system level dead time. To minimize the first component, LYSO scintillator is chosen whose decay time is $42ns$. The system level dead time is due the readout

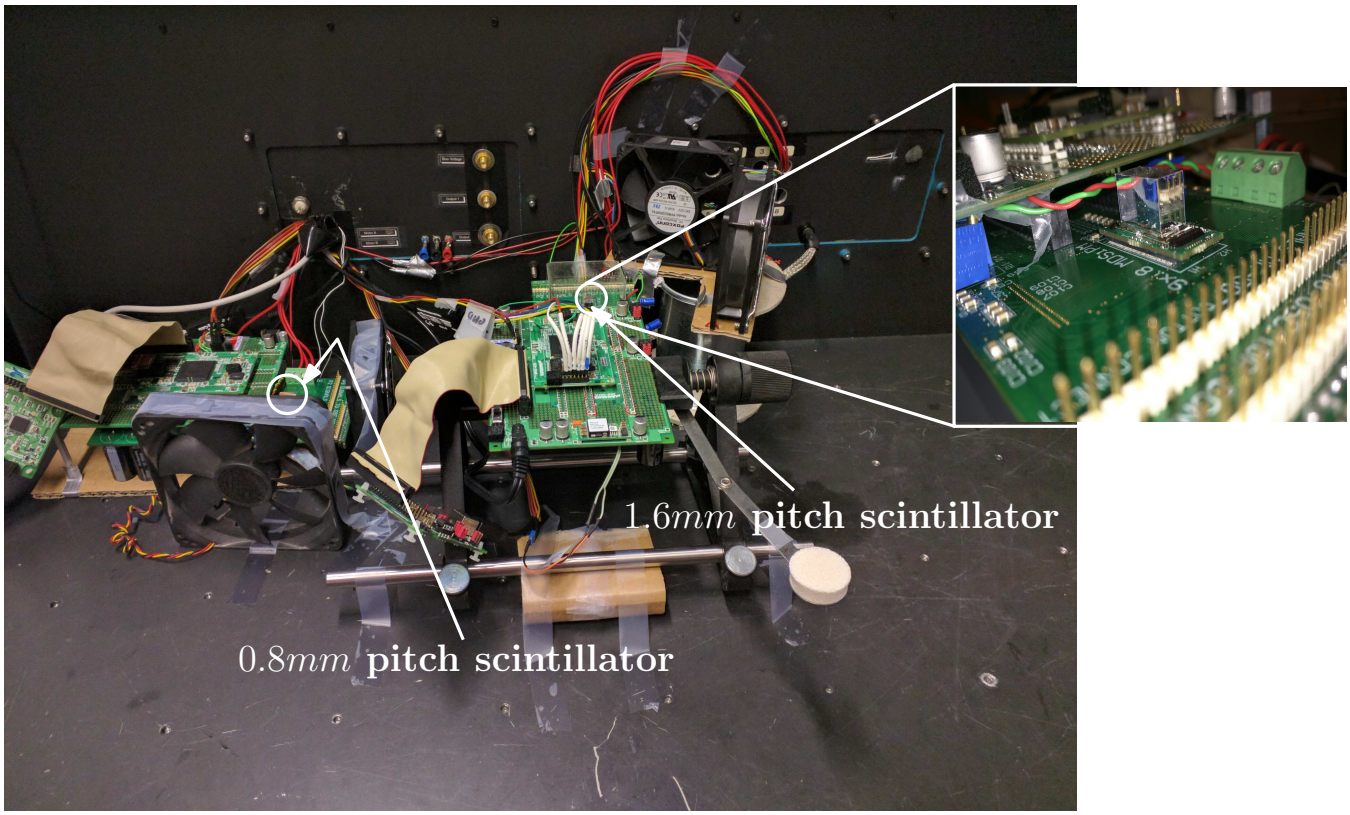

Figure 4.2: Two scintillators installed on test boards with fan based cooling.

time. During the readout time, the SPADs are unusable and hence no detection is possible. The measured system level dead time for mode-0 is $2ms$ while for mode-2 is $98.4\mu s$. Hence, from the measurements presented above, it is quite evident that system level dead time is more significant than the scintillator decay time.

For the measurement setup, the radioactive source under use is ^{22}Na and its properties are listed in Table .4.2. The source has been reported to have $200\mu Ci$ of activity in August 2010. Thus, the radioactivity as of now is measured using Eqn. 4.1.

$$N(t) = N_0.e^{-\lambda.t} = N_0.e^{-t/\tau} \tag{4.1}$$

where N_0 can be substituted with initial activity. The final activity for the source as of September 2016 comes to be $39.50\mu Ci$. The GATE simulation performed with a radioactive source of $39.5\mu Ci$ kept at a distance of $4cm$ away from the detector yields a count rate of 7545.2 counts per second. For mode-0, the system dead time is $2ms$. The windowtime is set at $1\mu s$. Thus, the total events that happened inside the active window time is given by Eqn. 4.2

$$\text{Counts within window time} = \frac{1\mu s}{2ms} \times 7545.2cps \;=\; 3.772cps \tag{4.2}$$

For the measurement, a total of $250GB$ of data has been read and processed in 50MB block size. The number of gamma scintillations is shown in the Fig. 4.8. The average

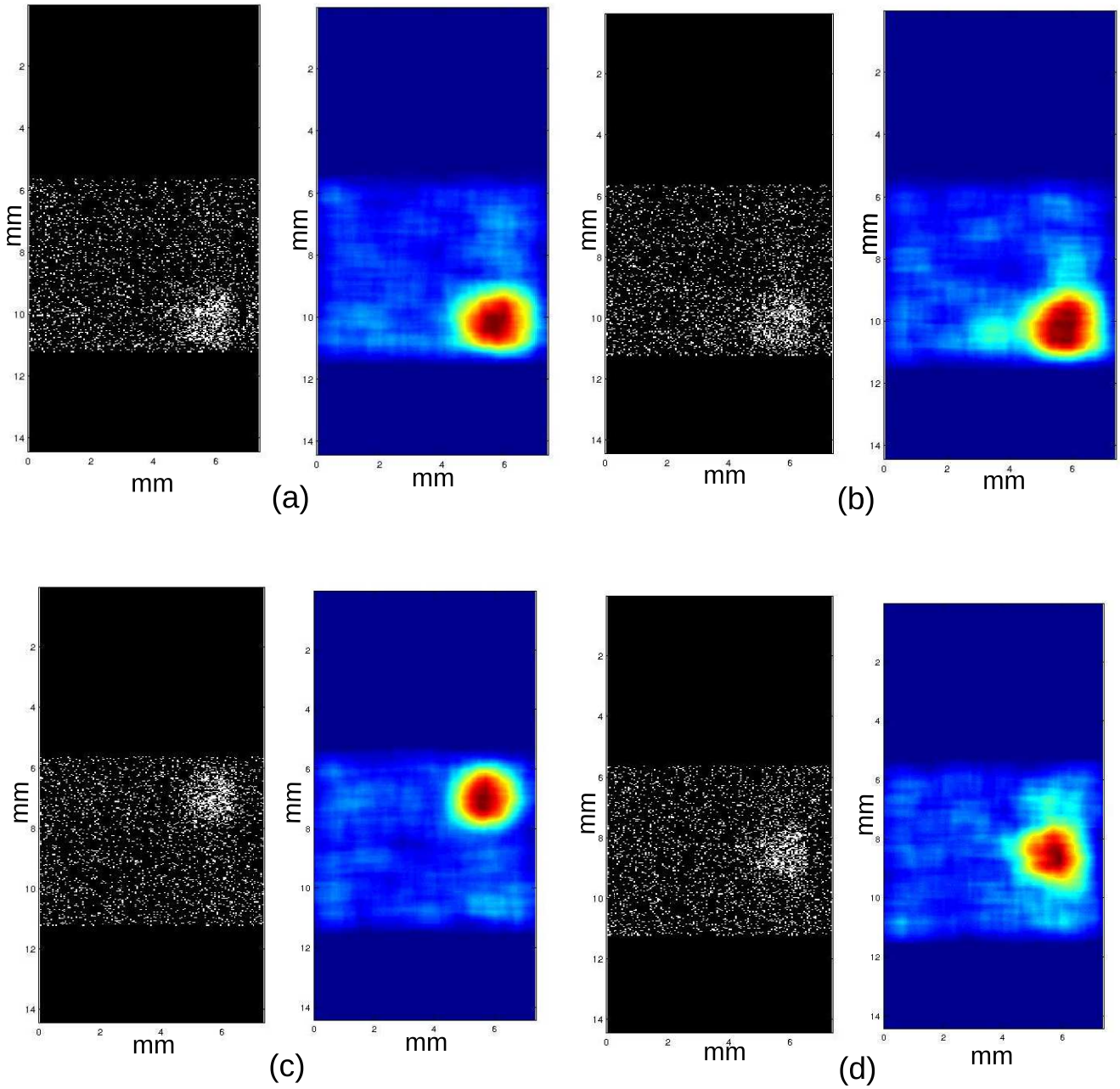

Figure 4.3: (a), (b), (c) and (d) are 4 instances of gamma scintillations detected by 1.6mm scintillator pitch.

number of gamma scintillations per block is calculated to be 14.45. With a USB bandwidth of approximately $53Mbps$, the time it takes to read out a block of $50MB$ is $7.4s$. Thus, the measured count rate is $1.95cps$.

The GATE simulation for dead time calculations are shown in Fig. 4.9. Fig. 4.9(a) shows the detector and a point source situated at a distance of $4cm$ and Fig. 4.9(b)

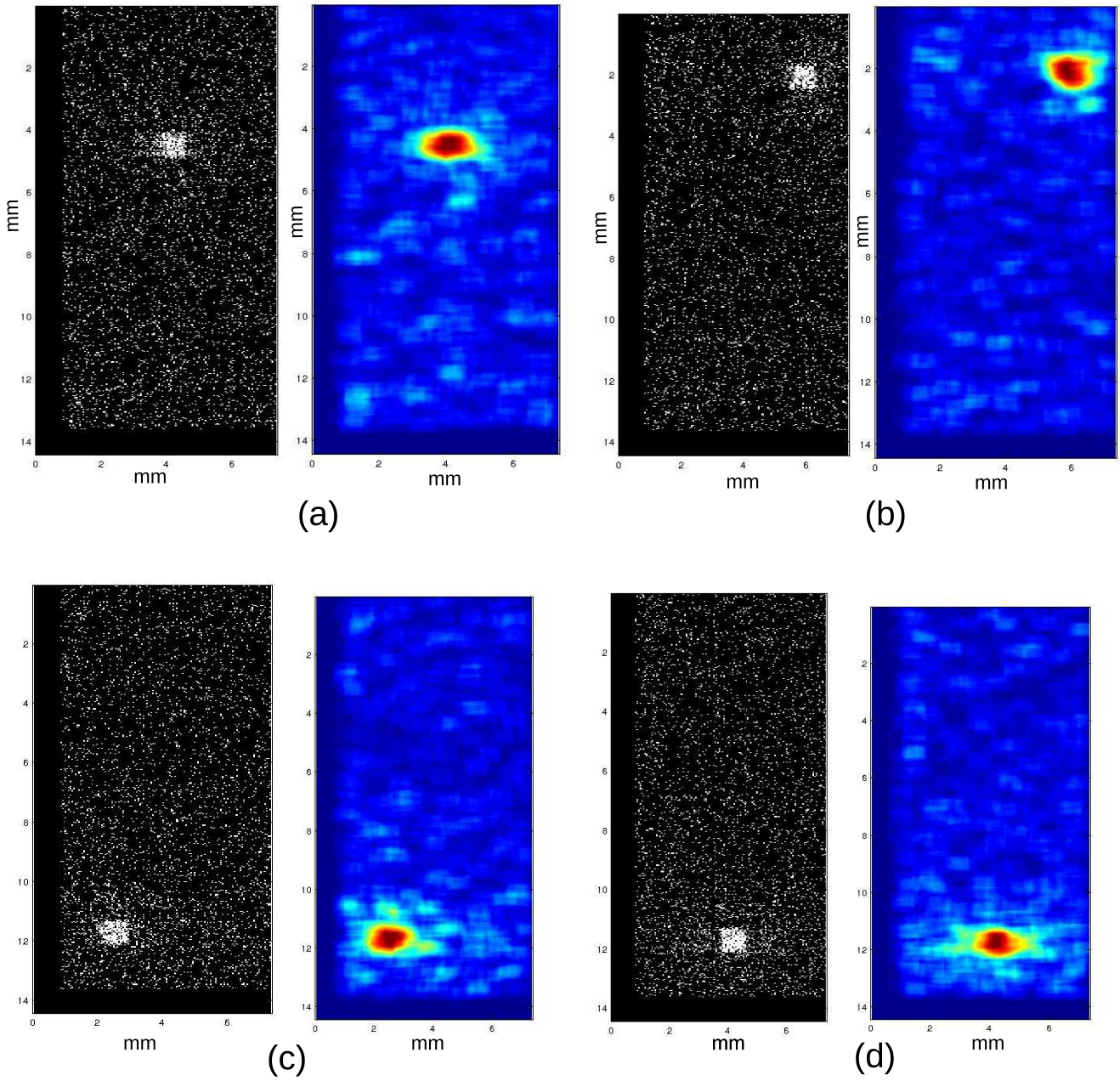

Figure 4.4: (a), (b), (c) and (d) are 4 instances of gamma scintillations detected by 0.8mm scintillator pitch.

shows gamma photons emitting out of the radioactive source. Fig. 4.10 shows the energy spectrum of the LYSO scintillator. The accumulated count rate beyond $280keV$ is calculated to be $1.95cps$. Count rate for energy below $280keV$ is not detected due to DCR.

Unlike mode-0, mode-2 is an event-driven based readout. Thus, the number gamma

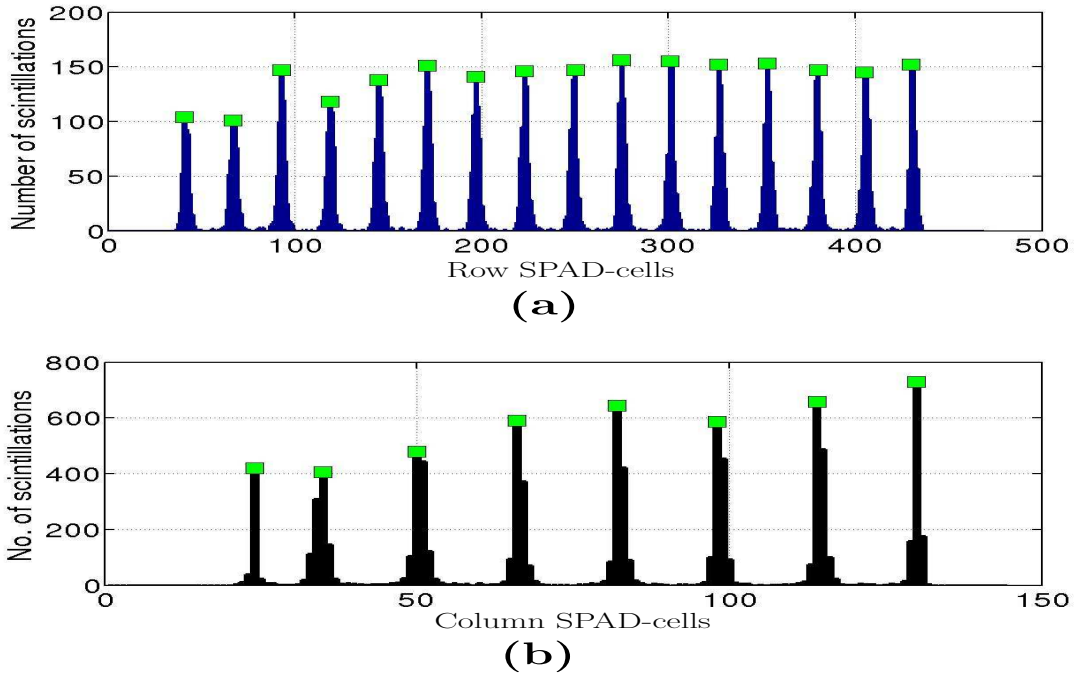

Figure 4.5: (a) Row-wise centroid histogram for 0.8mm pixel scintillator. (b) Column-wise centroid histogram for 0.8mm pixel scintillator.

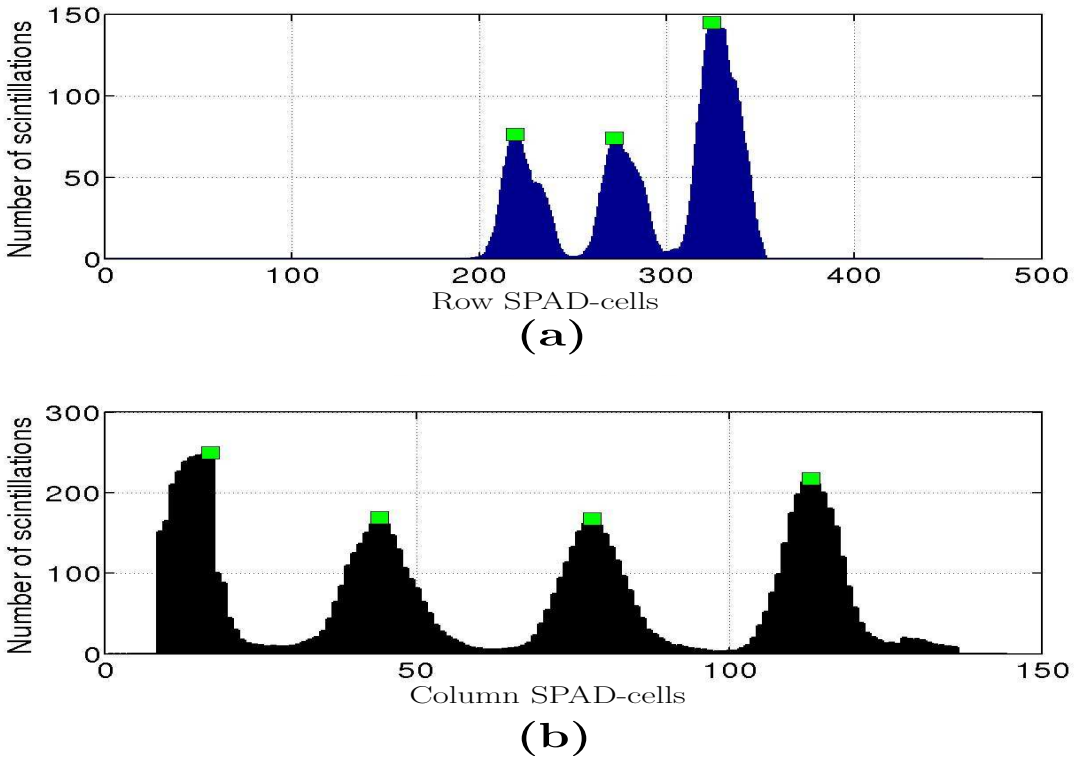

Figure 4.6: (a) Row-wise centroid histogram for 1.6mm pixel scintillator. (b) Column-wise centroid histogram for 1.6mm pixel scintillator.

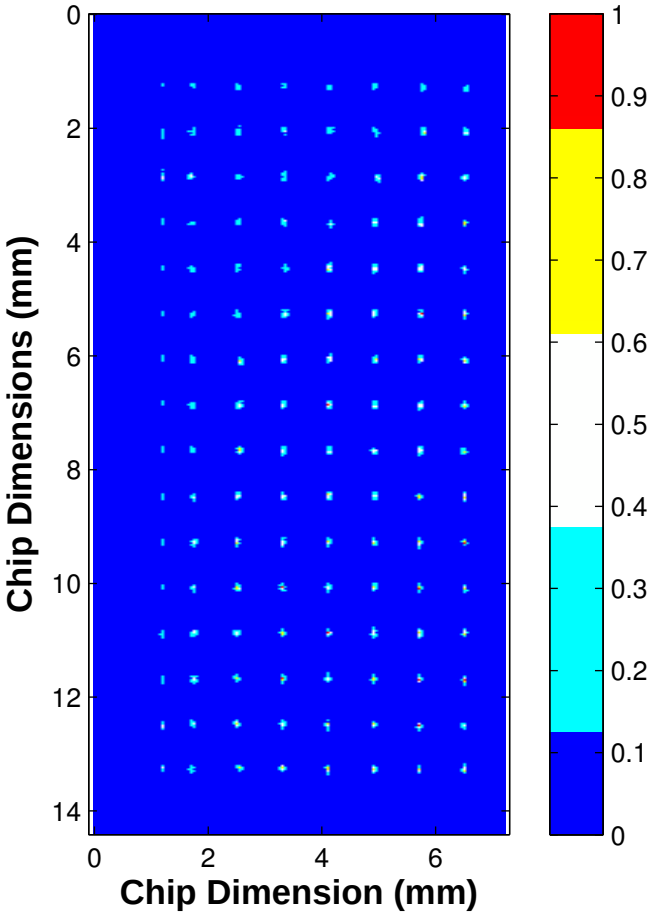

Figure 4.7: Normalized 2D histogram for $0.8mm$ pixel scintillator.

scintillations that can be captured using mode-2 is much higher than mode-0. This will result in higher measured count rate. The dead time in mode-2 is roughly $100\mu s$ and it is fixed i.e., it does not change with the number of gamma scintillations occurring in a same window. In such scenario, two gamma scintillations, if occurred within a same window time, will be counted only as 1. Thus, this induces an error in the counting mechanism [31]. To correct this error, nonparalyzable model is adopted for calculation. The nonparalyzable model is given by Eqn. 4.3

$$\begin{aligned} n = & \quad \frac{m}{1 - m.\tau} \quad where, \\ n = & \quad \text{true interaction rate} \\ m = & \quad \text{recorded interaction rate} \tau = \quad \text{sytem dead time} \end{aligned} \tag{4.3}$$

Substituting $7545.2cps$ for true count rate and $100\mu s$ for dead time, the recorded count rate is measured to be $7015.8cps$.

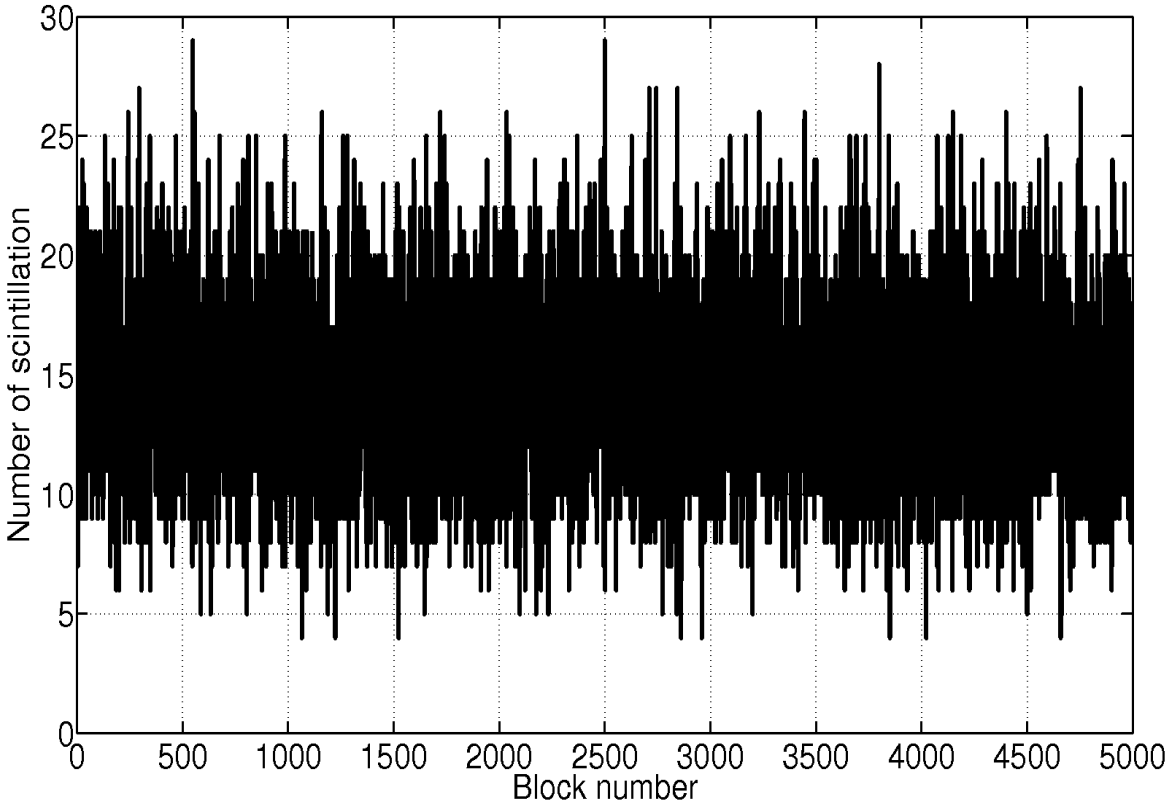

Figure 4.8: Number of gamma scintillations per block.

4.3 Timing Resolution

Timing resolution of a PET scan system is an important figure of merit and affects directly the reconstructed image quality in TOF-PET scan system design. The timing resolution of the PET scan system depends on the scintillator and TDC timing performance. The scintillator timing performance is purely material dependent and is characterized by two properties, namely, the rise time[1](t_r) and decay time[2](t_d). For TDC timing characterization, single-photon timing resolution (SPTR) measurements are adopted.

4.3.1 Experimentation setup and Methodology for SPTR

SPTR measurements are executed with MD-SiPM kept in photon-starved mode. For SPTR measurement, A pulsed beam from a laser setup is synchronized with the VCOEN window of the chip. The laser setup under use consists of a commercial $405nm$ blue laser source, an attenuator and a neutral density filter. The laser source is state-

[1]The time a scintillator takes to generate the visible light photons upon gamma photon absorption.

[2]Decay time is defined as the time after which the intensity of the light pulse generated returns to $1/e$ of its maximum value.

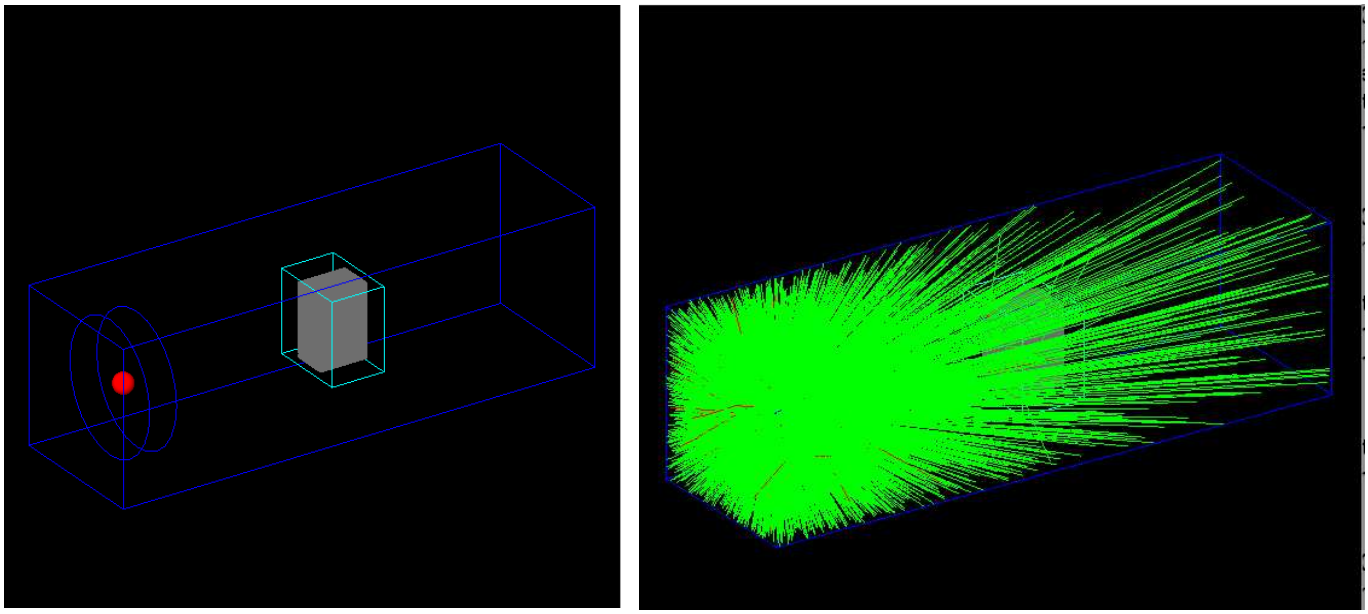

Figure 4.9: (a) The source and detector placement. (b) GATE simulation showing gamma photons emitting out of the source.

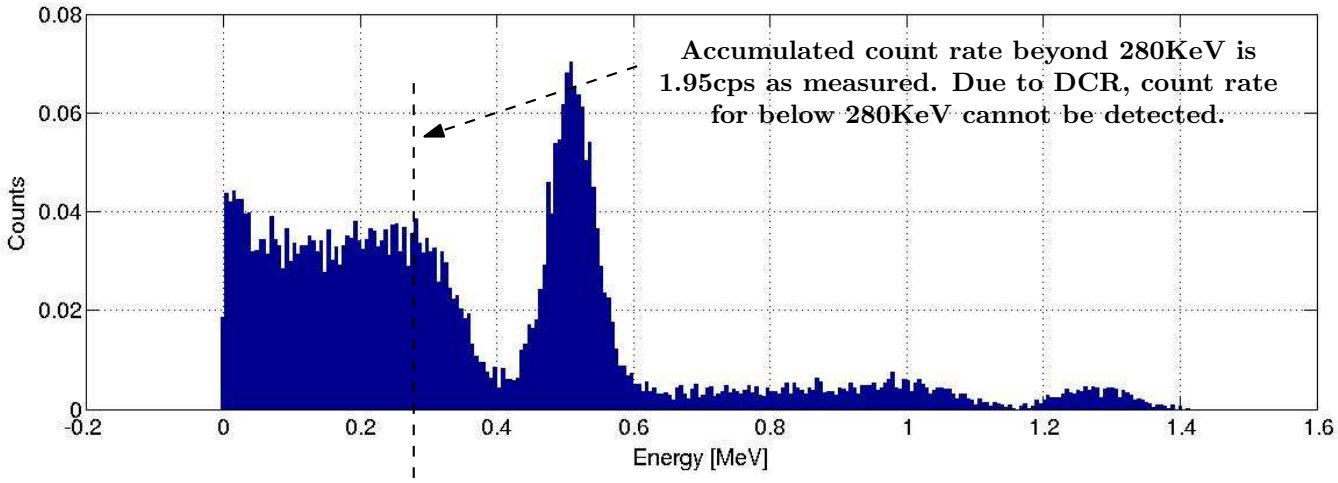

Figure 4.10: Energy spectrum of LYSO scintillator.

of-the-art equipment (manufactured by ALDS GmBH, Germany) with a FWHM jitter of $40ps$. To reduce the DCR corruption of TDC timing data, 10% of the extremely hot SPAD-cells (*Screamers*) are masked. For SPTR, the chip is configured in mode-0 with a VCOEN time of $2.5\mu s$. The laser equipment allows for an external trigger mechanism

which is utilized here to synchronize it with VCOEN window time. An output signal from FPGA is generated to start the laser trigger with VCOEN activation. The laser is operated with the system clock of $20MHz$ generating the pulse every $50ns$. Thus, for a $2.5\mu s$ window time, the laser is pulsed 50 times. Hence, the TDC data must contain 50 peaks per frame. Fig. 4.11 shows the SPTR setup.

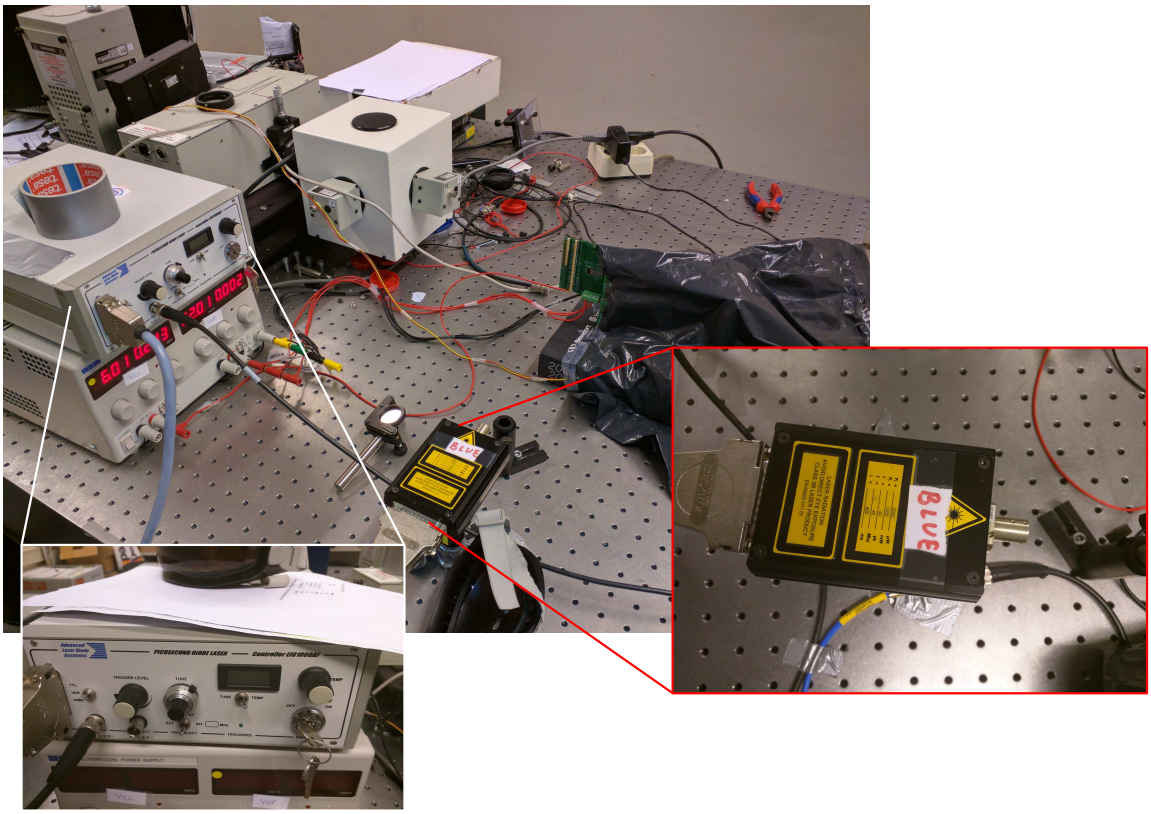

Figure 4.11: SPTR measurement setup.

4.3.2 SPTR Results

The SPTR measurement results are presented in the Fig. 4.12. The Laser is triggered with the $20MHz$ system clock frequency. The first 10 laser peaks are zoomed in for better observation. For the SPTR measurement, the VCOEN is kept activated for $2.5\mu s$.

4.3.3 Impact of DCR on TDCs

The TDCs are employed for capturing multiple timestamps for visible light photons generated by gamma photon absorption in scintillator. Thus, the accuracy of TOA is highly dependent on the availability of TDCs for capturing TOA upon a gamma event. DCR can bring down the availability of TDCs drastically. If the DCR is high, the TDCs are occupied by dark counts and, hence, cannot be utilized for acquiring timing information.

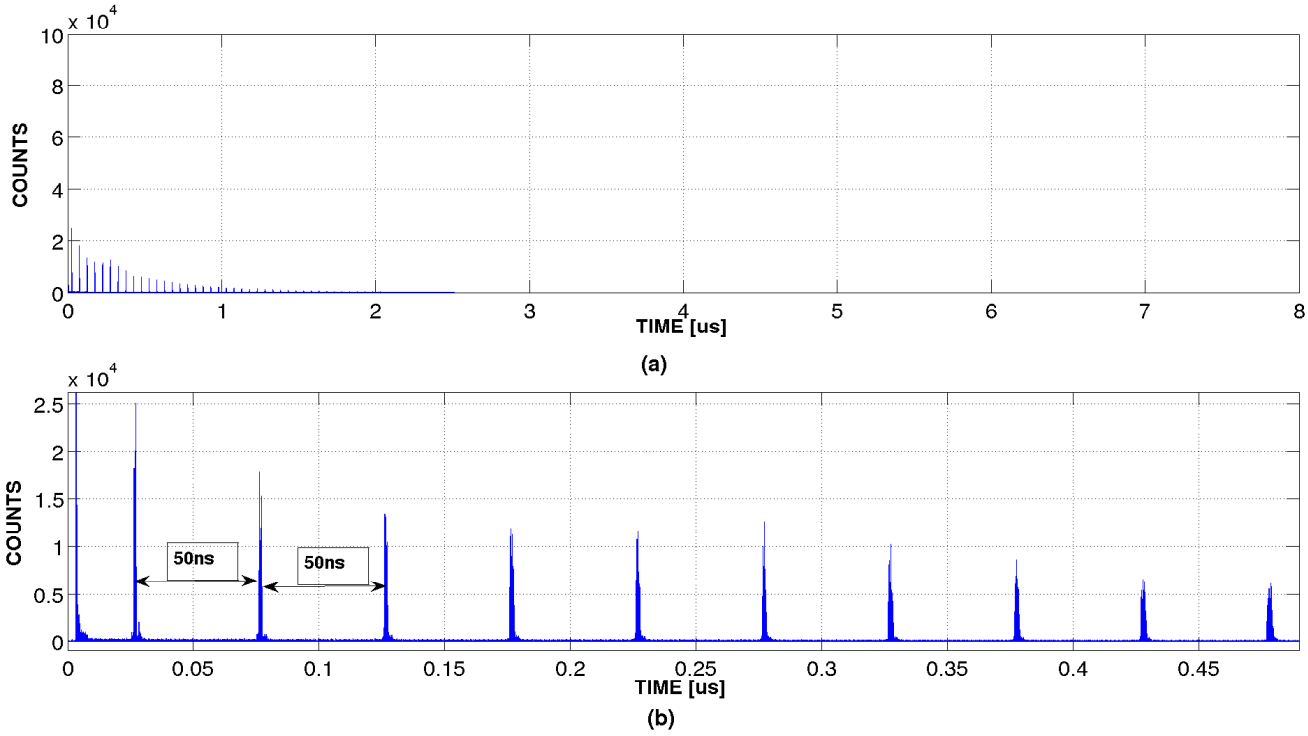

Figure 4.12: SPTR measurement with a $405nm$, blue laser. (a) Complete TDC histogram for TDC No. 260. (b) TDC histogram zoomed on the first 10 laser peaks.

To study, with reasonable accuracy, the impact of DCR on TDCs, actual DCR measurements are carried out which are then inserted into the simulation. We acquired DCR data in mode-0 with a VCOEN period of $1\mu s$ and operating the SPADs at $21.7V$. During the acquisition, the chip is cooled down using a fan and water cooling system. Next, a simulation is performed where the masking is varied from 0% to 50% in steps of 10%. Also, the simulation is executed for 4 smart reset periods [$50ns$, $100ns$, $200ns$, $300ns$]. Once we successfully generate the DCR data for a particular masking and smart reset time interval, PDF of fired TDCs is calculated.

Fig. 4.13(a) through (d) shows the CDF of free TDCs with different masking profiles and smart reset intervals.

4.4 Light Crosstalk

Under ideal condition, the scintillator is perfectly attached to the MD-SiPMs and no light photon from one scintillator pixel would trigger sensors in the other scintillator pixel. Practically, the scintillator is glued to the MD-SiPM by a transparent glue with a thickness of about $200\mu m$. Due to the difference in refractive index of glue and scintillator, some photons may refract and fall on the photosensor designated to adjacent scintillator pixel. This results in a phenomenon called as light crosstalk. Fig.

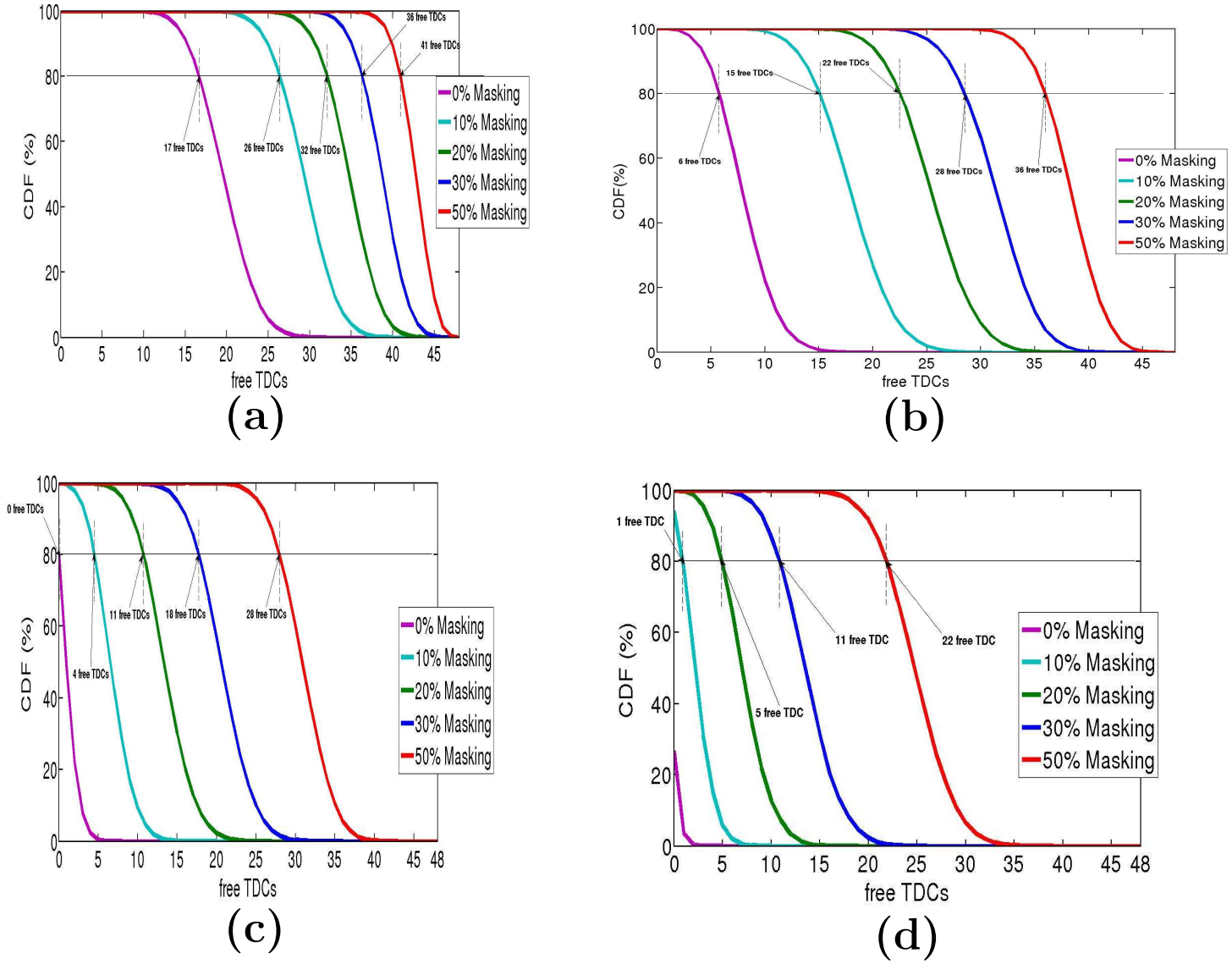

Figure 4.13: (a) CDF of free TDCs for 50ns smart reset period. (b) CDF of free TDCs for 100ns smart reset period. (c) CDF of free TDCs for 200ns smart reset period. (d) CDF of free TDCs for 300ns smart reset period.

4.14 shows the spread of scintillations for a 1.6mm scintillator pixel pitch. The light crosstalk results in scintillation to be extended in the adjacent MD-SiPM units and, thereby, the scintillation width comes around to be approximately 2mm. Similarly, Fig. 4.15 shows the scintillation spread for the 0.8mm scintillator pixel where the light crosstalk is approximately 1.32mm

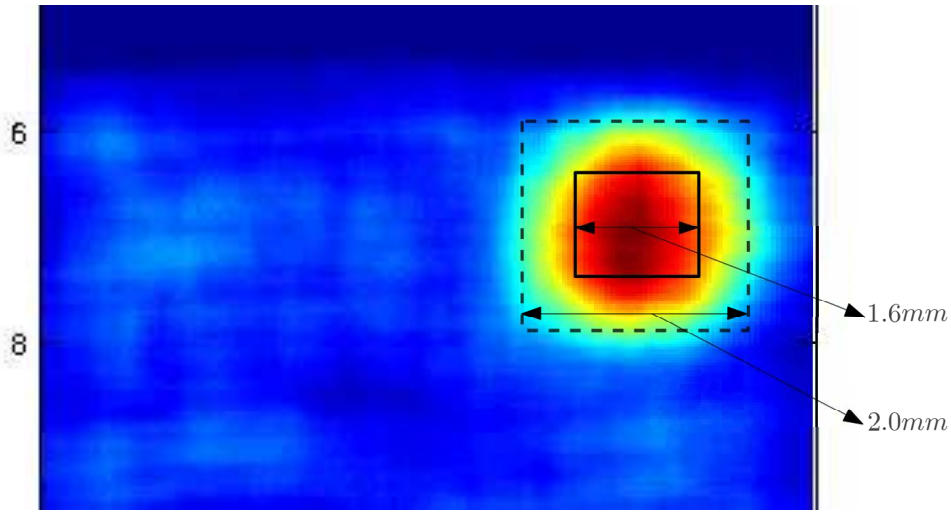

Figure 4.14: 1.6mm pitch scintillator with light crosstalk resulting in the scintillation width to be approximately 2.0mm.

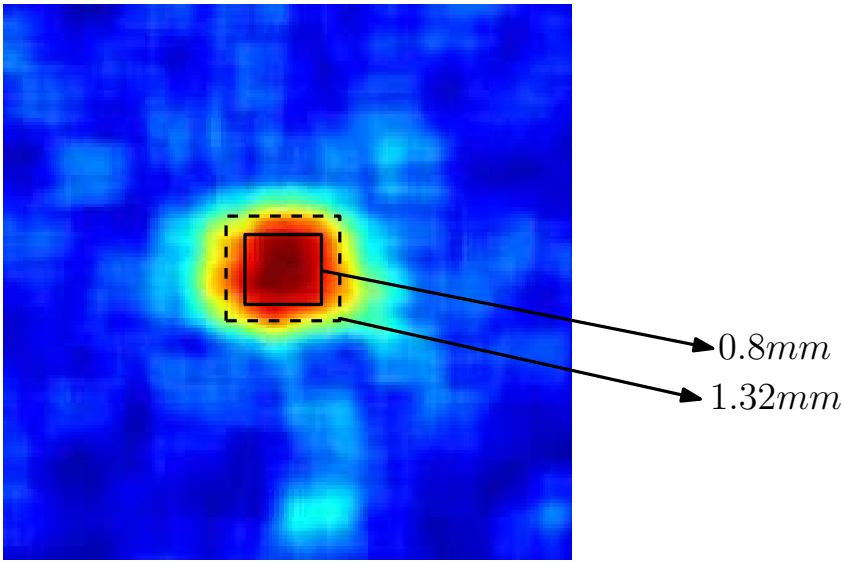

Figure 4.15: 0.8mm pitch scintillator with light crosstalk resulting in the scintillation width to be approximately 1.32mm.

Timing Estimation with Multiple Timestamps

5

In TOF-PET scan systems, the quality of 3D functional image obtained from scanner depends directly on the timing resolution of scanner [32]. The timing estimation can be done in two ways: single photon timing estimation or a multiple photon timing estimation in case of multiple TDCs. When using an array of SPADs for photon detection purposes, each SPAD can be coupled with a per SPAD-cell TDC to measure the time of arrival of each photon that impinges on the associated SPAD. The drawback of using this approach is drastic reduction in fill factor leading to a lower photon detection probability. The MD-SiPM array chip employed for PET detector development utilizes a column parallel TDC approach where 1 TDC is shared with every 3^{rd} pixel in a column. With a total of 144 SPAD-cell columns, the total number of TDCs present is 432 in the 9×18 MD-SiPM array chip. Therefore, timestamps for multiple photons generated during a gamma event can be recorded without compromising the array fill factor.

The main contributions presented in this chapter is to execute a light-transport monte carlo simulation of $0.8 \times 0.8 \times 10mm^3$ crystal scintillator with a point radioactive source in GATE. Earlier, emission PDF for photoelectrons was generated via matlab and subsequently used in timing estimation using algorithms like MLE, BLUE, etc. To have a more realistic timing estimation, GATE simulation is executed to generate enough statistics for TOA. These statistics are, then, used in matlab to have a better approximation of photoelectron PDF.

5.1 Theory

In PET scan systems, coincidence resolving time (CRT) is an important figure of merit directly influencing the reconstructed image quality [33]. The coincidence is based on the principle of detecting the two collinear gamma photons emitted during an annihilation event. In PET scan detectors, the main timing resolution constraints used to come from the scintillators response time and photosensor jitter. With the technological advancements, scintillators with faster response time are available resulting in more research and development in designing a TOF-PET scanner system. With the MD-SiPM array chip having 432 TDCs shared among the SPAD pixels, timestamps can be obtained for multiple photons generated during the scintillation process. To completely understand the problem of time estimation using multiple photon timestamps, we must look into the statistics of scintillation based detectors.

5.1.1 Statistical behaviour of scintillation photons.

Photon counting is a crucial part of TOF-PET scanner systems and photon counting statistics sets the limit on the timing resolution [34]. To understand the photon counting statistics, we start with a basic assumption that a gamma photon was absorbed at time Θ and the total number of photons emitted by the scintillator upon absorption is N. The photon emission inside the scintillator possesses an independent and identically distributed probability density function (PDF). The resulting PDF for emitted photon is denoted by $f_{emi}(t|\Theta)$ and modeled as a double exponential depending upon two factors: the rise time t_r and the decay time t_d [2]. The PDF for scintillation photon is given by Eqn. 5.1 [35].

$$f_{emi}(t|\Theta) = \begin{cases} 0 & ,\forall t : t < \Theta \\ \frac{e^{-\frac{(t-\Theta)}{t_d}} - e^{-\frac{(t-\Theta)}{t_r}}}{t_d - t_r} & ,\forall t : t \geq \Theta \end{cases} \tag{5.1}$$

Rise time, t_r, of scintillator is the time it takes to reach the maximum intensity upon gamma photon absorption and decay time, t_d, is the time it takes for the scintillation to stop after the gamma photon absorption. For a finer coincidence resolving time, both t_r and t_d needs to be as small as possible. The timestamps associated with unsorted photons which are generated as a result of scintillation process are calculated using PDF given by Eqn. 5.1 [24]. Fig. 5.1(a) shows the normalized PDF response of the scintillation photons exhibiting double exponential behaviour as given by Eqn. 5.1 and Fig. 5.1(b) shows the finite rise time of the PDF at time $t = 0.1\mu s(T_\circ)$ i.e., at the start of scintillation. Till now, we have assumed SPADs to be ideal and hence the

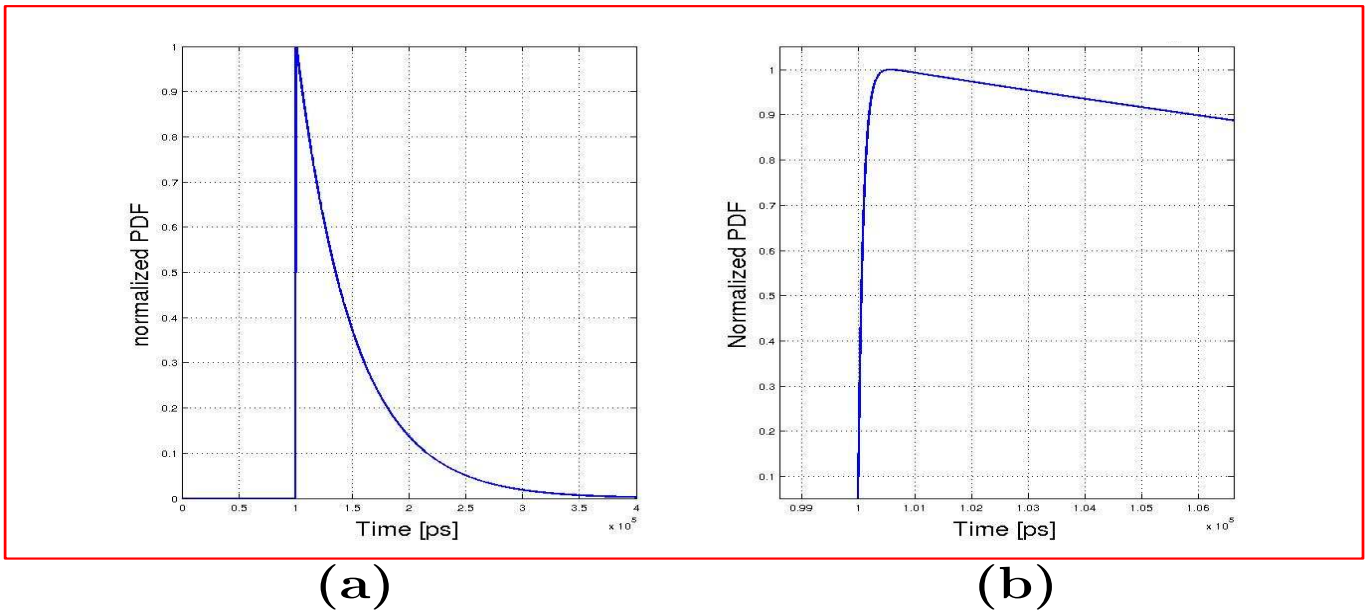

Figure 5.1: (a) Normalized PDF of the emitted photon upon a scintillation. (b) Normalized PDF zoomed at time $t = 0.1\mu s(T_\circ)$.

above timestamp estimation does not take into account the SPAD jitter, TDC jitter and electrical jitter. Let $\mathcal{N}[\mu,\sigma^2](t)$ be a normal distribution representing the total jitter of the system as SPAD, TDC and electrical jitter are additive noise in nature [32]. σ^2 represents the timing uncertainty arising out of all the sources i.e., SPADs, TDCs, pixel and readout electronics. To accommodate the jitter effects of the above mentioned sources, the probability density function for time mark estimation given in Eqn. 5.1 is convolved with $N[\mu,\sigma^2](t)$. The resulting probability density function is given by Eqn. 5.2.

$$f_{emi+jitter}(t|\Theta) = f_{emi}(t|\Theta) * \mathcal{N}[\mu,\sigma^2](t) \tag{5.2}$$

The PDF resulting from Eqn. 5.2 is utilized to calculate time of registration of detected photoelectrons. The PDF can be used for obtaining either single-photon timing information or multiple-photon timing information. According to order statistics, if in a scintillation process a total of n photons are emitted, the probability density function of the k^{th} photon's time of arrival can be estimated by the Eqn. 5.3 [36].

$$p_k(t|\Theta) = \frac{n!}{(k-1)!(n-k)!}[1 - F_{emi+jitter}(t|\Theta)]^{(n-k)}[F_{emi+jitter}(t|\Theta)^{(k-1)}]f_{emi+jitter}(t|\Theta) \tag{5.3}$$

Where, $F(t|\Theta)$ is the Cummulative Density Function (CDF) corresponding to the PDF in Eqn. 5.2. Fig. 5.2 shows the block diagram of the methodology adopted for estimat-

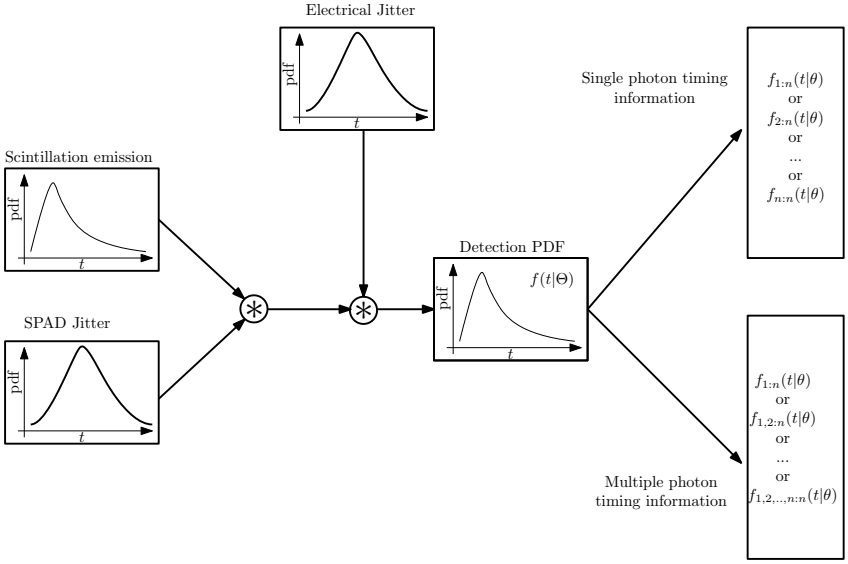

Figure 5.2: Block diagram of scintillation photon timestamp estimation methodology [2].

ing the time stamps of the scintillation photons that are emitted upon gamma photon absorption. The SPAD and electrical jitter are gaussian and hence modeled as additive noise which is convolved with the scintillation photon PDF to generate the detection PDF which is used for timestamp estimation.

5.1.2 Cramér-Rao Lower Bound for Time Estimation of Multiple Photons

From Eqn. 5.3, an estimator can be devised to accurately extract the timestamp informations for multiple photons that were emitted from a scintillation process. To ascertain the performance of the estimator, a benchmark is needed for comparison. Cramér-Rao Lower Bound (CRLB) is used for benchmarking the performance. In estimation theory, CRLB marks the absolute lower bound on the variance of an unbiased estimator [32]. CRLB can be an useful tool in determining the following aspects:

1. Any unbaised estimator that achieves the CRLB is considered to be fully efficient and is termed as Minimum Variance Unbiased (MVU) estimator
2. Any unbiased estimator can be compared to the theoretical bound established by CRLB to analyze its performance (closer the variance of an estimator to CRLB, the better its performance).
3. Since CRLB provides an absolute lower bound, impossible unbiased estimator designs can be ruled out immediately as achieving a variance lower than CRLB is impossible. This test is often termed as feasibility analysis.

Although CRLB defines a lower bound on the variance an unbiased estimator can achieve but it does not guarantee that such an unbiased estimator exist. To tackle the problem statement of estimating multiple timestamps, the starting point is set to single photon time-mark estimation [32]. Single photon unbiased timestamp estimator can be modeled by the Eqn. 5.4.

$$\begin{aligned} \hat{T_\circ} &= t_q \ - \ A \qquad (a) \\ where, \ A &= E[p_q|t_\circ = 0] \qquad (b) \end{aligned} \tag{5.4}$$

$E[p_q|t_\circ = 0]$ denotes the calibration coefficient that is employed to nullify the offset in the timestamp of the q^{th} photoelectron whose time of registration is defined by the PDF p_q. This results in the estimator becoming an unbiased one. Fisher information can be calculated for a single-photon timemark estimation from its PDF. The inverse of Fisher information is the CRLB. Fisher information for single photon timestamp estimation can be given by Eqn.

$$I(T_\circ) = \int_{-\infty}^{\infty} \left[\frac{\partial}{\partial T_\circ} log(p_q(t|T_\circ)) \right]^2 .p_q(t|T_\circ)dt \tag{5.5}$$

Applying chain rule to rewrite $p_q(t|T_\circ)$

$$p_q(t|T_\circ) = g_q(t - T_\circ) \tag{5.6}$$

Eqn. 5.5 can be re-written as

$$I(T_\circ) = \int_{-\infty}^{\infty} \left[\frac{\partial}{\partial T_\circ} log(g_q(t - T_\circ)) \right]^2 .g_q(t - T_\circ)dt \tag{5.7}$$

$$I(T_\circ) = \int_{-\infty}^{\infty} \left[\frac{1}{g_q(t - T_\circ)} . \frac{\partial}{\partial T_\circ} g_q(t - T_\circ) \right]^2 .g_q(t - T_\circ)dt \tag{5.8}$$

$$I(T_\circ) = \int_{-\infty}^{\infty} \left[\frac{\partial}{\partial T_\circ} g_q(t - T_\circ) \right]^2 \frac{1}{g_q(t - T_\circ)} dt \tag{5.9}$$

Eqn. 5.9 represents the fisher information for q^{th} photoelectron with p_q as its PDF.

5.2 GATE Simulations

In PET scan systems, monte carlo simulations can prove to be quite helpful in overall detector design optimization and imaging protocols. The quality of these optimizations directly depend on how realistic the simulation environment is [37]. In monte carlo simulations, an interaction $\mathcal{K}$ of a random process is analyzed. PDF of the random process is known a priori and simulation is executed by randomly sampling the PDF for occurrence of that interaction $\mathcal{K}$. GATE is an open-source software design to execute monte carlo simulations in the medical imaging domain. GATE is based on Geant4 (GEometry ANd Tracking) toolkit which is employed for simulating the interactions, a particle experiences while traversing through matter [38, 39]. The main advantage of using GATE toolkit is to simulate the light transport inside the scintillator and also to account for the scintillator's non ideal behaviour with an aim of estimating how a real scintillator would interact with gamma photons.

5.3 Maximum Likelihood Estimators (MLE)

In MLE, given a finite data set X_i, where i $\in [1, n]$, whose presumed probability distribution is dependent on an unknown parameter θ, the goal of likelihood estimation is to approximate the unknown parameter θ of the assumed PDF such that it closely represents the given dataset. For instance, if the dataset X_i, where $i \in [1, n]$ is assumed to have a gaussian distribution $\mathcal{N}[\mu, \sigma^2]$, then the aim of likelihood is to find out a good approximation of the mean using the given dataset X_i.

Maximum likelihood estimation (MLE) is step further in determining the best possible estimate. It is quite reasonable that if for a given dataset X_i $i \in [1, n]$, the best estimate θ_k will also maximize the likelihood function for the given dataset. For independent and identically distributed sample, the combined density function represents the likelihood function as well and is given by Eqn. 5.10 through 5.12 [40].

$$f(x_1, x_2, ...x_n|\theta) = f(x_1|\theta) \times f(x_2|\theta) \times \cdots f(x_n|\theta) \tag{5.10}$$

$$\mathcal{L}(\theta) = f(x_1, x_2, ...x_n|\theta) \tag{5.11}$$

$$\mathcal{L}(\theta) = \prod_{i=1}^{n} f(x_i|\theta) \tag{5.12}$$

Thus, the best estimate of unknown parameter θ_k is solution to the differential of likelihood function in Eqn. 5.12. As natural logarithm function is monotonically increasing function, the θ_k maximizing $\mathcal{L}(\theta)$ will also maximize $ln\ \mathcal{L}(\theta)$. The logarithm operation simplifies the differentiation process. Eqn. 5.13 gives the log-likelihood function.

$$ln\ \mathcal{L}(\theta) = \sum_{i=1}^{n} ln\ f(x_i|\theta) \tag{5.13}$$

The solution to Eqn. 5.13 gives the best estimate of unknown parameter θ_k for a given dataset X_i $i \in [1, n]$.

Similarly, in the case of multiple time-stamp estimation, a likelihood function can be designed to model the timestamps for the first Q photoelectrons for an unknown parameter $T_\circ$ [32]. The likelihood function and the associated fisher information for censored type II dataset of ordered statistics are given by Eqns. 5.14 and 5.15 respectively.

$$\mathcal{L}(t_1, t_2, ...t_Q|T_\circ) = \frac{R!}{(R-Q)!}\prod_{q=1}^{Q}[f(t_q|T_\circ)]\{1 - F(t_Q|T_\circ)\}^{R-Q} \tag{5.14}$$

$$I_{1:Q} = \int_{-\infty}^{\infty}\left[\frac{\partial}{\partial T_\circ}log(h(t|T_\circ))\right]^2\left[\sum_{q=1}^{Q}p_q(t|T_\circ)\right]dt \tag{5.15}$$

$$\text{where, } h(t|T_\circ) = \frac{f(t|T_\circ)}{1 - F(t|T_\circ)} \tag{5.16}$$

$$f(t_q|T_\circ) = f_{emi+jitter}(t_q|T_\circ) \text{ (from Eqn. 5.2)} \tag{5.17}$$

Where R in Eqn. 5.14 is the total number of photoelectrons detected.

5.4 Best Linear Unbiased Estimations (BLUE)

The approach for finding the best estimator through maximum likelihood function (MLE) is often computationally intensive. For instance, given a dataset X_i *where*, $i \in [1, n]$, despite knowing the mean (μ) and variance (σ^2), the approximation for the best PDF cannot be made. In such cases, a sub-optimal approach is undertaken. BLUE is one such approach which relies on the assumption that a given dataset X_i $i \in [1, n]$ can be modeled as a linear regression [41].

A linear timemark estimator can be expressed by Eqn. 5.18 Where $w_q^{(p)}$ represents a weight associated with a timemark for the q^{th} photoelectrons that is detected. The variable p simply denotes the type of weights that can be selected and represents different linear estimator models.

$$\hat{T_\circ}^{(p)} = \sum_{q=1}^{Q} t_q w_q^{(p)}, \quad p \in [1, 3] \tag{5.18}$$

For $p = 1$, a simple mean estimator is modeled. The weight for this estimator is simply the mean of the ordered group of Q photoelectron that were detected and is expressed by 5.19.

$$w_q^{(1)} = \frac{1}{Q}, \quad q \in [1, Q] \tag{5.19}$$

The second kind of linear estimator ($p = 1$) is based on the idea that each timestamp t_q associated with a q^{th}, *where* $q \in [1, Q]$, photoelectron has its weight depends on its variance. Thus, the weights for this estimator is given by Eqn. 5.20.

$$w_q^{(2)} = \frac{(\sigma^2(t_q))^{-1}}{\sum_{q=1}^{Q}(\sigma^2(t_q))^{-1}}, \quad q \in [1, Q] \tag{5.20}$$

In BLUE, the weights for individual timestamps t_q are dependent on the covariance matrix of the timestamps. Eqn. 5.21 and 5.22 illustrates the weights for BLUE [32].

$$\mathbf{W_q} = [w_1^{(3)}, w_2^{(3)}, ..., w_Q^{(3)}]^T \tag{5.21}$$

$$\mathbf{W_q^{(3)}} = \frac{\mathbf{C^{-1}.d}}{||\mathbf{C}^{-1/2}\mathbf{d}||_2^2} \tag{5.22}$$

Where, $\mathbf{d}$ is an unity column vector of length equal to the total number of photoelectron detected i.e., Q, and $\mathbf{C}$ is the covariance matrix of registered timestamps.

5.5 MLE and BLUE Simulation Results

To ascertain the performance of MLE and BLUE, simulation results are presented next. First, a GATE simulation is executed for a single pixel scintillator of $0.8 \times 0.8 \times 10mm^3$ dimensions along with a point radioactive source. The scintillator is modeled as mirrored tape. The monte carlo simulation is executed to obtain TOA of photoelectrons given by PDF in Eqn. 5.1. The simulation is executed to obtain enough statistics of the TOA of photoelectrons. The idea behind gathering enough statistics is to build a histogram in matlab and apply curve fitting techniques to finally approximate the emission PDF. Fig. 5.3 shows the obtained histogram from GATE simulations and curve fitting generated using matlab. Second, to account for the SPAD, TDC and

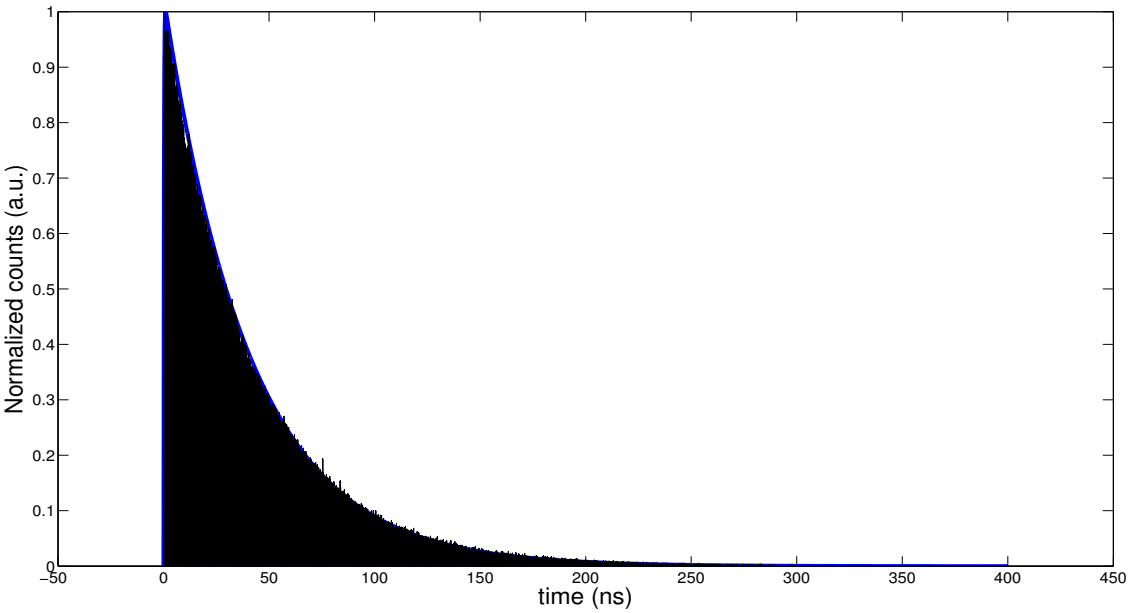

Figure 5.3: GATE simulation results of emission PDF for photo electrons generated upon gamma photon absorption within a scintillator.

other electrical circuits, a jitter of 300ps is assumed and a gaussian PDF is convolved

with emission PDF to obtain the final PDF for calculating time of arrival of photons. The final PDF is given in Eqn. 5.2. In the third step, a second monte carlo simulation is executed over matlab to sample the calculated PDF randomly to obtain the multiple timestamps. The timestamps are generated for 3 cases: 400, 600 and 800 photoelectrons (R). Once, the timestamps are available, MLE and BLUE algorithm are applied to calculate the coincidence resolving time.

Fig. 5.4 shows the simulation result of FWHM of CRT for both single and multiple timestamps with different number of sampled photoelectrons. It is observed that the CRT at FWHM is quite stable for multiple timestamps as against single photon timestamp. Moreover, as the number of sampled photoelectrons is increased, the CRT at FWHM gets better.

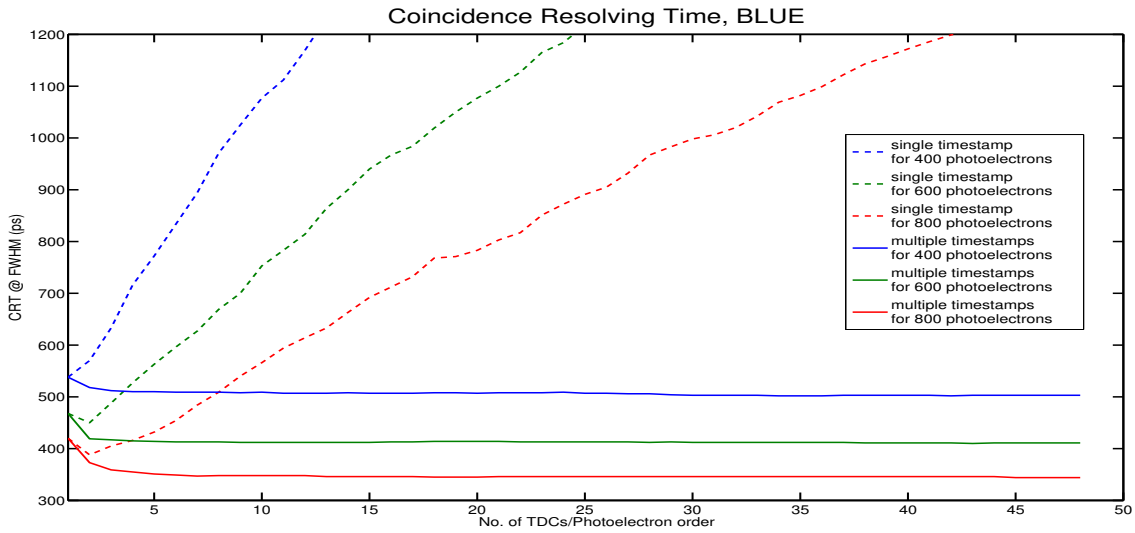

Figure 5.4: CRT @ FWHM versus photoelectron order calcuated using BLUE algorithm.

Similarly, Fig. 5.5 shows the simulation result for single and multiple timestamps with varying number of sampled photoelectrons. The methodology behind the emission PDF generation is identical for both BLUE and MLE. The same statistics sampled from second monte carlo simulation on matlab (which is fed into the BLUE algorithm) is used to calcualate CRT at FWHM using MLE algorithm.

Also, in Fig. 5.5, a comparison is made between CRT obtained from MLE versus BLUE algorithm. The TOA from the first 15 TDCs is marked as reference. As visible, the CRT at FWHM calculated from BLUE approximates the CRT at FWHM calculated from MLE more closely as the number of sampled photoelectron is increased from 400 to 800.

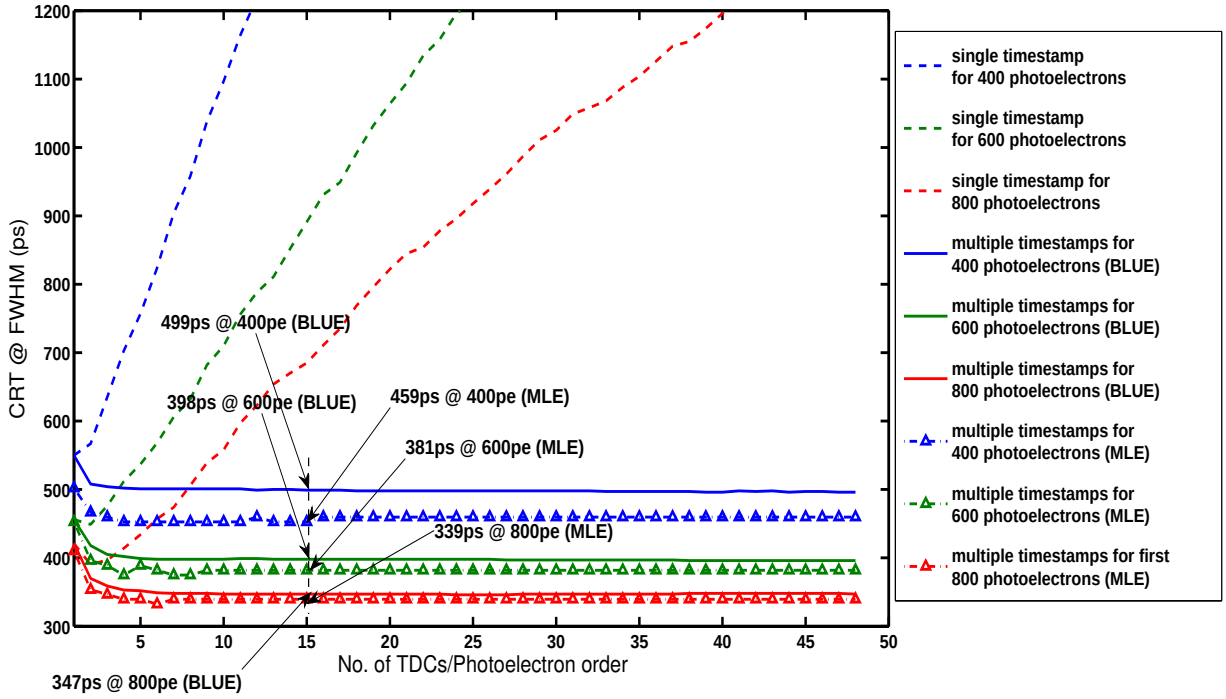

Figure 5.5: CRT @ FWHM versus photoelectron order calcuated using MLE algorithm.

6 Conclusion

The thesis is aimed at developing system level design for PET scan detector module. A brief summary is presented next describing about the firmware design, temperature sensing and readout, and chip configuration and its radiation characterization using a ^{22}Na radioactive source.

6.1 Summary and Contributions

The first chapter deals with the introduction to small-animal PET scan detector. Physics behind PET is discussed along with introduction to preclinical PET scan systems. State-of-the-art PET scan detectors and their inherent limitations are discussed next. Lastly, performance metrics for PET scan detectors are discussed along with a brief overview of intrinsic non-idealities that exist in PET scan detectors.

In chapter-2, the monolithic 9×18 MD-SiPM array chip is described. The discussion starts with an architectural overview of the chip followed by SPAD-cell array, SPADs and its figure of merit. Finally, readout architecture for different modes of operation is described. What follows next are the contributions of this thesis towards the project.

Chapter-3 elaborates the complete firmware design for the MD-SiPM array chip. The preliminary mode of operation called as mode-0, which has been designed over Xilinx Virtex-5, is ported to the cost effective Spartan-6 FPGA board followed by an extensive verification of newly ported mode-0. A new mode of operation, termed as mode-2, has been developed from scratch. Mode-2 is an event-driven based readout mechanism unlike mode-0. The new mode is developed to perform a complete energy register readout of all the cluster matrix with a much lower dead time compared to mode-0. This enables us to experiment with different crystal scintillator pixel size. Finally, a complete thermal characterization is performed with a single chip connected to the motherboard with water cooling mechanism. Lastly, the firmware designed to operate a chip in both mode-0 and mode-2 is adapted for multiple chip operation and readout.

In chapter-4, energy measurements with a radioactive source are performed for two scintillator choices (one with $1.6mm$ pixel pitch and another with $0.8mm$ pixel pitch). Along with energy measurements, scintillator pixel identification and light crosstalk are evaluated. Finally, SPTR measurements for TDC and impact of DCR on TDCs are discussed.

Chapter-5 explores the possibility of timing estimation using multiple timestamps. Here, monte carlo simulations are executed on GATE toolkit for a $0.8 \times 0.8 \times 10mm^3$ crystal scintillator with a point radioactive source. This is done to have a better approximation of emission PDF for photoelectrons. The TOA of photoelectrons generated from GATE simulations are utilized in matlab to achieve a more realistic emission PDF

for timing estimation using different algorithms like MLE, BLUE, etc.

6.2 Further Improvements

In the design of PET scan module, one of the design improvisation that can further enhance its performance is improving the packing fraction of the detector. It has been observed that using a 4×2 motherboard as shown in Fig. 3.12 introduces a lot of dead space between the two detectors. To avoid this, a new 4×1 configuration is designed and currently is in testing phase. Fig. 6.1 shows the 3D rendering of the new detector module board. A higher packing fraction will result in higher overall PET sensitivity

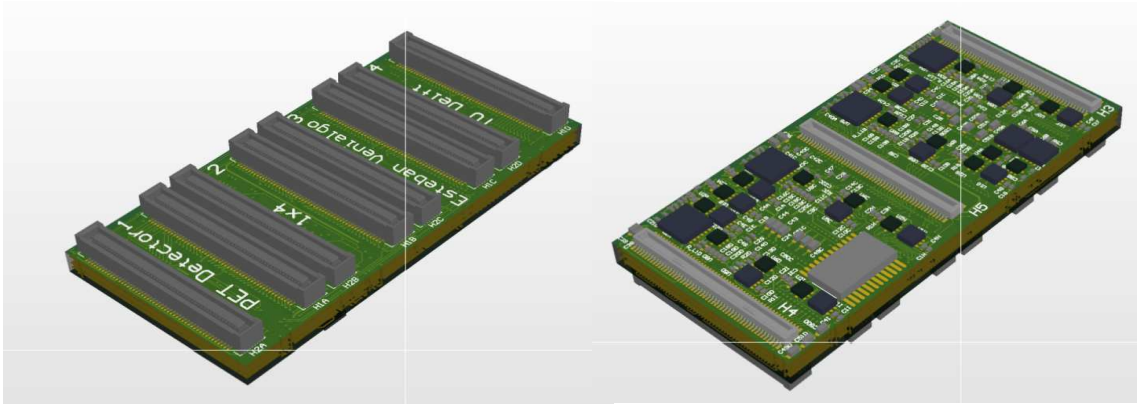

Figure 6.1: 4×1 motherboard for PET scan detector module. (a) Top layer with connectors for 4 MD-SiPM chips. (b) Bottom layer with connectors for Spartan-6 FPGA board.

as detectors are placed seamlessly and more detectors can fit within a same ring area. The second design improvement under consideration is use of a USB3.0 super highspeed link instead of USB2.0 highspeed link. USB3.0 link ensures that a non-stop readout is possible without having to temporarily pause the firmware for multiple chip readout due to bandwidth limitations.

6.3 Future of SPAD based PET sensors

SPADs possess a huge potential to be one of the best candidates for designing PET scanners. The fact that SPADs can be manufactured in CMOS process alongside the associated digital electronics is one of the reasons for a higher fill factor and thereby higher photon detection probability. Compared to PMTs, SPADs can be operated at much lower bias voltage which eliminates the need of investing in high-voltage power supplies. Lower operating voltage and high level of integration reduces the electronic jitter in SPAD based PET scan systems. Though, PMTs still cost less for a larger detector area, cost of SPAD based photosensors can be brought down by employing commercial CMOS process for fabrication. Also, as SPADs possess high tolerance for

magnetic fields, PET detectors designed using SPADs can be integrated with MRI scan systems for providing multi-modal imaging ability.

Bibliography

[1] Shingo Mandai, *Multichannel Digital Silicon Photomultipliers for Time-of-Flight PET Master of Science*. Doctoral thesis, Delft University of Technology, 2014.

[2] S. Mandai and E. Charbon, "Multi-channel digital SiPMs: Concept, analysis and implementation," *IEEE Nuclear Science Symposium Conference Record*, no. 1, pp. 1840–1844, 2012.

[3] A. L. Goertzen, Q. Bao, M. Bergeron, E. Blankemeyer, S. Blinder, M. Canadas, A. F. Chatziioannou, K. Dinelle, E. Elhami, H.-s. Jans, E. Lage, R. Lecomte, V. Sossi, S. Surti, Y.-C. Tai, J. J. Vaquero, E. Vicente, D. A. Williams, and R. Laforest, "NEMA NU 4-2008 Comparison of Preclinical PET Imaging Systems," *Journal of Nuclear Medicine*, vol. 53, no. 8, pp. 1300–1309, 2012.

[4] R. Badawi - Introduction to PET Physics (Division of Nuclear Medicine, University of Washington), "http://depts.washington.edu/nucmed/IRL/pet_intro/index.html."

[5] R. Yao, R. Lecomte, and E. S. Crawford, "Small-Animal PET: What Is It, and Why Do We Need It?," *Journal of Nuclear Medicine Technology*, vol. 40, no. 3, pp. 157–165, 2012.

[6] HumanData, "Spartan-6 FPGA Board XCM-206Z Series User's Manual,"

[7] Proteus, "http://www.apace-science.com/proteus/yap.htm."

[8] Omegapiezo, "No Titlehttp://www.omegapiezo.com/crystal_scintillators.html."

[9] M. E. Phelps, S. R. Cherry, and M. Dahlbom, *PET: Physics, instrumentation, and scanners*, vol. 1542. Springer-Verlag New York, 1 ed., 2006.

[10] S. J. Ament, S. Maus, H. Reber, H. G. Buchholz, N. Bausbacher, C. Brochhausen, F. Graf, M. Miederer, and M. Schreckenberger, *PET lung ventilation/perfusion imaging using 68Ga aerosol (Galligas) and 68Ga-Labeled macroaggregated albumin*, vol. 194. Springer Berlin Heidelberg, 2013.

[11] Z. Wang, P. J. Markiewicz, J. Kornhuber, T. Kuwert, and D. Merhof, "Comparison of Methods for Classification of Alzheimer ' s Disease , Frontotemporal Dementia and Asymptomatic Controls," pp. 0–5, 2013.

[12] C. Kuntner and D. Stout, "Quantitative preclinical PET imaging: opportunities and challenges," *Frontiers in Physics*, vol. 2, no. February, pp. 1–12, 2014.

[13] T. L. Morgan, "Quality Assurance for PET and PET/CT Systems," *Health Physics*, vol. 103, no. 6, pp. 810–811, 2012.

[14] Wikipedia. Positronium, "https://en.wikipedia.org/wiki/Positronium."

[15] C. C. Constantinescu and J. Mukherjee, "Performance evaluation of an Inveon PET preclinical scanner," *Phys. Med. Biol.*, vol. 54, no. 9, pp. 2885–2899, 2009.

[16] K. Herrmann, M. Dahlbom, D. Nathanson, L. Wei, C. Radu, A. Chatziioannou, and J. Czernin, "Evaluation of the Genisys4, a Bench-Top Preclinical PET Scanner," *Nuclear Medicine.*, vol. 54, no. 7, pp. 1162–1167, 2013.

[17] T. Okamoto, K. Ote, K. Sakai, A. Noda, K. Shimizu, K. Masuda, T. Ohmura, and M. Watanabe, "An animal PET scanner using flat-panel position-sensitive PMTs," pp. 74–80, 2014.

[18] Y. Shao, S. R. Cherry, S. Siegel, R. W. Silverman, and S. Majewski, "Evaluation of multi-channel PMTs for readout of scintillator arrays," vol. 390, pp. 209–218, 1997.

[19] R. Grazioso, N. Zhang, J. Corbeil, M. Schmand, R. Ladebeck, M. Vester, G. Schnur, W. Renz, and H. Fischer, "APD-based PET detector for simultaneous PET / MR imaging," vol. 569, pp. 301–305, 2006.

[20] C. Xu, E. Garutti, S. Mandai, and E. Charbon, "Comparison of Digital and Analog Silicon Photomultiplier For Positron Emission Tomography Application," 2013.

[21] L. H. C. Braga, L. Gasparini, L. Grant, R. K. Henderson, N. Massari, M. Perenzoni, D. Stoppa, and R. Walker, "A fully digital 8X16 sipm array for pet applications with per-pixel tdcs and real-time energy output," *IEEE Journal of Solid-State Circuits*, vol. 49, no. 1, pp. 301–314, 2014.

[22] P. D. Cutler, S. R. Cherry, E. J. Hoffman, W. M. Digby, and M. E. Phelps, "Design-Features and Performance of a Pet System for Animal Research," *Journal of Nuclear Medicine*, vol. 33, no. 4, pp. 595–604, 1992.

[23] W. W. Moses, "Time of Flight in PET Revisited," vol. 50, no. 5, pp. 1325–1330, 2003.

[24] M. W. Fishburn, *Fundamentals of CMOS single-photon avalanche diodes*. Doctoral thesis, Delft University of Technology, 2012.

[25] J. Melorose, R. Perroy, and S. Careas, *Microelectronic Circuits*, vol. 1. Oxford University Press, Inc. New York, NY, USA ©2007, 5 ed., 2015.

[26] A. Spinelli and A. L. Lacaita, "Physics and numerical simulation of single photon avalanche diodes," *IEEE Transactions on Electron Devices*, vol. 44, no. 11, pp. 1931–1943, 1997.

[27] C. Veerappan, *Single-Photon Avalanche Diodes for Cancer Diagnosis*. Doctoral thesis, Delft University of Technology, 2016.

[28] S. Henzler, *Time to Digital Converters*. Springer Series in Advanced Microelectronics, Springer, 2010.

[29] Xilinx, "Spartan-6 Family Overview Summary of Spartan-6 FPGA Features," *Product Specification*, vol. 160, no. DS160 v2.0, pp. 1–11, 2011.

[30] T.I., "Low-Power , Digital Temperature Sensor with SMAART Wire Interface," 2011.

[31] G. F. Knoll, *Radiation Detection and Measurement*. 3rd ed., 2000.

[32] E. Venialgo, S. Mandai, T. Gong, D. R. Schaart, and E. Charbon, "Time estimation with multichannel digital silicon photomultipliers," *Physics in medicine and biology*, vol. 60, no. 6, p. 2435, 2015.

[33] L. H. C. Braga, L. Gasparini, and D. Stoppa, "A time of arrival estimator based on multiple timestamps for digital PET detectors," *IEEE Nuclear Science Symposium Conference Record*, pp. 1250–1252, 2012.

[34] S. Seifert, H. T. van Dam, and D. R. Schaart, "The lower bound on the timing resolution of scintillation detectors," *Physics in Medicine and Biology*, vol. 57, no. 7, pp. 1797–1814, 2012.

[35] R. F. Post and L. I. Schiff, "Statistical limitations on the resolving time of a scintillation counter [26]," *Physical Review*, vol. 80, no. 6, p. 1113, 1950.

[36] G. Ranucci, "Time statistics of the photoelectron emission process in scintillation counters," *Nuclear Inst. and Methods in Physics Research, A*, vol. 335, no. 1-2, pp. 121–128, 1993.

[37] S. Stute, T. Carlier, K. Cristina, C. Noblet, a. Martineau, B. Hutton, L. Barnden, and I. Buvat, "Monte Carlo simulations of clinical PET and SPECT scans: impact of the input data on the simulated images.," *Physics in medicine and biology*, vol. 56, no. 19, pp. 6441–57, 2011.

[38] W. Geant4, "https://en.wikipedia.org/wiki/Geant4."

[39] I. Buvat, S. Jan, S. Kerhoas, and F. Mayet, "GATE user guide.," no. July 2011, 2011.

[40] Eberly College of Science., "https://onlinecourses.science.psu.edu/stat414/node/191."

[41] B. C. Arnold, N. Balakrishnan, and H. Nagaraja, *A First Course in Order Statistics*. Philadelphia, PA, USA: Society for Industrial and Applied Mathematics, 2008.